Inelastic Scattering of Transversely Phase-Structured Free Electrons

Austin Gregory Nixon

A dissertation
submitted in partial fulfillment of the
requirements for the degree of

Doctor of Philosophy

University of Washington
2025

Reading Committee:
David J. Masiello, Chair
Brandi Cossairt
Bruce Robinson

Program Authorized to Offer Degree:
Chemistry

University of Washington

Abstract

Inelastic Scattering of Transversely
Phase-Structured Free Electrons

Austin Gregory Nixon

Chair of the Supervisory Committee:
David J. Masiello
Department of Chemistry

Recent developments in abilities to produce, parse, and measure the electron's wave function within the transmission electron microscope (TEM) and scanning TEM (STEM), have sparked renewed theoretical interest in quantum mechanical treatments of inelastic electron scattering observables and the information they contain. Optical selection rules, originating from the intrinsic spin and linear momentum degrees of the photon, are commonly leveraged in optical-based spectromicroscopies. Although quantum mechanical treatments of inelastic electron scattering have been well understood in core-loss electron energy loss spectroscopy (EELS) for decades, recent demonstrations shaping the electron wave function in the low-loss regime has driven renewed interest in quantum mechanical treatments of the electron probe. Borrowing ideas from the field of quantum optics, the creation and manipulation of transversely structured vortex (or twisted) electron beams has enabled vectorially-resolved electron energy loss and gain measurements of nanoscale and quantum materials. Additionally, the preparation of free electron qubits endowed with quantum information in the form of quantized energy or topological charge, via structured laser pules, spiral phase plates, and holographic masks, has contributed to the recognition of electrons as potential carriers of quantum information. This dissertation explores the quantum electrodynamics of inelastic electron scattering, with particular emphasis placed upon the investigation and development of novel electron scattering observables and the information they encode.

Contents

List of Figures

Glossary

TEM: Transmission Electron Microscope

STEM: Scanning Transmission Electron Microscope

EELS: Electron Energy Loss Spectroscopy

EEGS: Electron Energy Gain Spectroscopy

LG: Laguerre-Gauss

HG: Hermite-Gauss

Acknowledgments

Though many people have positively contributed to my graduate experiences, I will refrain from indulgence and instead limit my acknowledgments to a select few who, in my view, deserve explicit recognition.

Above all, no words written here can convey the depths of profound gratitude I have for my advisor Dr. David J. Masiello. The opportunity to pursue an education is a gift and a privilege. I am honored to be one of his students, and I shall forever be grateful for his patience, guidance, and scientific mentorship.

I'm indebted to the post-docs Dr. Zhongwei Hu and Dr. Marc Bourgeios for the many hours of scientific collaboration that helped contribute to my growth as a scientist. I'm thankful to Dr. Kevin C. Smith for passing to me his obsession with harmonic oscillators and unitary transformations. I will always be appreciative of Dr. C. Praise Anyanwu, Dr. Liam Wrigley, Siamak Khorasani, and Andrew Rossi for their friendship and encouragement. Lastly, Matthieu Chalifour, Betty (Xiaofei) Guo, and Kevin Moser are owed a specific thanks for their camaraderie and laughter in the office.

List of Publications

Under Review

1. Kevin C. Smith, Austin G. Nixon, and David J. Masiello. Strongly coupled photonic molecules as doubly-coupled oscillators, 2025. [1]

Published

1. Marc R. Bourgeois, Feng Pan, C. Praise Anyanwu, Austin G. Nixon, Elliot K. Beutler, Jennifer A. Dionne, Randall H. Goldsmith, and David J. Masiello. Spectroscopy in nanoscopic cavities: Models and recent experiments. *Annu. Rev. Phys. Chem.*, 75:509–534, 2024. [2]

2. Austin G. Nixon, Matthieu Chalifour, Marc R. Bourgeois, Michael Sanchez, and David J. Masiello. Inelastic scattering of transversely structured free electrons from nanophotonic targets: Theory and computation. *Phys. Rev. A*, 109:043502, Apr 2024. [3]

3. Marc R. Bourgeois, Austin G. Nixon, Matthieu Chalifour, and David J. Masiello. Optical polarization analogs in inelastic free-electron scattering. *Sci. Adv.*, 9(51):eadj6038, 2023. [4]

4. Marc R. Bourgeois, Austin G. Nixon, Matthieu Chalifour, Elliot K. Beutler, and David J. Masiello. Polarization-resolved electron energy gain nanospectroscopy with phase-structured electron beams. *Nano Lett.*, 22(17):7158–7165, 2022. [5]

5. Feng Pan, Kristoffer Karlsson, Austin G. Nixon, Levi T. Hogan, Jonathan M. Ward, Kevin C. Smith, David J. Masiello, Síle Nic Chormaic, and Randall H. Goldsmith. Active control of Plasmonic–Photonic interactions in a microbubble cavity. *J. Phys. Chem. C*, 126(48):20470–20479, December 2022. [6]

6. Parivash Moradifar, Austin G. Nixon, Tiva Sharifi, Tim Brandt van Driel, Pulickel Ajayan, David J. Masiello, and Nasim Alem. Nanoscale mapping and Defect-Assisted manipulation of surface plasmon resonances in 2D Bi2Te3/Sb2Te3 In-Plane heterostructures. *Adv. Opt. Mater.*, 10(10):2101968, May 2022. [7]

7. Yueying Wu, Zhongwei Hu, Xiang-Tian Kong, Juan Carlos Idrobo, Austin G. Nixon, Philip D. Rack, David J. Masiello, and Jon P. Camden. Infrared plasmonics: Stem-eels characterization of fabry-pérot resonance damping in gold nanowires. *Phys. Rev. B*, 101:085409, Feb 2020. [8]

8. Grace Pakeltis, Zhongwei Hu, Austin G. Nixon, Eva Mutunga, C. Praise Anyanwu, Claire A. West, Juan Carlos Idrobo, Harald Plank, David J. Masiello, Jason D. Fowlkes, and Philip D. Rack. Focused electron beam induced deposition synthesis of 3D photonic and magnetic nanoresonators. *ACS Appl. Nano Mater.*, 2(12):8075–8082, December 2019. [9]

Part I

Foundations

Chapter 1

Introduction

1.1 A Brief Historical Prologue

In the first quarter of the 20th century, Louis de Broglie theorized that matter can exhibit wave-like properties [10]. The experimental demonstration of the wave-nature of matter was confirmed a few years later in 1927, by Clinton Davisson and Lester Germer, as well as George Thompson and Alexander Reid. These two groups independently observed electron diffraction patterns, a distinguishing hallmark of wave-like behavior, by performing electron scattering measurements on crystalline nickel targets [11], and thin metallic films [12], respectively. This all came a couple decades after Max Planck postulated in 1900, that light waves could only gain or lose energy in finite and incremental amounts related to their frequency [13]. Subsequently, it was Albert Einstein who employed the concept of light *quanta* in 1905 to explain the photoelectric effect [14], and shortly thereafter in 1923 Arthur Compton experimentally demonstrated the particle-like behavior of light [15]. The demonstration of the particle nature of light came nearly 100 years after Thomas Young first performed his double slit experiment in 1803, providing direct evidence for the wave phenomena of light [16].

Around this time in the mid-1920s, Erwin Schrödinger, using the matter wave concept put forth by de Broglie, introduced the Schrödinger equation to describe the time evolution of what is known as a quantum mechanical wave-function, due to the Hamiltonian governing the system [17]. In 1927, Paul Dirac built upon these new developments, and was able to accurately explain the emission and absorption of radiation by matter through modeling the interaction between electromagnetic fields and atoms using a quantum mechanical treatment [18]. In the next year, Dirac introduced a wave equation for the interaction of a electron with the electromagnetic field, correctly taking into account special relativity and the spin-1/2 quantum number of the electron [19]. These works birthed the field of quantum electrodynamics, a unification of quantum theory and electrodynamics, which would lay the ground work for what became known as quantum field theory. Following these monumental experimental and theoretical results, Hans Bethe employed the Schrödinger equation to model electron diffraction in the non-relativistic limit [20]. A depiction of an electron

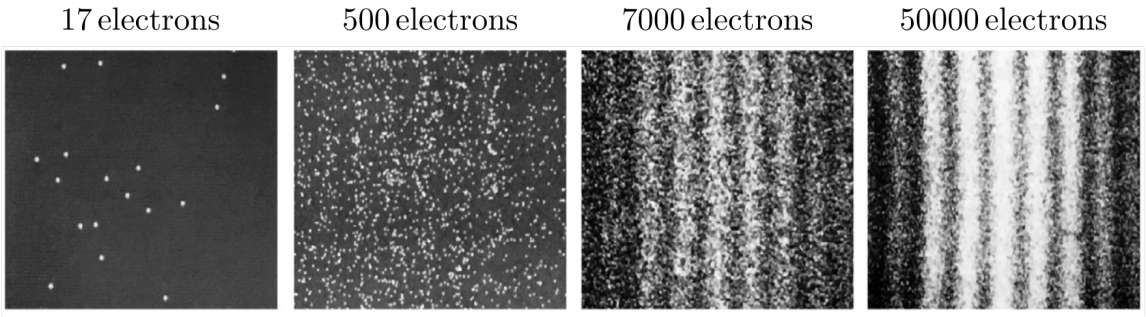

Figure 1.1: Wave-particle duality of electrons as demonstrated by a double-slit interference experiment. Reprinted from [26], with permission from Elsevier.

diffraction experiment is shown in Fig. (1.1), highlighting the wave-particle duality of electrons as evident by the presence of interference fringes. In the following years, other forms matter were shown to exhibit wave-particle duality, such as the neutron [21, 22], as well as atoms [23], and even molecules [24].

Before the debate of wave-particle duality of light and matter was settled, Maxwell's equations, in addition with Lorentz's force law, had provided a mathematically rigorous description for the interactions of electromagnetic waves and charged matter. Known as classical electrodynamics, these four partial differential equations describe the dynamics of interacting electric charges and currents, and ultimately the electromagnetic fields which they source [25]. In tandem with the quantum mechanics revolution of the 20th century, the knowledge and application of these equations helped to lay the foundations of modern chemistry, physics, as well as interdisciplinary subjects such as nanoscience and optics.

Prior to the development of quantum mechanics during the early 20th century, it had been known since the late 1800s, that the resolution of light had a physical constraint. This was illuminated in late 1882, when Ernst Abbe introduced the optical diffraction limit [27], showcasing that the smallest diameter d that light may be focused to is given by

$$d = \frac{\lambda}{2n \sin \theta}, \tag{1.1}$$

where n is the refractive index of the material, θ is the half-angle of the focused cone of light, and λ is the wavelength of light. As a result, the spatial resolution of optical microscopes is fundamentally limited by the corresponding wavelength of light. In stark contrast to the behavior of light waves, due to the revelation of de Broglie, electron waves can reach a far greater spatial resolution depending upon the momentum of the electron. When considering matter waves, the de Broglie wavelength is given by

$$\lambda = \frac{h}{p}, \tag{1.2}$$

with h Planck's constant and p the momentum of the particle. Hence, the wavelength of matter particles is governed by their momentum, the product of their mass and velocity. This realization was in part, a driving

force that helped launch the fields of electron optics and electron microscopy.

The transmission electron microscope, first developed by Max Knoll and Ernst Ruska in 1931, utilized electromagnetic lenses, akin to how glass lenses can be used to focus or disperse light, to focus electrons generated from an cathode ray tube [28, 29]. The first version of the transmission electron microscope was limited in spatial resolution to ∼50 nm. However, subsequent variations and improvements to the electromagnetic lenses improved the spatial resolution, and it was in 1933 [30] that the resolution reached ∼10 nm, surpassing the spatial resolution of ∼200 nm inherent to optical microscopes. This new found level of spatial resolution permitted the visualization of the world at an unprecedented magnification. In addition to viewing biological cells and their larger organelle counterparts, the electron microscope unearthed an entire new world composed macromolecules [31], crystal structures [32], and eventually individual atoms [33].

In the beginning, transmission electron microscopes were primarily reliant on elastically scattered electrons, i.e., electrons which may change trajectory as they interact with the target, though remain energetically unchanged. However, following the advancements of the electron microscope in the 1930s and 1940s, it became apparent that in addition to imaging at the nanoscale, the measurement of the energy distribution of inelastic scattered electrons could also be of great scientific significance. Building upon the work of others, Kai Siegbahn developed the first high resolution of, what is now known as X-ray photoelectron spectroscopy, in the 1950s and 1960s to understand the binding energies of atomic electrons in various chemical samples [34]. This experimental technique relied upon the photoelectron effect, whereby X-rays would eject electrons from a target sample, whose energy would then be recorded by an electron spectrometer. He was able to perform high (energy) resolution measurements on target specimens, showcasing the powerful insight provided by electron energy analyzers [35]. These developments of electron preparation and subsequent measurement, including both spatial and energy resolutions, help build the foundations for electron energy loss spectroscopy.

The theoretical description of electron energy loss was first formulated by Hans Bethe in 1930, to describe the energy loss suffered by charged particles as they traverse matter targets. Known as the stopping power of a material, Bethe's formula related the inelastic scattering cross section for electrons, to the optical properties of the matter they were probing, specifically the inverse dielectric function [20,36]. This helped to set the stage for work to come by David Bohm and his graduate student David Pines in the early 1950s on the collective electromagnetic excitations in electron gases due to long range Coulomb interactions [37–39]. These so called plasmons, could be observed in the low-loss part of the EELS spectrum. Furthermore, Bohm and Pines were able to make distinctions between low-loss inelastic scattering events due to plasmons, and individual particle (core-loss) excitations due to ionization events. The typical electron energy loss regimes for these inelastic scattering events is < 50 eV and 50-100s of eV for low-loss and core-loss, respectively. Taken together, low-loss and core-loss electron energy loss spectroscopies provide detailed insight into the various excitations, be them vibrational (as in the case of phonons), or electromagnetic, as well as the chemical structure of matter targets. In the many decades since, electron microscopies and spectroscopies have revolutionized our understanding of the complex structure of the universe at the nanoscale. Though these were monumental

achievements, iterations and improvements to the electron microscope and their corresponding technologies would pave the way for not only for improved spatial and energy resolutions, but the transverse shaping of the electron wavefunction as well.

It was experimentally proven by Richard Beth in 1936 that photons can posses spin angular momentum [40]. This was done by measureing the torque exerted on quartz wave plates subject to circularly polarized light, demonstrating that right and left circularly polarized light carry $+\hbar$ and $-\hbar$ units of spin angular momentum, respectively. In addition to photon spin, optical beams can also be endowed with spatial structuring, such as orbital angular momentum. In 1992 it was theoretically shown by Les Allen and colleagues that specific laser modes with a helical phase front, referred to as Laguerre-Gauss modes, possessed such orbital angular momentum [41]. They showed that these states of light can carry $\ell\hbar$ units of orbital angular momentum, with ℓ being the topological charge of the optical beam, i.e., the number of times the phase of the wave rotates around the principle axis during a single period of propagation. This was experimentally confirmed only a few years later in 1997, by Miles Padgett et al. whereby the authors were able to rotate an optically trapped particle via the transfer of orbital angular momentum from a Laguerre-Gauss optical mode [42]. In the three decades since, the ideas utilized to create, manipulate and measure these exotic modes of light, so called vortex states or beams, have made their way to the field of electron microscopy.

Inspired by the concept of optical beams carrying orbital angular momentum, scientists at RIKEN (The Institute of Physical and Chemical Research) developed a semiclassical description of electron vortices in 2007, starting from the Schrödinger equation for a matter-wave packet [43]. This groundbreaking work was subsequently followed by direct experimental evidence of electron vortices in 2010, where researchers generated electron beams with orbital angular momentum by passing plane wave electrons through a holographic mask [44] and spiral phase plate [45]. In the following year, electron vortex beams with orbital angular momentum of up to $\pm 100\hbar$ were also created [46]. Nearly a decade later in 2021, electrostatic orbital angular momentum sorters for the electron beam were developed. These sorters, specifically for transmission electron microscope, allowed for the post-selection of the electron wave function carrying specific orbital angular momentum content [47]. Taken together, the ability to pre- and post-select the electron wave function based upon orbital angular momentum quantum number, has opened the door for the measurement of the angular momentum content of target specimens using the transmission electron microscope [48, 49]. Combined with the spatial and energy resolution, the additional capability to track this newfound degree of freedom has begun to impart a lasting impact on the field of electron microscopy.

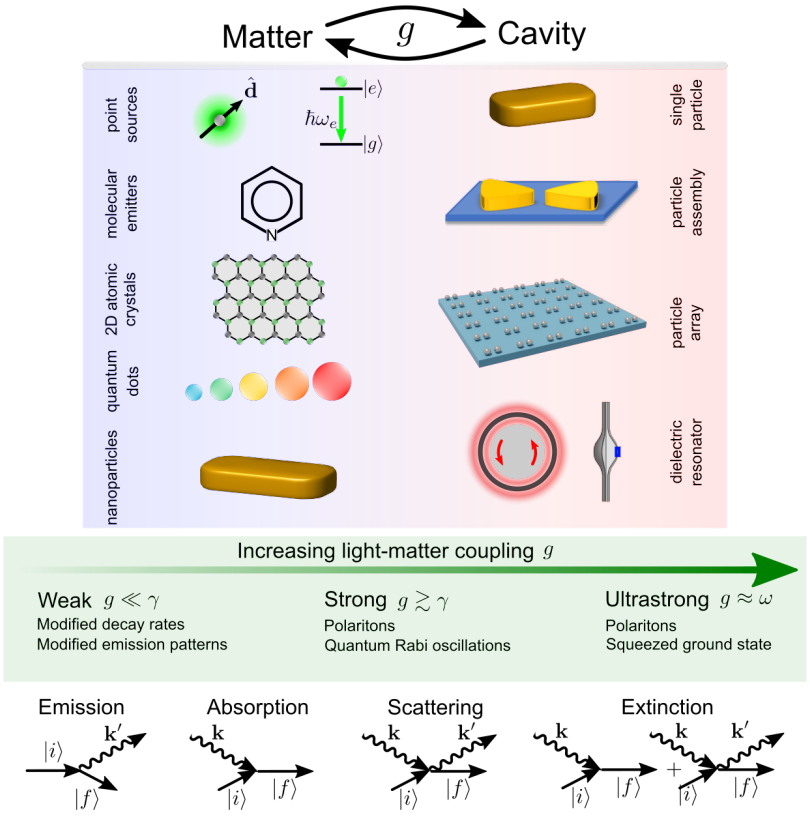

Figure 1.2: Overview of light-matter interactions involving various light (cavity) and matter degrees of freedom. These include atomic, molecular, plasmonic, and excitonic forms of matter, interacting with multiple types of nanophotonic cavities that host optical excitations. Highlighted in green are the different coupling strength regimes between light-matter degrees of freedom and the physical phenomena associated with weak, strong, and ultrastrong coupling strengths. The bottom panel shows diagrammatic processes commonly involved in light-matter interactions. Straight arrows represent initial ($|i\rangle$) and final ($|f\rangle$) material states, whereas sinusoidal arrows represent initial ($\mathbf{k}$) and final ($\mathbf{k}'$) optical wave vectors. Figure taken from Ref. [2].

1.2 Outline of Dissertation

The contents of this dissertation are organized into parts, each part containing individual chapters. Part I is devoted to the background knowledge and theoretical foundations relevant to the research projects I've contributed to over the years, as well as the scientific papers found in part II. The material contained in the latter half of Part I is (collectively) pulled from textbooks I've found useful over the years in my graduate coursework and research endeavors [50–53]. Figure 1.2 provides a succinct overview of the types of nanophotonic targets (coupled or uncoupled) that are frequently investigated with optical and electron beam spectroscopies. Part II presents the scientific papers that constituted a significant portion of my PhD work, with each chapter devoted to a single paper.

Overall, Ch. 2 contains a small collection of organized notes on the topic of modeling optical and electron beam spectroscopies (specifically in the low-loss limit), as well as the dynamics of coupled nanophotonic

systems. None of the material presented in this chapter is novel. Section 2.1 details the basics of Lagrangian and Hamiltonian mechanics. It includes a brief introduction to isolated and coupled harmonic oscillators in the classical limit. Maxwell's Equations are introduced in Sec. 2.2, accompanied by an overview of gauge invariance and short walk-through of the paraxial wave equation derived from the aforementioned electrodynamic equations. Classical descriptions for the modeling of absorption, scattering, and extinction are presented in Sec. 2.3 for the case of a dipole harmonic oscillator driven by an external electric field. Lastly, Sec. 2.4 briefly touches upon the necessary quantum mechanical background, covering a revisitation of the harmonic oscillator, unitary transformations, absorption of a charged particle in an external field, and, finally, electron vortices.

Chapter 3 introduces transversely phase-shaped electron energy gain spectroscopy as a tool to probe the spatial dependence of optically excited nanophotonic target specimens. In this work, the authors propose to combine the energy resolution of optical probes in the continuous-wave limit, with the spatial resolution inherent to electron beam spectroscopies. The electron wave function is treated quantum mechanically as a scalar wave function, rather than as a point charge, as is more common in modeling low-loss electron spectroscopy measurements. Furthermore, building upon recent advancements to pre- and post-select the electron wave function in the orbital angular momentum basis, the authors demonstrate the additional information that can be obtained about the material target when utilizing vortex electron states. Specifically, the nanophotonic target is selectively pumped with an optical plane wave pulse to excite a chosen optically bright mode, which is then spatially resolved with a vortex electron beam. This work highlights the benefits of cross-polarized measurements using optical probes and transversely phase-structured electron beams.

Building upon the previous paper, Ch. 3 unearths a connection between a recent paper concerning low-loss inelastic vortex-electron scattering [48] and the measurement of circular dichroism [54] in the core-loss electron energy loss spectroscopy literature. Specifically, this work draws connections between what is known as the transition current density for the electron beam and the polarization vector of free space light as it appears in optical based scattering observables. Herein, the authors demonstrate that by using a superposition of electron states, in either the focused beam or wide-field limit, the electron probe is capable of retrieving chiral information about the target specimen if pre- and post-selection of the electron state is possible. This is done without the aid of an optical pump as in the case of Ch. 3, as it specifically focuses on electron energy loss, rather than electron energy gain spectroscopy. Overall, the authors establish that by monitoring specific transitions between different electron superposition states — whether wide-field (plane waves) or focused (Laguerre-Gauss or Hermite-Gauss transverse modes) — circular dichroism measurements can be obtained using only the electron beam.

Finally, Ch. 5 extends the work found in the previous two papers and calculates the inelastic electron scattering observables for transitions between a variety of defocused (plane wave) and focused beam (vortex) electron states. These include measurements of electron energy gain and loss probabilities for focused electron beams, as well as the double differential scattering cross section for cases involving plane wave electrons. In

this work, the authors derive the transition current density, relevant to all inelastic scattering observables, between arbitrary plane wave, Bessel, Laguerre-Gauss, and Hermite-Gauss electron states. Lastly, as a proof of concept, select electronic transitions are implemented in the electron-driven discrete dipole approximation code.

Chapter 2

Theoretical Background and Review

2.1 Lagrangian and Hamiltonian Mechanics

In this section, we very briefly introduce the concept of Lagrangian and Hamiltonian formalisms as outlined in [53]. For a more complete description, we refer the reader to Chapter II and Complement A_{II} of the aforementioned reference. When discussing a system made up of n degrees of freedom, one can describe the dynamics of the system if the coordinates $q_i(t)$,..., $q_n(t)$ and velocities $\dot{q}_i(t)$,..., $\dot{q}_n(t)$ at a specific time t, are known. These *dynamical variables* can be used to acquire the accelerations $\ddot{q}_i(t)$,..., $\ddot{q}_n(t)$ and subsequently the equations of motion for a system. By integrating the equations of motion, one can obtain the position of a system as a function of time.

Alternatively, the principle of least action can be employed to understand the dynamics of a system. This variation principle states that the possible paths a system can take as it progresses from some initial point A at time t_1 to a final point B at time t_2, will be the path $q_i(t)$ that minimizes the action S. The action is commonly expressed in terms of the Lagrangian

$$S = \int_{t_1}^{t_2} dt\, L\big(q_i(t), \dot{q}_i(t), t\big), \tag{2.1}$$

where L depends upon the dynamical coordinates $q_i(t)$ and velocities $\dot{q}_i(t)$, and can furthermore be dependent explicitly upon time (though not always). Depending upon the specifics of the system in question, the coordinates and velocities may themselves be a function of time. In the case of a simple point particle, the Lagrangian is the difference between the kinetic and potential energies of the system $L = T - V$, where T and V are the kinetic and potential energies, respectively. Lagrange's equations are given by

$$\frac{d}{dt}\left(\frac{\partial L}{\partial \dot{q}_i}\right) - \frac{\partial L}{\partial q_i} = 0. \tag{2.2}$$

Equation (2.2) can be employed to obtain the equations of motion for a particular system. Lagrange's

equation will be further explored in the context of coupled. and uncoupled harmonic oscillators in Sec. 2.1.1. The momentum conjugate to q_i, and it's time derivative are obtained from the Lagrangian L

$$\begin{aligned} p_i &= \frac{\partial L}{\partial \dot{q}_i} \\ \dot{p}_i &= -\frac{\partial L}{\partial q_i}. \end{aligned} \tag{2.3}$$

The Hamiltonian associated with the Lagrangian $L(q_i, \dot{q}_i, t)$ is given by the sum of the kinetic and potential energies $H = T + V$, which is obtained from the Lagrangian via

$$H(p_i, q_i) = \sum_i \dot{q}_i p_i - L(\dot{q}_i, q_i). \tag{2.4}$$

When considering Hamiltonian mechanics, the dynamical variables are instead the coordinates $q_i(t)$ and momenta $p_i(t)$ rather than the coordinates and velocities. Hamilton's equations are acquired by taking partial derivatives of Eq. (2.4) with respective to the dynamical variables

$$\begin{aligned} \dot{q}_i &= \frac{\partial H}{\partial p_i} \\ \dot{p}_i &= -\frac{\partial H}{\partial q_i}. \end{aligned} \tag{2.5}$$

As will be seen in subsequent sections and chapters, the Hamiltonian of a system will be the starting point for modeling the interaction of light and matter. Additionally, modeling the dynamics of interaction cavity modes as seen in [1], begins with a Lagrangian formalism, before moving on to describe the system dynamics in terms of a Hamiltonian. Finally, the interaction of charged particles with an electromagnetic field is accurately described the the minimal coupling Lagrangian and Hamiltonians; a simple description of this is discussed in Sec. 2.4.

2.1.1 Harmonic Oscillators in Brief

Harmonic oscillators are ubiquitous in nature. In this section, we briefly touch upon the concept of the harmonic oscillator, and apply the Lagrangian and Hamiltonian mechanics formalisms presented in the previous section to understand the dynamics of uncoupled and coupled harmonic oscillators.

For a system of i uncoupled oscillators, the Lagrangian is

$$L = \sum_i \frac{1}{2} m_i \dot{q}_i^2 - \frac{1}{2} m_i \omega_i^2 q_i^2, \tag{2.6}$$

and thereby the Hamiltonian is

$$H = \sum_i \frac{1}{2m_i} \dot{q}_i^2 + \frac{1}{2} m_i \omega_i^2 q_i^2. \tag{2.7}$$

As evident by the previous two equations, the kinetic energy of a simple, single harmonic oscillator is propor-

tional to the velocity of the displacement squared, whereas the potential energy term is proportional to the displacement squared. For the case of a single harmonic oscillator $i = 1$ in Eqs. (2.6) and (2.7), producing the following equation of motion (employing either Lagrange's or Hamilton's equations shown in Sec. 2.1)

$$\ddot{q}_1 + \omega^2 q_1 = 0. \tag{2.8}$$

The frequency ω is related to the spring constant k from Hooke's law via the relationship $\omega = \sqrt{k/m}$. Upon defining the initial conditions $q(0) = q_0$ and $\dot{q}(0) = \dot{q}_0$, whereby q_0 and $\dot{q}_0$ are the coordinate and velocity at time $t = 0$, the solution to this differential equation is given by

$$q(t) = q_0 \cos(\omega t) + \frac{\dot{q}_0}{\omega} \sin(\omega t). \tag{2.9}$$

Therefore, if one knows the Hamiltonian or Lagrangian of a system, its subsequent motion and dynamics can be understood. It goes without saying that in the case mentioned, the energy of the system is conserved. This will not always be physical however, and one may need to account for dissipation. To include the effects of dissipation, we can postulate the following Lagrangian

$$L = \frac{1}{2} m \dot{q}_1^2 e^{\gamma t} - \frac{1}{2} m \omega^2 q_1^2 e^{\gamma t}, \tag{2.10}$$

which produces the equation of motion for a damped harmonic oscillator

$$\ddot{q}_1 + \gamma \dot{q}_1 + \omega^2 q_1 = 0. \tag{2.11}$$

As will be shown in subsequent sections, much of physics and chemistry makes use of harmonic oscillators. For the purposes of this dissertation, we will primarily deal with either a single driven harmonic oscillator representing the collective motion of bound electrons in an atom or charge in a dielectric material, or alternatively, the collective dynamics of coupled harmonic oscillators. This will not be a tutorial in solving various differential equations, however we will walk through select cases as they ultimately relate to work in [1]. Additionally, a brief and illustrative example of harmonic oscillators is detailed in Sec. 2.3 for the case of localized surface plasmons driven by an external electromagnetic field. This is important for the calculation of the absorption, scattering, and extinction observables produced by oscillating charges, and is related to material explored in [6], which concerns the investigation of cavity fields coupled to matter when employing a microbubble cavity.

2.1.2 Coordinate Coupled Oscillators: Equations of Motion

For starters, as a proof of concept, we can write down a generic Lagrangian describing two coupled harmonic oscillators, which are coupled through their coordinates (as opposed to say their velocities as would

be the case of a double pendulum), and subsequently find the supermode eigenfrequencies $\omega_\pm$ of the system. We will refer back to this section when discussing harmonic oscillators in the context of quantum mechanics (and unitary transformations). For such a system, the Lagrangian is

$$L = \frac{1}{2}m_1\dot{q}_1^2 + \frac{1}{2}m_2\dot{q}_2^2 - \frac{1}{2}m_1\omega_1^2 q_1^2 - \frac{1}{2}m_2\omega_2^2 q_2^2 + g q_1 q_2. \tag{2.12}$$

where g is taken to be a constant (and not a function of the frequencies themselves). The corresponding Hamiltonian is

$$H = \frac{1}{2m_1}p_1^2 + \frac{1}{2m_2}p_2^2 + \frac{1}{2}m_1\omega_1^2 q_1^2 + \frac{1}{2}m_2\omega_2^2 q_2^2 - g q_1 q_2. \tag{2.13}$$

With this in hand, employing Lagrange's equations, Eq. (2.2), we arrive at equations of motion for q_1 and q_2, respectively

$$\begin{aligned} \ddot{q}_1 + \omega_1^2 q_1 - \frac{g}{m_1}q_2 &= 0 \\ \ddot{q}_2 + \omega_2^2 q_2 - \frac{g}{m_2}q_1 &= 0. \end{aligned} \tag{2.14}$$

When written in matrix form, the above becomes

$$\frac{d^2}{dt^2}\begin{pmatrix} q_1 \\ q_2 \end{pmatrix} = \begin{pmatrix} -\omega_1^2 & \frac{g}{m_1} \\ \frac{g}{m_2} & -\omega_2^2 \end{pmatrix}\begin{pmatrix} q_1 \\ q_2 \end{pmatrix}. \tag{2.15}$$

It is convenient to recast the above as

$$\ddot{\mathbf{q}} = \mathbf{M}\,\mathbf{q}, \tag{2.16}$$

where $\mathbf{M}$ is the matrix appearing on the right hand side of Eq. (2.15) and $\mathbf{q} = [q_1\ q_2]^T$. The goal is now to diagonalize the matrix appearing on the right hand side of Eq. (2.15). In the unique case where the masses are equal $m_1 = m_2 = m$, no scaling is needed, and only the rotation matrix $\mathbf{R}$ is required for this procedure. However, in the scenario where $m_1 \neq m_2$, an additional scaling matrix $\mathbf{S}$ is needed to complete the procedure. The rotation and scaling matrices are

$$\mathbf{R} = \begin{pmatrix} \cos\theta & -\sin\theta \\ \sin\theta & \cos\theta \end{pmatrix}, \tag{2.17}$$

and

$$\mathbf{S} = \begin{pmatrix} \left(\frac{m_2}{m_1}\right)^{\frac{1}{4}} & 0 \\ 0 & \left(\frac{m_1}{m_2}\right)^{\frac{1}{4}} \end{pmatrix}. \tag{2.18}$$

It is important to note that the matrix $\mathbf{R}$ obeys $\mathbf{R}\mathbf{R}^{-1} = \mathbb{1}$, where $\mathbf{R}^{-1}$ refers to the inverse of the matrix $\mathbf{R}$. The same can be said of the scaling matrix $\mathbf{S}$. Inserting resolutions of the identity in the form of $\mathbf{S}\mathbf{S}^{-1}$,

and performing some algebraic manipulation, Eq. (2.16) becomes

$$\ddot{\mathbf{q}}_s = \mathbf{M}_s\, \mathbf{q}_s. \tag{2.19}$$

Here, $\mathbf{q}_s = \mathbf{S}^{-1}\mathbf{q}$ and the previously asymmetric matrix $\mathbf{M}$ is now symmetric and of the form

$$\mathbf{M}_s = \begin{pmatrix} -\omega_1^2 & \frac{g}{\sqrt{m_1 m_2}} \\ \frac{g}{\sqrt{m_1 m_2}} & -\omega_2^2 \end{pmatrix}. \tag{2.20}$$

Since the matrix is now symmetric, we are in a place to perform a rotation and subsequently diagonalize. Now we can insert resolutions of the identity in the form of the rotation matrix to arrive at

$$\ddot{\mathbf{q}}_\pm = \mathbf{M}_\pm\, \mathbf{q}_\pm, \tag{2.21}$$

with

$$\mathbf{M}_\pm = -\begin{pmatrix} \omega_1^2\cos^2\theta + \omega_2^2\sin^2\theta - \frac{g}{\sqrt{m_1 m_2}}\sin 2\theta & \frac{1}{2}(\omega_2^2 - \omega_1^2)\sin 2\theta - \frac{g}{\sqrt{m_1 m_2}}\cos 2\theta \\ \frac{1}{2}(\omega_2^2 - \omega_1^2)\sin 2\theta - \frac{g}{\sqrt{m_1 m_2}}\cos 2\theta & \omega_2^2\cos^2\theta + \omega_1^2\sin^2\theta + \frac{g}{\sqrt{m_1 m_2}}\sin 2\theta \end{pmatrix}. \tag{2.22}$$

It is evident from the above, that upon the condition where

$$\theta = \frac{1}{2}\tan^{-1}\left(\frac{2g}{\sqrt{m_1 m_2}(\omega_2^2 - \omega_1^2)}\right), \tag{2.23}$$

the off-diagonal terms appearing in Eq. (2.22) are zero. In such cases, the equations of motion defined by Eq. (2.15) are said to be diagonalized, and the supermode frequencies of the coupled system $\omega_\pm$ are readily given as

$$\begin{aligned} \mathbf{M}_\pm &= -\begin{pmatrix} \omega_1^2\cos^2\theta + \omega_2^2\sin^2\theta - \frac{g}{\sqrt{m_1 m_2}}\sin 2\theta & 0 \\ 0 & \omega_2^2\cos^2\theta + \omega_1^2\sin^2\theta + \frac{g}{\sqrt{m_1 m_2}}\sin 2\theta \end{pmatrix} \\ &= -\begin{pmatrix} \omega_+^2 & 0 \\ 0 & \omega_-^2 \end{pmatrix}, \end{aligned} \tag{2.24}$$

with

$$\omega_+^2 = \omega_1^2\cos^2\theta + \omega_2^2\sin^2\theta - \frac{g}{\sqrt{m_1 m_2}}\sin 2\theta \tag{2.25a}$$

$$\omega_-^2 = \omega_2^2\cos^2\theta + \omega_1^2\sin^2\theta + \frac{g}{\sqrt{m_1 m_2}}\sin 2\theta. \tag{2.25b}$$

Thus, the supermode frequencies of the composite system have been obtained via a simple diagonalization procedure. Section 2.4 will walk through a similar procedure when dealing with two coupled quantum

harmonic oscillators. Therein, the same result for the supermode eigenfrequencies will be obtained.

2.2 Electrodynamics

2.2.1 Maxwell's Equations and Gauge Invariance

This section introduces and reviews the basis of electromagnetic theory, and has collectively been sourced from [52, 53]. For a more complete understanding, the interested reader is encouraged to search out the previously mentioned books. To begin, Maxwell's equations in Gaussian units, for sources in vacuum are given by

$$\nabla \cdot \mathbf{E} = 4\pi\rho \tag{2.26a}$$

$$\nabla \cdot \mathbf{B} = 0 \tag{2.26b}$$

$$\nabla \times \mathbf{E} = -\frac{1}{c}\frac{\partial \mathbf{B}}{\partial t} \tag{2.26c}$$

$$\nabla \times \mathbf{B} = \frac{1}{c}\frac{\partial \mathbf{E}}{\partial t} + \frac{4\pi}{c}\mathbf{j}, \tag{2.26d}$$

where $\mathbf{E}$ and $\mathbf{B}$ are the respective electric and magnetic fields, which are sourced by the charge ρ and current $\mathbf{j}$ densities [52, 53]. These quantities are related via the continuity equation for electric charge

$$\frac{\partial \rho}{\partial t} + \nabla \cdot \mathbf{j} = 0. \tag{2.27}$$

We can imagine further, that the electromagnetic fields are sourced by two different forms of material, (i) free charge, i.e., ions and charged particles, and (ii) bound charges in the form of a polarizable medium. In this case, the source terms appearing in Eqs. (2.26) can be further decomposed into *free* (denoted f) and *bound* (denoted b) charges that are due to presence of free and bound charges such as

$$\rho = \rho_f + \rho_b \tag{2.28a}$$

$$\mathbf{j} = \mathbf{j}_f + \mathbf{j}_b. \tag{2.28b}$$

Furthermore, in the microscopic case, we can assume that ρ_f can be written as a sum over individual charge carries, such that

$$\rho_f = \sum_i q_i \delta(\mathbf{x} - \mathbf{x}_i) \tag{2.29a}$$

$$\mathbf{j}_f = \sum_i q_i \mathbf{v}_i \delta(\mathbf{x} - \mathbf{x}_i), \tag{2.29b}$$

where $\mathbf{v}_i = \dot{\mathbf{x}}_i$ is the velocity of the ith charge. When considering the bound charge, per usual [cite], we assume that the bound charge is related to the polarization of a material via

$$\rho_b = -\nabla \cdot \mathbf{P}, \tag{2.30}$$

realizing the relationship $\mathbf{j}_b = \dot{\mathbf{P}}$. Making use of Eqs. (2.26a), and Eq. (2.28) we arrive at $\nabla \cdot \mathbf{D} = 4\pi\rho_f$, where we have introduced the displacement field $\mathbf{D} = \mathbf{E} + 4\pi\mathbf{P}$. Thus, Maxwell's equations for macroscopic medium are

$$\nabla \cdot \mathbf{D} = 4\pi\rho_f \tag{2.31a}$$

$$\nabla \cdot \mathbf{B} = 0 \tag{2.31b}$$

$$\nabla \times \mathbf{E} = -\frac{1}{c}\frac{\partial \mathbf{B}}{\partial t} \tag{2.31c}$$

$$\nabla \times \mathbf{H} = \frac{1}{c}\frac{\partial \mathbf{D}}{\partial t} + \frac{4\pi}{c}\mathbf{j}_f \tag{2.31d}$$

where we have chosen to set the magnetic permeability μ equal to 1, such that $\mathbf{B} = \mu\mathbf{H} = \mathbf{H}$. In the case of a linear and isotropic material, $\mathbf{P} = \chi(\mathbf{x})\mathbf{E}$, where $\chi(\mathbf{x})$ is the linear susceptibility. Here, $\mathbf{D} = \epsilon(\mathbf{x})\mathbf{E}$, with $\epsilon(\mathbf{x}) = 1 + 4\pi\chi(\mathbf{x})$. Equations (2.26b) and (2.26c) hint that electric and magnetic fields may be decomposed into

$$\mathbf{E} = -\nabla\phi - \frac{1}{c}\frac{\partial \mathbf{A}}{\partial t} \tag{2.32a}$$

$$\mathbf{B} = \nabla \times \mathbf{A}, \tag{2.32b}$$

where $\mathbf{A}$ and ϕ are the vector and scalar potentials, respectively. Insertion of these forms for the electric and magnetic fields into Eqs. (2.32), produce equations of motion for the potentials

$$\nabla^2\phi + \frac{1}{c}\frac{\partial}{\partial t}\Big(\nabla \cdot \mathbf{A}\Big) = -4\pi\rho \tag{2.33a}$$

$$\nabla^2\mathbf{A} - \frac{1}{c^2}\frac{\partial^2 \mathbf{A}}{\partial t^2} - \nabla\left(\nabla \cdot \mathbf{A} + \frac{1}{c}\frac{\partial \phi}{\partial t}\right) = -\frac{4\pi}{c}\mathbf{j}. \tag{2.33b}$$

It can be shown that Eqs. (2.33) are unaltered upon the transformation of the vector and scalar potentials as

$$\mathbf{A} \to \mathbf{A} + \nabla\Lambda \tag{2.34a}$$

$$\phi \to \phi - \frac{1}{c}\frac{\partial \Lambda}{\partial t}, \tag{2.34b}$$

with $\Lambda(\mathbf{x}, t)$ an arbitrary function of space and time. The invariance of the fields under these transformations is known as gauge invariance [52, 53]. A common Gauge used when investigating the interactions of light-

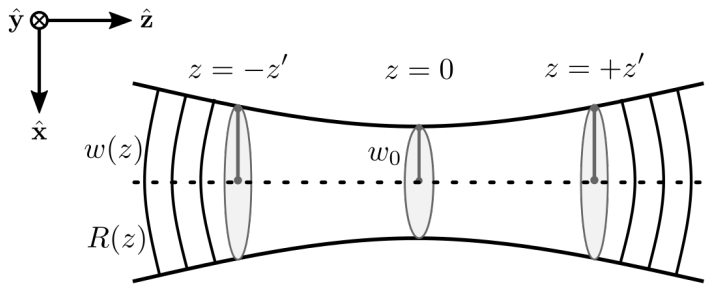

Figure 2.1: Optical vortex beams. Panel (a) displays a schematic of structured beams, such as the Laguerre- and Hermite-Gauss optical modes. Here, $R(z)$ is the radius of curvature at the axial position z, $w(z)$ is the beam waist, and w_0 is the beam waist at $z = 0$. The optical states propagate along the $\hat{\mathbf{z}}$ direction, with transverse components in the $\{\hat{\mathbf{x}}, \hat{\mathbf{y}}\}$ plane.

matter is the Coulomb (alternatively known as the transverse gauge) gauge is given by

$$\nabla \cdot \mathbf{A}(\mathbf{x}) = 0. \tag{2.35}$$

In this scenario, Eq. (2.33a) becomes the well-known Poisson's equation in electrostatics $\nabla^2\phi = -4\pi\rho$, which, in the absence of free charge, reduces to Laplace's equation $\nabla^2\phi = 0$. When polarizable material is present, see Eqs. (2.31d), it can instead be helpful to work in what is known as the generalized Coulomb gauge whereby

$$\nabla \cdot \boldsymbol{\epsilon}(\mathbf{x})\, \mathbf{A}(\mathbf{x}) = 0, \tag{2.36}$$

with $\boldsymbol{\epsilon}(\mathbf{x})$ representing the dielectric material of the target.

2.2.2 Paraxial Wave Equation

When considering electromagnetic waves propagating in a uniform isotropic linear media, Maxwell's equations are reduced to the form

$$\nabla \cdot \mathbf{E} = 0 \tag{2.37a}$$

$$\nabla \cdot \mathbf{B} = 0 \tag{2.37b}$$

$$\nabla \times \mathbf{E} = -\frac{1}{c}\frac{\partial \mathbf{B}}{\partial t} \tag{2.37c}$$

$$\nabla \times \mathbf{B} = \frac{\epsilon\mu}{c}\frac{\partial \mathbf{E}}{\partial t}, \tag{2.37d}$$

where ϵ and μ are the electric permittivity and magnetic permeability of the material, respectively. Taking the cross product of Eqs. (2.37c) and (2.37d), and then making use of the following identity $\nabla \times \nabla \times \mathbf{v} = \nabla(\nabla \cdot \mathbf{v}) - \nabla^2\mathbf{v}$, where $\mathbf{v}$ is a generic 3-dimensional vector, we arrive at the well known Helmholtz wave

equation

$$\left\{\nabla^2 - \frac{\epsilon\mu}{c^2}\frac{\partial^2}{\partial t^2}\right\}\begin{bmatrix}\mathbf{E}\\ \mathbf{B}\end{bmatrix} = 0. \tag{2.38}$$

The most general form for a circularly polarized plane wave (linear combination of two plane waves) propagating in the $\mathbf{k} = k\hat{\mathbf{n}}$ direction is

$$\mathbf{E}(\mathbf{x}, t) = \big(\hat{\boldsymbol{\varepsilon}}_1 E_1 + \hat{\boldsymbol{\varepsilon}}_2 E_2\big)e^{i(\mathbf{k}\cdot\mathbf{x}-\omega t)}. \tag{2.39}$$

Here E_1 and E_2 are complex amplitudes containing the phase information of the propagating linear waves, and $\hat{\boldsymbol{\varepsilon}}$ the corresponding polarizations. When $E_1 = E_2$, Eq. (2.39) represents the electric field with linear polarization. However, when the amplitudes differ in their phases, Eq. (2.39) represented elliptically polarization. If E_1 and E_2 have the same magnitude but differ in a phase by $\pi/2$, the electric field is said to be circularly polarized, such that $\mathbf{E}(\mathbf{x}, t) = E_0(\hat{\boldsymbol{\varepsilon}}_1 \pm i\hat{\boldsymbol{\varepsilon}}_2)e^{i(\mathbf{k}\cdot\mathbf{x}-\omega t)}$. If a solution is proposed to Eq. (2.38) of the form $\mathbf{E}(\mathbf{x}, t) = E_0 u(\mathbf{x})\hat{\boldsymbol{\varepsilon}}e^{i(k_z z-\omega t)}$, we arrive at

$$\left(\nabla^2 + 2ik_z\frac{\partial}{\partial z}\right)u(\mathbf{x}) = 0. \tag{2.40}$$

In cases such that $|\partial^2 u(\mathbf{x})/\partial z^2| << |\nabla_\perp^2 u(\mathbf{x})|$ and $2k_z|\partial u(\mathbf{x})/\partial z| << |\nabla_\perp^2 u(\mathbf{x})|$, Eq. (2.40) reduces to the well known paraxial wave equation

$$\left(\nabla_\perp^2 + 2ik_z\frac{\partial}{\partial z}\right)u(\mathbf{x}) = 0. \tag{2.41}$$

In the cylindrical coordinate system, vortex solutions are given by

$$\begin{aligned} u_{l,p}(\mathbf{x}, t) = \sqrt{\frac{2^{|\ell|+1}p!}{\pi(|\ell|+p)!}}\frac{z_R}{\sqrt{z_R^2+z^2}}\left(\frac{\sqrt{2}\rho}{w(z)}\right)^{|\ell|}\mathrm{L}_p^{(|\ell|)}\left[\frac{2\rho^2}{w(z)^2}\right]e^{k_z z}e^{i(k_z z-\omega t)}e^{i\ell\phi}e^{-\rho^2/w(z)^2} \\ \times e^{ik_z\rho^2 z/2(z_R^2+z^2)-i(2p+|\ell|+1)\tan^{-1}(z/z_R)}, \end{aligned} \tag{2.42}$$

which are known as the Laguerre-Gaussian modes [41]. Here, the waist of the beam is $w(z) = w_0\sqrt{1+(2z/k_z w_0^2)^2}$, and Rayleigh range $z_R = k_z w_0^2/2$ are written in terms of the beam radius at the focus $w_0 = w(z=0)$. Displayed in Fig. 2.1 is a schematic of a paraxial optical beam. When working in the weak-focusing limit whereby the beam waist is independent of the z-coordinate, the Laguerre-Gauss and Hermite-Gauss transverse states take a more simplified form [48]

$$\begin{aligned} \Psi_{n,m}^{\mathrm{HG}}(x, y) &= \frac{1}{w_0}\sqrt{\frac{2}{\pi n!m!}}\,2^{-\frac{n+m}{2}}H_n\left[\frac{x\sqrt{2}}{w_0}\right]H_m\left[\frac{y\sqrt{2}}{w_0}\right]e^{-\frac{x^2+y^2}{w_0^2}} \\ \Psi_{l,p}^{\mathrm{LG}}(R, \phi) &= \frac{1}{w_0}\sqrt{\frac{2p!}{\pi(|\ell|+p)!}}\left(\frac{\sqrt{2}R}{w_0}\right)^{|\ell|}\mathrm{L}_p^{(|\ell|)}\left[\frac{2R^2}{w_0^2}\right]e^{i\ell\phi}e^{-\frac{x^2+y^2}{w_0^2}}. \end{aligned} \tag{2.43}$$

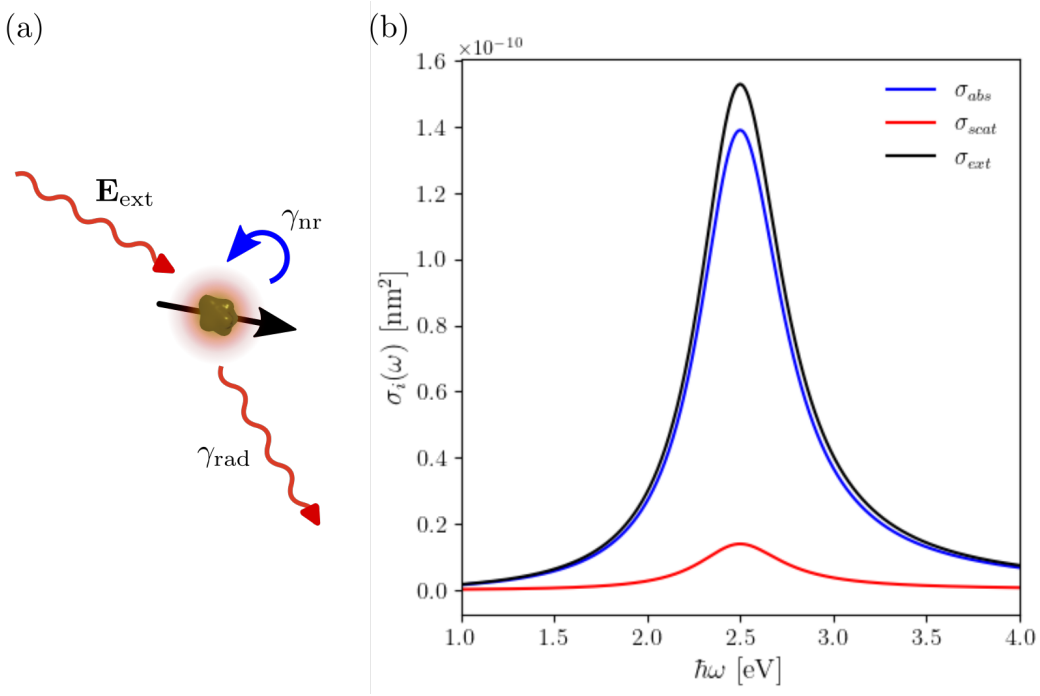

Figure 2.2: Absorption, scattering, and extinction cross sections for a single dipole. Panel (a) depicts a schematic of a point dipole driven by an optical plane wave represented $\mathbf{E}_{\text{ext}}$. Shown in panel (b) are the absorption, scattering, and extinction cross sections for a single driven dipole. For the present example, $\hbar\omega_0 = 2.5\,\text{eV}$, $\hbar\gamma_{\text{nr}} = 0.05\,\text{eV}$, $\hbar\gamma_{\text{nr}} = 0.005\,\text{eV}$, and $m = 8.31 \times 10^{-7} m_e$ where m_e is the electron mass. The trace colors for σ_{abs} and σ_{scat} correspond to the non-radiative and radiative dissipation processes depicted in panel (a), respectively.

When considering a charged particle in a magnetic field, these are known as Landau states or levels. Therefore, in the context of electron spectroscopies, Eq. (2.43) are mathematically convenient, being highly idealized cases.

2.3 Cross sections for an externally driven dipole.

In this section, we build upon the previous sections involving Harmonic oscillators and Maxwell's equations. This is specifically relevant to some of the work done in [6] and the works that preceded it. The collective electromagnetic response of bound atomic electrons in a polarizable material, subject to external driving electric field, can be modeled as a driven harmonic oscillator via the equation of motion

$$m\ddot{\mathbf{x}}(t) + m\gamma_{\text{tot}}\dot{\mathbf{x}}(t) + m\omega_0^2\mathbf{x}(t) = \mathbf{F}(t), \tag{2.44}$$

where $\mathbf{F}(t)$ is a yet to be defined electromagnetic driving force. The driving force can be due to an optical plane wave, or alternatively the electric field of a passing free electron. The damping terms can be composed of both radiative γ_{rad} and non-radiative γ_{nr} terms, such that the $\gamma_{\text{tot}} = \gamma_{\text{rad}} + \gamma_{\text{nr}}$. For the example case

presented here, the forcing terms are: (i) the restoring force of the oscillator $\mathbf{F}_{\text{restore}} = m\omega_0^2\mathbf{x}$, (ii) the radiative force $\mathbf{F}_{\text{rad}} = -2e^2/3c^3\,\dddot{\mathbf{x}} = m\gamma_{\text{rad}}\dot{\mathbf{x}}$, (iii) the non-radiative force $\mathbf{F}_{\text{nr}} = m\gamma_{\text{nr}}\dot{\mathbf{x}}$, and (iv) an external driving force due to the applied electromagnetic field $\mathbf{F}(t) = e\mathbf{E}_{\text{ext}}(t)$. When the fields vary harmonically in time with ω, such that $\mathbf{x}(t) = \mathbf{x}(\omega)e^{-i\omega t}$ and $\mathbf{E}_{\text{ext}}(t) = \hat{\boldsymbol{\varepsilon}}E_0e^{-i\omega t}$, the steady-state solution to Eq. (2.44) is

$$\mathbf{x}(\omega) = \frac{e}{m}\frac{\hat{\boldsymbol{\varepsilon}}E_0}{\omega_0^2 - i\omega\gamma_{\text{tot}} - \omega^2}. \tag{2.45}$$

The induced dipole moment (of a single bound electron) is thus $\mathbf{p} = e\mathbf{x}$. We can relate this to the atomic polarizability of a metal under the influence of an applied electromagnetic field via $\mathbf{p}(\omega) = \alpha(\omega)\mathbf{E}_{\text{ext}}$,

$$\alpha(\omega) = \frac{e^2}{m}\frac{1}{\omega_0^2 - i\omega\gamma_{\text{tot}} - \omega^2}. \tag{2.46}$$

The power radiated by a dipole harmonic oscillator can be obtained by integrating the force $\mathbf{F}_i$ projected onto the velocity $\dot{\mathbf{x}}$

$$\langle P_i\rangle = \frac{1}{T}\int_{-T/2}^{T/2}\mathbf{F}_i\cdot\dot{\mathbf{x}}\,dt. \tag{2.47}$$

With this in mind, we can find the absorption, scattering, and extinction cross section by normalizing the powers acquired from Eq. (2.47) by the incoming energy flux

$$\sigma_i = \frac{\langle P_i\rangle}{S}, \tag{2.48}$$

where $S = cE_0^2/8\pi$ is also known as the time averaged Poynting vector. Due to the complex time-dependence of the variables, the real-part of the variables must be taken in the integrand of Eq. (2.47). If we return to the single driven oscillator, Eq. (2.44), and assuming that the dissipation is a combination of radiative and non-radiative, we can calculate absorption and scattering cross sections. Furthermore, we assume that the dipole is oriented in the $\hat{\mathbf{x}}$ direction, and the force is applied along the same axis such that $\mathbf{F}(t) = e\hat{\mathbf{x}}E_0e^{-i\omega t}$. Therefore, the equation of motion reduces to

$$m\ddot{x} + (\gamma_{\text{rad}} + \gamma_{\text{abs}})\dot{x} + \omega_0^2 x = \frac{e}{m}E_0. \tag{2.49}$$

Using the relations between the induced dipole excitation and the electromagnetic field (i) $\mathbf{p}(\omega) = e\mathbf{x}(\omega)$ and (ii) $\mathbf{p}(\omega) = \alpha(\omega)\mathbf{E}_{\text{ext}}$, we find for the absorbed power

$$\begin{aligned}\langle P_{\text{abs}}\rangle &= \frac{1}{T}\int_{-T/2}^{T/2}\text{Re}\{\mathbf{F}_{\text{abs}}\}\cdot\text{Re}\{\dot{\mathbf{x}}\}\,dt \\ &= \frac{1}{T}(m\gamma_{\text{nr}})\int_{-T/2}^{T/2}\text{Re}\{-i\omega x(\omega)e^{-i\omega t}\}^2\,dt \\ &= \frac{m\gamma_{\text{nr}}}{2}\left(\frac{\omega E_0}{e}\right)^2\left|\alpha(\omega)\right|^2\end{aligned} \tag{2.50}$$

where we have used the polarizability defined by Eq. (2.46). Likewise, the scattered power is given by

$$\begin{aligned}\langle P_{\text{scat}}\rangle &= \frac{1}{T}\int_{-T/2}^{T/2} \text{Re}\big\{\mathbf{F}_{\text{rad}}\big\}\cdot \text{Re}\big\{\dot{\mathbf{x}}\big\}\, dt \\ &= \frac{m\gamma_{\text{rad}}}{2}\left(\frac{\omega E_0}{e}\right)^2 \big|\alpha(\omega)\big|^2\end{aligned} \tag{2.51}$$

All together, the absorption and scattering cross section are

$$\begin{aligned}\sigma_{\text{abs}}(\omega) &= \frac{4\pi\omega^2}{c}\left(\frac{m}{e^2}\right)\gamma_{\text{nr}}\big|\alpha(\omega)\big|^2 \\ \sigma_{\text{scat}}(\omega) &= \frac{4\pi\omega^2}{c}\left(\frac{m}{e^2}\right)\gamma_{\text{rad}}\big|\alpha(\omega)\big|^2.\end{aligned} \tag{2.52}$$

The total extinction cross section is obtained by the sum of the absorption and scattering cross sections

$$\sigma_{\text{ext}}(\omega) = \sigma_{\text{abs}}(\omega) + \sigma_{\text{scat}}(\omega). \tag{2.53}$$

The absorption, scattering, and extinction cross sections for a single dipole harmonic oscillator are displayed in Fig. (2.2) as a proof on concept. We can work through a similar procedure when dealing with two coupled harmonic oscillators. Here we will lay out the procedure and show that the frequency and damping of the first oscillator are influenced by the presence of the second dipole harmonic oscillator. In this scenario, we will find that the atomic polarizability for one oscillator *dresses* the other. The equations of motion for the coupled system are described by

$$\begin{aligned}m_1\ddot{\mathbf{x}}_1(t) + m_1\gamma_{1,\text{tot}}\dot{\mathbf{x}}_1(t) + m_1\omega_1^2\mathbf{x}_1(t) - g\mathbf{x}_2(t) &= \mathbf{F}(t) \\ m_2\ddot{\mathbf{x}}_2(t) + m_2\gamma_{2,\text{tot}}\dot{\mathbf{x}}_2(t) + m_2\omega_2^2\mathbf{x}_2(t) - g\mathbf{x}_1(t) &= 0\end{aligned} \tag{2.54}$$

where we have implicitly assumed that there is only coordinate-coordinate coupling in the Lagrangian. For simplicity, we have chosen to drive only the first dipole. Again, it is assumed that the dipole harmonic oscillators are oriented along the $\hat{\mathbf{x}}$ direction, as well as the driving force $\mathbf{F}$. Working in the steady state limit $x_i(t) = x_i(\omega)e^{i\omega t}$, and projecting onto the dipole axis $\hat{\mathbf{x}}$ we arrive at

$$\begin{aligned}\Big(-\omega^2 - i\omega\gamma_{1,\text{tot}} + \omega_1^2\Big)x_1 - \frac{g}{m_1}x_2 &= \frac{e}{m_1}E_0 \\ \Big(-\omega^2 - i\omega\gamma_{2,\text{tot}} + \omega_2^2\Big)x_2 - \frac{g}{m_2}x_1 &= 0.\end{aligned} \tag{2.55}$$

Solving for x_1 and x_2

$$\begin{aligned} x_1(\omega) &= \frac{eE_0/m_1}{\omega_1^2 - i\omega\gamma_{1,\text{tot}} - \omega^2 - \frac{g^2/m_1m_2}{\omega_2^2 - i\omega\gamma_{2,\text{tot}} - \omega^2}} \\ x_2(\omega) &= \frac{g(eE_0)/m_1m_2}{(\omega_1^2 - i\omega\gamma_{1,\text{tot}} - \omega^2)(\omega_2^2 - i\omega\gamma_{2,\text{tot}} - \omega^2) - \frac{g^2}{m_1m_2}}. \end{aligned} \tag{2.56}$$

Inserting x_2 into the equation for x_1 and repackaging the frequencies and damping into the *dressed* parameters for the first oscillator, we arrive at

$$x_1(\omega) = \frac{eE_0}{m_1\tilde{D}_1}\Big\{\big(\tilde{\omega}_1^2 - \omega^2\big) + i\big(\omega\tilde{\gamma}_{1,\text{tot}}\big)\Big\} \tag{2.57}$$

where we have introduced

$$\begin{aligned} \tilde{\omega}_1^2 &= \omega_1^2 - \frac{g^2}{m_1m_2D_2}\Big(\omega_2^2 - \omega^2\Big) \\ \tilde{\gamma}_{1,\text{tot}} &= \gamma_{1,\text{tot}} + \frac{g^2}{m_1m_2D_2}\gamma_{2,\text{tot}} \end{aligned} \tag{2.58}$$

with a denominator functions defined as $D_i = (\omega_i^2 - \omega^2)^2 + \omega^2\gamma_{i,\text{tot}}^2$ and $\tilde{D}_i = (\tilde{\omega}_i^2 - \omega^2)^2 + \omega^2\tilde{\gamma}_{i,\text{tot}}^2$. As a result, it is apparent that calculated absorption, scattering, and extinction cross sections for the first dipole would inherit features from the second dipole. In such cases, as seen in the *dressed* parameters, the cross section peaks would be shifted due to the presence of a second oscillator. For a detailed investigation on the observables when a second oscillator is included, see Ref. [2].

2.4 Quantum Mechanics Background

2.4.1 Unitary Transformations

When dealing with coupled quantum systems, it can be useful to employ the method of unitary transformations [55] to obtain the eigenvalues of the coupled system. In such cases, the goal is to acquire a closed and analytic relationship between a canonical operator $\mathcal{O}$, and it's transformed counterpart $\widetilde{\mathcal{O}}$. This can be accomplished via the Baker-Campbell-Hausdorff formula and a unitary transformation operator $U = e^S$,

$$\begin{aligned} \widetilde{\mathcal{O}} &= U^\dagger \mathcal{O} U \\ &= \mathcal{O} + [\mathcal{O}, S] + \frac{1}{2!}[[\mathcal{O}, S], S] + \frac{1}{3!}[[[\mathcal{O}, S], S], S] + ..., \end{aligned} \tag{2.59}$$

where the unitarity of U, $UU^\dagger = U^\dagger U = \mathbb{1}$, preserves all commutation relations. For unitarity to be satisfied, the generating function S must be anti-Hermitian, $S^\dagger = -S$. Following from the transformation of an

operator $\widetilde{\mathcal{O}}$ given by Eq. (2.59), the state $|\Psi\rangle$ transforms as

$$\begin{aligned} |\widetilde{\Psi}\rangle &= U^\dagger |\Psi\rangle \\ &= e^{-S}|\Psi\rangle. \end{aligned} \tag{2.60}$$

Due to the unitarity of U, it is evident that the matrix elements are unchanged under unitary transformations, $\langle\Psi|\mathcal{O}|\Psi\rangle = \langle\Psi|U^\dagger\mathcal{O}UU^\dagger|\Psi\rangle = \langle\widetilde{\Psi}|\widetilde{\mathcal{O}}|\widetilde{\Psi}\rangle$. This strategy has recently been employed in the investigation of coupled photonic molecules [1].

2.4.2 Coordinate Coupled Oscillators Revisited

Here we detail the the case of coordinate coupled oscillators, similar to Sec. 2.1.1, though for the case of quantum harmonic oscillators. We will show how to obtain the supermode eigenfrequencies for two coupled, quantum harmonic oscillators by means of unitary transformations as presented in the previous section. With begin with the Hamiltonian for two arbitrary bosonic modes (in x and p), analogous to Eq. (2.13),

$$H = \frac{1}{2m_1}p_1^2 + \frac{1}{2m_2}p_2^2 + \frac{1}{2}m_1\omega_1^2x_1^2 + \frac{1}{2}m_2\omega_2^2x_2^2 - gx_1x_2. \tag{2.61}$$

Returning to the unitary transformations, when the system Hamiltonian is of the form Eq. (2.13), with either coordinate-coordinate or momentum-momentum, the following generating function can be used to diagonalize the system and obtain the supermode frequencies $\omega_\pm$

$$S_1 = \frac{i\theta}{\hbar}\left(\alpha_1 x_1 p_2 - \alpha_2 x_2 p_1\right), \tag{2.62}$$

where α_1 and α_2 are considered the squeezing parameters. The commutation relationships between the momenta p_1, p_2, coordinates x_1, x_2 and the generating function S_1 are

$$\begin{aligned} [p_1, S_1] &= \theta\alpha_1 p_2, & [p_2, S_1] &= -\theta\alpha_2 p_1, \\ [x_1, S_1] &= \theta\alpha_2 x_2, & [x_2, S_1] &= -\theta\alpha_1 x_1, \end{aligned} \tag{2.63}$$

where $[x_i, p_j] = i\hbar\delta_{ij}$. We are now in a position to work out the higher order commutation relations needed by Eq. (2.59). The following series identities for $\cos\phi$ and $\sin\phi$ will prove useful:

$$\begin{aligned} \cos\phi &= 1 - \frac{\phi^2}{2!} + \frac{\phi^4}{4!} - \frac{\phi^6}{6!} + ... \\ &= \sum_{n=0}^{\infty}\frac{(-1)^n}{(2n)!}\phi^{2n} \\ \sin\phi &= \phi - \frac{\phi^3}{3!} + \frac{\phi^5}{5!} - \frac{\phi^7}{7!} + ... \\ &= \sum_{n=0}^{\infty}\frac{(-1)^n}{(2n+1)!}\phi^{2n+1}. \end{aligned} \tag{2.64}$$

Working out the algebra, we arrive at the transformed operators $\tilde{x}_i$, $\tilde{p}_i$ in terms of the old operators

$$\begin{aligned}\begin{pmatrix}\tilde{x}_1\\ \tilde{x}_2\end{pmatrix} &= \begin{pmatrix}\cos\theta & \sqrt{\frac{\alpha_2}{\alpha_1}}\sin\theta\\ -\sqrt{\frac{\alpha_1}{\alpha_2}}\sin\theta & \cos\theta\end{pmatrix}\begin{pmatrix}x_1\\ x_2\end{pmatrix}\\ \begin{pmatrix}\tilde{p}_1\\ \tilde{p}_2\end{pmatrix} &= \begin{pmatrix}\cos\theta & \sqrt{\frac{\alpha_1}{\alpha_2}}\sin\theta\\ -\sqrt{\frac{\alpha_2}{\alpha_1}}\sin\theta & \cos\theta\end{pmatrix}\begin{pmatrix}p_1\\ p_2\end{pmatrix},\end{aligned} \tag{2.65}$$

where we have imposed the product of the squeezings to be unity $\alpha_1\alpha_2 = 1$. We can preform an inverse matrix operation to obtain the old coordinates and momenta x_i, p_i in terms of the new transformed operators

$$\begin{aligned}\begin{pmatrix}x_1\\ x_2\end{pmatrix} &= \begin{pmatrix}\cos\theta & -\sqrt{\frac{\alpha_2}{\alpha_1}}\sin\theta\\ \sqrt{\frac{\alpha_1}{\alpha_2}}\sin\theta & \cos\theta\end{pmatrix}\begin{pmatrix}\tilde{x}_1\\ \tilde{x}_2\end{pmatrix}\\ \begin{pmatrix}p_1\\ p_2\end{pmatrix} &= \begin{pmatrix}\cos\theta & -\sqrt{\frac{\alpha_1}{\alpha_2}}\sin\theta\\ \sqrt{\frac{\alpha_2}{\alpha_1}}\sin\theta & \cos\theta\end{pmatrix}\begin{pmatrix}\tilde{p}_1\\ \tilde{p}_2\end{pmatrix}.\end{aligned} \tag{2.66}$$

Using the relationships above, the Hamiltonian given by Eq. (2.61) can be expressed in terms of the new transformed variables. The old Hamiltonian expressed in terms of these new variables is

$$\begin{aligned}H = &\frac{1}{2}\Big(\frac{1}{m_1}\cos^2\theta + \frac{1}{m_2}\frac{\alpha_2}{\alpha_1}\sin^2\theta\Big)\tilde{p}_1^2 + \frac{1}{2}\Big(\frac{1}{m_2}\cos^2\theta + \frac{1}{m_1}\frac{\alpha_1}{\alpha_2}\sin^2\theta\Big)\tilde{p}_2^2\\ &+ \frac{1}{2}\Big(m_1\omega_1^2\cos^2\theta + m_2\omega_2^2\frac{\alpha_1}{\alpha_2}\sin^2\theta - 2g\sqrt{\frac{\alpha_1}{\alpha_2}}\cos\theta\sin\theta\Big)\tilde{x}_1^2\\ &+ \frac{1}{2}\Big(m_2\omega_2^2\cos^2\theta + m_1\omega_1^2\frac{\alpha_2}{\alpha_1}\sin^2\theta + 2g\sqrt{\frac{\alpha_2}{\alpha_1}}\cos\theta\sin\theta\Big)\tilde{x}_2^2\\ &+ \Big(\frac{1}{m_2}\sqrt{\frac{\alpha_2}{\alpha_1}} - \frac{1}{m_1}\sqrt{\frac{\alpha_1}{\alpha_2}}\Big)\cos\theta\sin\theta\,\tilde{p}_1\tilde{p}\\ &+ g\Big((m_2\sqrt{\frac{\alpha_1}{\alpha_2}}\omega_2^2 - m_1\sqrt{\frac{\alpha_2}{\alpha_1}}\omega_1^2)\cos\theta\sin\theta - g(\cos^2\theta - \sin^2\theta)\Big)\tilde{x}_1\tilde{x}_2.\end{aligned} \tag{2.67}$$

From Eq. (2.67) we see that the Hamiltonian is decoupled when the following conditions are satisfied:

$$\begin{aligned}\frac{1}{m_2}\sqrt{\frac{\alpha_2}{\alpha_1}} - \frac{1}{m_1}\sqrt{\frac{\alpha_1}{\alpha_2}} &= 0\\ (m_2\sqrt{\frac{\alpha_1}{\alpha_2}}\omega_2^2 - m_1\sqrt{\frac{\alpha_2}{\alpha_1}}\omega_1^2)\cos\theta\sin\theta - g(\cos^2\theta - \sin^2\theta) &= 0.\end{aligned} \tag{2.68}$$

Invoking the unity condition $\alpha_1\alpha_2 = 1$, in combination with the first equation above, yields the results for squeezing parameters: $\alpha_1 = \sqrt{m_1/m_2}$ and $\alpha_2 = \sqrt{m_2/m_1}$. Inserting these findings into the second equation produces the result for the mixing angle

$$\theta = \frac{1}{2}\tan^{-1}\left(\frac{2g}{\sqrt{m_1m_2}(\omega_2^2 - \omega_1^2)}\right). \tag{2.69}$$

This result for θ needed to decoupled and diagonalize two quantum harmonic oscillators is the same as that which was previously found in the classical case when using and equation of motion approach, see Eq. (2.23). When Eqs. (2.68) are satisfied, Eq. (2.67) reduces to a more simplified form

$$\begin{aligned} H &= \frac{1}{2m_1}\tilde{p}_1^2 + \frac{1}{2m_2}\tilde{p}_2^2 \\ &+ \frac{1}{2}m_1\Big(\omega_1^2\cos^2\theta + \omega_2^2\sin^2\theta - \frac{g}{\sqrt{m_1m_2}}\sin 2\theta\Big)\tilde{x}_1^2 \\ &+ \frac{1}{2}m_2\Big(\omega_2^2\cos^2\theta + \omega_1^2\sin^2\theta + \frac{g}{\sqrt{m_1m_2}}\sin 2\theta\Big)\tilde{x}_2^2 \\ &= \frac{1}{2m_1}\tilde{p}_1^2 + \frac{1}{2m_2}\tilde{p}_2^2 + \frac{1}{2}m_1\omega_+^2\tilde{x}_1^2 + \frac{1}{2}m_2\omega_-^2\tilde{x}_2^2, \end{aligned} \tag{2.70}$$

with $\omega_\pm$ defined by Eq. (2.25). To better understand the physics at play, we can explicitly express the eigenfrequencies appearing in Eq. (2.70) in terms of the bare system parameters, as opposed to trigonometric functions with the mixing angle θ as the argument. The trigonometric functions can be rewritten as

$$\begin{aligned} \cos^2\theta &= \frac{1}{2}\Big(\cos 2\theta + 1\Big) = \frac{1}{2}\Big(\frac{1}{\sqrt{1+x^2}} + 1\Big) = \frac{1}{2\sqrt{\delta_\omega^2 + \frac{4g^2}{m_1m_2}}}\left(\omega_2^2 - \omega_1^2 + \sqrt{\delta_\omega^2 + \frac{4g^2}{m_1m_2}}\right) \\ \sin^2\theta &= -\frac{1}{2}\Big(\cos 2\theta - 1\Big) = -\frac{1}{2}\Big(\frac{1}{\sqrt{1+x^2}} - 1\Big) = \frac{1}{2\sqrt{\delta_\omega^2 + \frac{4g^2}{m_1m_2}}}\left(\omega_1^2 - \omega_2^2 + \sqrt{\delta_\omega^2 + \frac{4g^2}{m_1m_2}}\right) \\ \sin 2\theta &= \frac{x}{\sqrt{1+x^2}} = \frac{1}{2\sqrt{\delta_\omega^2 + \frac{4g^2}{m_1m_2}}}\left(\frac{4g}{\sqrt{m_1m_2}}\right) \end{aligned} \tag{2.71}$$

with x defined as $x = 2g/\sqrt{m_1m_2}(\omega_2^2 - \omega_1^2)$, and where we introduced $\delta_\omega = \omega_2^2 - \omega_1^2$ inside the square roots. We find for $\omega_\pm$:

$$\begin{aligned} \omega_+^2 &= \frac{1}{2}\left(\omega_1^2 + \omega_2^2 - \sqrt{\left(\omega_2^2 - \omega_1^2\right)^2 + \frac{4g^2}{m_1m_2}}\right) \\ \omega_-^2 &= \frac{1}{2}\left(\omega_1^2 + \omega_2^2 + \sqrt{\left(\omega_2^2 - \omega_1^2\right)^2 + \frac{4g^2}{m_1m_2}}\right). \end{aligned} \tag{2.72}$$

These forms for the supermode eigenfrequencies, along with those present in Eq. (2.70), are identical to $\omega_\pm$ as discovered in the classical case in Sec. 2.1.1, see Eqs. (2.25). There may be physical systems which exhibit both momentum (or said differently velocity coupling) coupling in addition to coordinate coupling. A coupled pendulum system is one such system, as well as coupled photonic cavities as demonstrated recently in [1]. For a complete procedure on the decoupling and diagonalization of a system with momentum and coordinate coupling, the interested reader is encouraged to seek out the aforementioned paper.

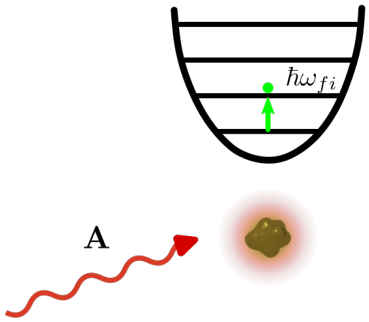

Figure 2.3: Schematic depiction of optical absorption by a matter target. In this case, the matter target is treated quantum mechanically, while the electromagnetic field is classical. The energy associated with the transition dipole is represented by $\hbar\omega_{fi}$ and the electromagnetic vector potential is labeled by $\mathbf{A}$.

2.4.3 Charged Particle in an External Field

The Hamiltonian for a free nonrelativistic particle in an external electromagnetic field is given by

$$H = \frac{1}{2m}\big(\mathbf{p} - \frac{q_e}{c}\mathbf{A}\big)^2 + q_e\phi, \tag{2.73}$$

where c is the speed of light, m the mass of the particle, and $q_e = -e$ with e the elementary charge. An illustrative example of light-matter interactions at first order, and relevant to Chapter 4, can be found in section 5.8 of [50]. In this scenario, we are dealing with the absorption and emission of classical radiation by atomic electrons. For a single bound electron, we begin with the Hamiltonian described by Eq. (2.73), and choose to work in the Coulomb gauge as previously defined by Eq. (2.35), where $\mathbf{A}$ is a classical field, and $\mathbf{p}$ the linear momentum if a single atomic (bound) electron. Under these circumstances, and neglecting the $\mathbf{A}^2$, we have

$$H = \frac{\mathbf{p}^2}{2m} + \frac{q_e}{mc}\mathbf{A}\cdot\mathbf{p}, \tag{2.74}$$

where ϕ has no contribution in the absence of free charge describing the matter. For a monochromatic plane wave, the vector potential is

$$\mathbf{A} = A_0\hat{\boldsymbol{\varepsilon}}\big[e^{i\frac{\omega}{c}\hat{\mathbf{n}}\cdot\mathbf{x}-i\omega t} + e^{-i\frac{\omega}{c}\hat{\mathbf{n}}\cdot\mathbf{x}+i\omega t}\big], \tag{2.75}$$

with $\hat{\boldsymbol{\varepsilon}}$ the linear polarization of light and $\hat{\mathbf{n}}$ the direction of propagation. The two terms appearing in Eq. (2.75) have a different physical meaning: the first term containing $e^{+i\omega t}$ is responsible for stimulated emission, whereas the second term with $e^{-i\omega t}$ is responsible for absorption. We first focus on the case of absorption. Here, the transition rate from an initial target state $|i\rangle$ to a final state $|f\rangle$ is proportional (see previous section) to the matrix elements given by

$$V_{fi} = \langle f\big|\frac{q_e A_0}{mc}\big(\hat{\boldsymbol{\varepsilon}}\cdot\mathbf{p}\big)e^{i\frac{\omega}{c}\hat{\mathbf{n}}\cdot\mathbf{x}}\big|i\rangle \tag{2.76}$$

The transition rate thus takes the form

$$w_{fi}^{abs} = \frac{2\pi}{\hbar}\left(\frac{q_e A_0}{mc}\right)^2 \left|\langle f|\big(\hat{\boldsymbol{\varepsilon}}\cdot\mathbf{p}\big)e^{i\frac{\omega}{c}\hat{\mathbf{n}}\cdot\mathbf{x}}|i\rangle\right|^2 \delta(E_f - E_i - \hbar\omega). \tag{2.77}$$

We can acquire an absorption cross section by dividing the total energy per unit time absorbed by the target matter as it transition from $|i\rangle \to |f\rangle$ by the energy flux of the electromagnetic field. Recalling the relationship between the electric and magnetic fields and the vector potential in the Coulomb gauge (see Eqs. (2.32) and (2.35)), the energy flux is

$$\begin{aligned}\mathcal{U} &= \frac{1}{16\pi}\big(E^2 + B^2\big) \\ &= \frac{1}{2\pi}\frac{\omega^2}{c^2}\big|A_0\big|^2.\end{aligned} \tag{2.78}$$

The absorption cross section is thus given by

$$\sigma^{abs}(\omega) = \frac{4\pi^2}{\omega}\frac{q_e^2}{m^2 c}\left|\langle f|\big(\hat{\boldsymbol{\varepsilon}}\cdot\mathbf{p}\big)e^{i\frac{\omega}{c}\hat{\mathbf{n}}\cdot\mathbf{x}}|i\rangle\right|^2 \delta(E_f - E_i - \hbar\omega). \tag{2.79}$$

When the wavelength of the electromagnetic radiation λ is much greater than the physical dimensions of the atomic target we cam we can make the electric dipole approximation. This amounts to Taylor expanding the exponential $e^{i\frac{\omega}{c}\hat{\mathbf{n}}\cdot\mathbf{x}}$ and retaining the zeroth order term. In this scenario, Eq. (2.79) can be expressed as

$$\sigma^{abs}(\omega) = \frac{4\pi^2}{\omega}\frac{q_e^2}{m^2 c}\left|\hat{\boldsymbol{\varepsilon}}\cdot\langle f|\mathbf{p}|i\rangle\right|^2 \delta(E_f - E_i - \hbar\omega). \tag{2.80}$$

As evident in Eq. (2.80), located inside the matrix elements is the transition dipole moment of the matter $\mathbf{p}_{fi} = \langle f|\mathbf{p}|i\rangle$, dotted into the polarization unit vector $\hat{\boldsymbol{\varepsilon}}$ of the applied driving electric field. One can imagine reversing the roles of the probing optical field and matter target: using an electron (matter) probe to gain insight into the polarization content of the electromagnetic fields produced by a target structure. This is the basis of *optical polarization analogs* as introduced in [48] and further elaborated on in [3, 4].

2.4.4 Electron Vortices

When considering non-relativistic scalar wave-functions descriptions of the free electron (i.e., neglecting the electron spin such that we are not dealing with spinors), the Schrödinger equation can be used to describe the dynamics of the free electron. For example, as shown in [26, 56], vortex electron beams are solutions to the Schrödinger equation.

$$H\psi_k(\mathbf{x}, t) = E_k\psi_k(\mathbf{x}, t), \tag{2.81}$$

where $\psi_k(\mathbf{x}, t)$ is the electron state, and E_k is the associated kinetic energy, given by $E_k = \mathbf{p}_k^2/2m$, with $\mathbf{p}$ the linear momentum. Rearranging Eq. (2.81),

$$\left(\nabla^2 + k^2\right)\psi_k(\mathbf{x}, t) = 0, \tag{2.82}$$

where $k^2 = 2mE_k/\hbar^2$. It is apparent that Eq. (2.82) bears a striking resemblance to Helmholtz wave equation presented as Eq. (2.38). In cylindrical coordinates, the solutions to the Schrödinger equation take the form of axially symmetric states

$$\psi_{\ell,k}(\mathbf{x}) \propto J_{|\ell|}(\kappa r)e^{i\ell\phi}e^{ik_z x_\parallel}, \tag{2.83}$$

where the time dependence has been dropped, i.e., $\psi_k(\mathbf{x}, t) = \psi_k(\mathbf{x})e^{-i(E_k/\hbar)t}$ and $J_{|\ell|}(\kappa r)$ are Bessel functions of the first kind. Here, κ is the transverse wave number and r the radial coordinate. Due to the azimuthal phase factor, these states are eigenfunctions of the z-component orbital angular momentum operator: $\hat{L}_z\psi_{\ell,k}(\mathbf{x}) = \ell\psi_{\ell,k}(\mathbf{x})$. Therefore, vortex electron states carry well-defined longitudinal orbital angular momentum [26]. In order to arrive at Laguerre- and Hermite-Gauss states, the paraxial approximation for the electron wave function must be applied to Eq. (2.82), similar to that done in Sec. 2.2.2. For a more detailed discussion, see Refs. [26, 56].

Part II

Inelastic Scattering of Transversely Structured Free Electrons

Chapter 3

Polarization-Resolved Electron Energy Gain Nanospectroscopy With Phase-Structured Electron Beams

- Marc R. Bourgeois, Austin G. Nixon, Matthieu Chalifour, Elliot K. Beutler, and David J. Masiello. Polarization-resolved electron energy gain nanospectroscopy with phase-structured electron beams. *Nano Lett.*, 22(17):7158–7165, 2022. [5]

3.1 Abstract

Free-electron-based measurements in scanning transmission electron microscopes (STEMs) reveal valuable information on the broadband spectral responses of nanoscale systems with deeply sub-diffraction limited spatial resolution. Leveraging recent advances in manipulating the spatial phase profile of the transverse electron wave front, we theoretically describe interactions between the electron probe and optically-stimulated nanophotonic targets in which the probe gains energy while simultaneously transitioning between transverse states with distinct phase profiles. Exploiting the selection rules governing such transitions, we propose phase-shaped electron energy gain nanospectroscopy for probing the 3D polarization-resolved response field of an optically excited target with nanoscale spatial resolution. Considering ongoing instrumental developments, polarized generalizations of STEM electron energy loss and gain measurements hold the potential to become powerful tools for fundamental studies of quantum materials and their interaction with nearby nanostructures supporting localized surface plasmon or phonon polaritons as well as for non-invasive imaging and nanoscale 3D field tomography.

3.2 Introduction

Optical selection rules based on the polarization degree of freedom of light are indispensable tools for probing mode symmetries in nanophotonic systems, but are fundamentally limited in spatial resolution by diffraction. Below the diffraction limit, near-field based imaging techniques such as scanning near-field optical microscopy [57, 58] and photoemission electron microscopy [59–63] have been used to spectrally and spatially map plasmonic excitations with spatial resolution below 10 nm [64, 65]. STEM nanospectroscopies such as electron energy-loss (EEL) spectroscopy have also been used extensively to map coupled localized surface plasmons (LSPs) [66–72] and LSP-based exciton polariton systems [73–75] with even greater spatial resolution. Although the connection between the photon polarization in X-ray absorption measurements and the momentum exchange during core-loss inelastic electron scattering measurements is well-known [54, 76–79], it has largely been ignored in investigations of low-energy STEM measurements of nanophotonic systems. In the low-loss regime, it is conventional to adopt the non-recoil approximation and to neglect transverse recoil entirely [68]. STEM-EEL observables evaluated quantum mechanically under these assumptions or classically for a uniformly moving point electron depend only on the component of the electromagnetic local density of optical states (EMLDOS) of the target specimen projected along the STEM electron trajectory [80, 81]. Thus, no information on the transverse EMLDOS components is retained by the measurement. Consequently, STEM-based 3D field tomography currently requires collecting a series of EEL measurements with varying relative angles between the electron trajectory and the sample. This information can be used to numerically solve the inverse problem to acquire knowledge of the 3D field profile of a target [82–86].

Building on early hints at an optical polarization analog for electron beams in low-loss measurements [49, 87–89], a recent theoretical work [48] has shown that careful structuring of the transverse spatial profile of the incident electron beam into first order Laguerre-Gauss (LG) vortex states or Hermite-Gauss (HG) states along with post-selection of the outgoing transverse Gaussian state produces an EEL signal that depends only on the target's projected EMLDOS polarized linearly or circularly in the plane perpendicular to the electron propagation axis. In this sense, an analog to plane wave polarization states on the Poincaré sphere has been established for EEL via the introduction of transverse degrees of freedom of the incoming and outgoing STEM electron states combined with the measurement of specific pre- and post-selected state channels. This polarized version of EEL ($\mathrm{EEL}_{\perp}$) spectroscopy stands in stark contrast to conventional EEL ($\mathrm{EEL}_{\parallel}$) measurements, and provides a route to probe the full EMLDOS with deeply sub-diffraction limited spatial resolution.

In this letter we leverage phase-structured free electron beams combined with continuous-wave (cw) laser excitation to develop phase-shaped electron energy gain ($\mathrm{EEG}_{\perp}$) nanospectroscopy capable of probing the 3D polarization-resolved response field of an excited target with nanoscale spatial resolution. This transversely polarized EEG nanospectroscopy further expands the rapidly developing electron microscopy toolset and unlocks a previously unattainable detailed view into nanophotonic systems such as local chirality, the 3D polarization-resolved mode profiles, and polarization singularities. Through an appropriate definition

of a transition current dictated by the probe's transverse wave function degrees of freedom, we find also the one-to-one mapping between Bloch and Poincaré spheres in the fully-retarded laser-stimulated EEG observable and discuss its connection to the transition current derived in the quasistatic limit for EEL measurements [48]. Indeed, by monitoring specific transitions between phase-structured transverse electron states, we show the resulting $\mathrm{EEG}_\perp$ probability spectrum depends only on the components of the laser-stimulated response field projected onto the direction of the transverse transition current. After deriving the $\mathrm{EEG}_\perp$ probability spectrum expression we present analytic and numeric $\mathrm{EEG}_\perp$ calculations for prototypical nanophotonic systems including an isolated sphere, a sphere dimer, and a chiral rod dimer structure.

3.3 Results

During the interaction between a STEM electron and an excited target, the probing electron can inelastically scatter to both lower (spontaneous loss and stimulated loss) as well as higher (stimulated gain) kinetic energies [90–93]. In the spontaneous EEL process the evanescent field of the probe couples to both bright and dark modes of the target. As a consequence, the final states contributing to the total EEL probability include all outgoing longitudinal plane wave electron states $|k_f\rangle$ and all target modes $|\ell\rangle$, where ℓ is a collective index denoting the state of the target, see Figure 3.1a. In the laser-stimulated EEG and EEL processes, energy is transferred to or from the probe from the optically excited state of the target $|\ell\rangle_{\hat{\boldsymbol{\epsilon}}}$, the mode composition of which is dictated by the optical polarization $\hat{\boldsymbol{\epsilon}}$. Importantly, while the loss portion of the spectrum is an incoherent sum of spontaneous and stimulated loss contributions, the stimulated gain spectrum on the anti-Stokes side of the zero-loss peak (ZLP) is free of contamination by other responses beyond the ZLP tail. It should be noted that EEG spectroscopy has been performed with cw optical excitation and in STEMs without a pulsed electron gun [92, 94, 95], which considerably simplifies the experimental setup as compared to photon-induced near-field electron microscopy (PINEM) measurements that employ laser and electron pulses with a controllable time delay [96–101]. Figure 3.1b presents a scheme of the cw laser-stimulated EEG experiment with a single Ag nanoparticle (NP) excited optically and probed with a STEM electron. We take the wave vector $\mathbf{k}$ of the stimulating plane wave (red) to be along the $\hat{\mathbf{z}}$-oriented electron trajectory (blue). Linearly $\hat{\boldsymbol{\epsilon}} = \hat{\mathbf{x}}, \hat{\mathbf{y}}$ and circularly $\hat{\boldsymbol{\epsilon}} = \hat{\mathbf{n}}_+, \hat{\mathbf{n}}_-$ polarized cases with $\hat{\mathbf{n}}_\pm = \left(\hat{\mathbf{x}} \pm i\hat{\mathbf{y}}\right)/\sqrt{2}$ are explicitly shown.

Owing to their large initial longitudinal momentum the paraxial approximation can be invoked to facilitate the separation of the STEM electron's transverse $\mathbf{R}$ and longitudinal z coordinates such that $\mathbf{r} = (\mathbf{R}, z)$. The probe wave function thus becomes

$$\psi_{\mathrm{el}}(\mathbf{r}) = \Psi(\mathbf{R})\frac{e^{ikz}}{\sqrt{L}}, \tag{3.1}$$

where L is the quantization length along z, k is the longitudinal wave vector magnitude, and $\Psi(\mathbf{R})$ is the transverse wave function. Tight focusing in the transverse direction has typically been employed in STEM EEL and EEG measurements to achieve high spatial resolution, and it is conventionally assumed that the incident and transmitted electrons are characterized by the same Gaussian transverse state $\Psi_{00}(\mathbf{R})$. In

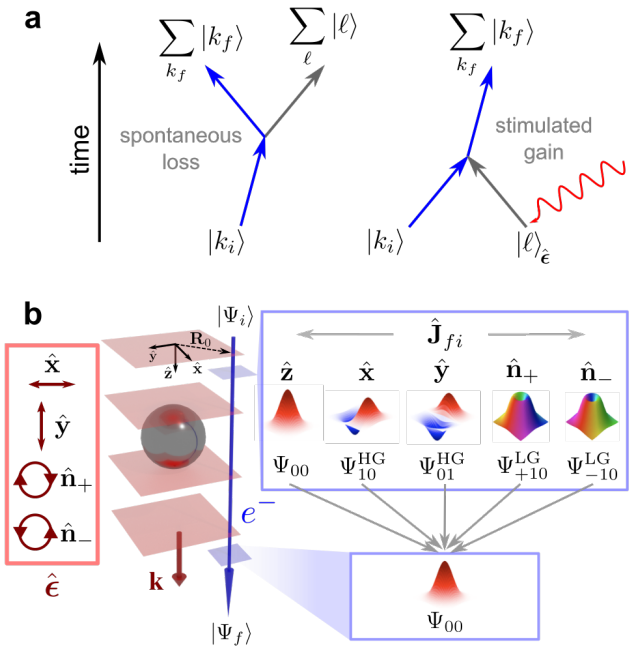

Figure 3.1: Polarized electron energy gain spectroscopy. (a) Interaction schematics illustrating the contributions to measured conventional electron energy loss and gain measurements. Electron and plasmon modes are represented by blue and gray arrows, respectively. The phase fronts of the stimulating laser field are represented as red planes. (b) Schematic diagram enumerating the possible photon polarization states $\hat{\boldsymbol{\epsilon}}$ as well as the unit vectors $\hat{\mathbf{J}}_{fi}$ associated with transitions between various first order Hermite-Gauss ($\Psi_i = \Psi_{nm}^{\mathrm{HG}}$) and Laguerre-Gauss ($\Psi_i = \Psi_{\ell n}^{\mathrm{LG}}$) transverse electron states to the outgoing Gaussian state $\Psi_f = \Psi_{00}$.

the narrow width limit $|\Psi_{00}(\mathbf{R})|^2 = \delta^2(\mathbf{R}-\mathbf{R}_0)$ for impact parameter $\mathbf{R}_0$, the conventional EEG (EEG$_\parallel$) probability spectrum is given by [90–92]

$$\Gamma^{\parallel}_{\rm EEG}(\omega) = \left(\frac{e}{\hbar\omega_\ell}\right)^2 \left| \int dz\; e^{-i\omega z/v}\; \mathbf{E}_{\hat{\boldsymbol{\epsilon}}}(\mathbf{R}_0, z)\cdot\hat{\mathbf{z}} \right|^2 \delta(\omega-\omega_\ell), \tag{3.2}$$

where $-e$ is the electron charge, v is the electron speed, and ω_ℓ and $\hat{\boldsymbol{\epsilon}}$ are the stimulating laser frequency and polarization state, respectively. $\mathbf{E}_{\hat{\boldsymbol{\epsilon}}}(\mathbf{R}_0, z)$ is the positive-frequency component of the response field generated by the target along the electron trajectory oriented in the $\hat{\mathbf{z}}$ direction at $\mathbf{R}_0$.

By generalizing the EEG observable to include the degrees of freedom associated with the initial $|\Psi_i\rangle$ and final $|\Psi_f\rangle$ transverse states of the probe, it can be shown (Supporting Information (SI)) that the generalized EEG probability spectrum within the non-recoil approximation can be written as

$$\Gamma_{\rm EEG}(\omega) = \left(\frac{1}{\hbar\omega_\ell}\right)^2 \left|\mathbf{J}_{fi}\right|^2 \left| \int dz\; e^{-i\omega z/v}\; \mathbf{E}_{\hat{\boldsymbol{\epsilon}}}(\mathbf{R}_0, z)\cdot\hat{\mathbf{J}}_{fi} \right|^2 \delta(\omega-\omega_\ell) \tag{3.3}$$

expressed in terms of the transition current

$$\mathbf{J}_{fi}(\omega) = \frac{i\hbar e}{mv}\left[\langle\Psi_f|\,\boldsymbol{\nabla}_\perp\,|\Psi_i\rangle + \frac{imv}{\hbar}\,\langle\Psi_f|\Psi_i\rangle\,\hat{\mathbf{z}} \right], \tag{3.4}$$

which is completely determined by the initial and final transverse states of the electron. Note that $\hat{\mathbf{J}}_{fi}$ will be purely longitudinal along $\hat{\mathbf{z}}$ when $|\Psi_i\rangle = |\Psi_f\rangle$ and entirely transverse when $|\Psi_i\rangle \neq |\Psi_f\rangle$ and $\langle\Psi_f|\,\boldsymbol{\nabla}_\perp\,|\Psi_i\rangle \neq 0$. Critically, the orientation of the transition current dictates which components of $\mathbf{E}_{\hat{\boldsymbol{\epsilon}}}(\mathbf{R}_0, z)$ contribute to the gain signal along the electron trajectory. When $\langle\mathbf{R}\,|\Psi_i\rangle = \langle\mathbf{R}\,|\Psi_f\rangle = \langle\mathbf{R}\,|\Psi_{00}\rangle$ and $|\langle\mathbf{R}\,|\Psi_{00}\rangle\,|^2 \to \delta^2(\mathbf{R}-\mathbf{R}_0)$, as in the conventional case described above, $\mathbf{J}_{fi}(\omega) = e\hat{\mathbf{z}}$ recovering Eq. (3.2). If, instead, $\langle\Psi_f|\Psi_i\rangle = 0$, the transition current vector will be contained within the 2D transverse plane perpendicular to the electron trajectory. Lourenço-Martins and coworkers discovered [48] that by selecting $|\Psi_i\rangle$ as one of the first-order HG or LG states and $|\Psi_f\rangle = |\Psi_{00}\rangle$, then the $\hat{\mathbf{J}}_{fi}$ vectors derived in the quasistatic limit for the EEL$_\perp$ observable coincide with the basis vectors typically employed to describe linearly and circularly polarized light. In the SI we show that this connection between transverse state transitions and the Poincaré sphere remains for the definitions of $\hat{\mathbf{J}}_{fi}$ in Eq. (3.4) (Figure 3.1b). In this sense, we have extended the work of Ref. [48] to establish an analog to plane wave polarization states on the Poincaré sphere in the context of the fully-retarded laser-stimulated EEG observable.

For suitably defined first order HG and LG transverse states, the magnitudes of the transition currents associated with transitions to the outgoing Gaussian state are of equal magnitude (SI). Thus, since $\langle\Psi_f|\Psi_i\rangle\,\hat{\mathbf{z}} = \mathbf{0}$, this motivates the definition of the transverse EEG probability spectrum

$$\Gamma^{\perp}_{\rm EEG}(\omega) = \left(\frac{e}{\omega_\ell mvw_0}\right)^2 \left| \int dz\; e^{-i\omega z/v}\; \mathbf{E}_{\hat{\boldsymbol{\epsilon}}}(\mathbf{R}_0, z)\cdot\hat{\mathbf{J}}_{fi} \right|^2 \delta(\omega-\omega_\ell), \tag{3.5}$$

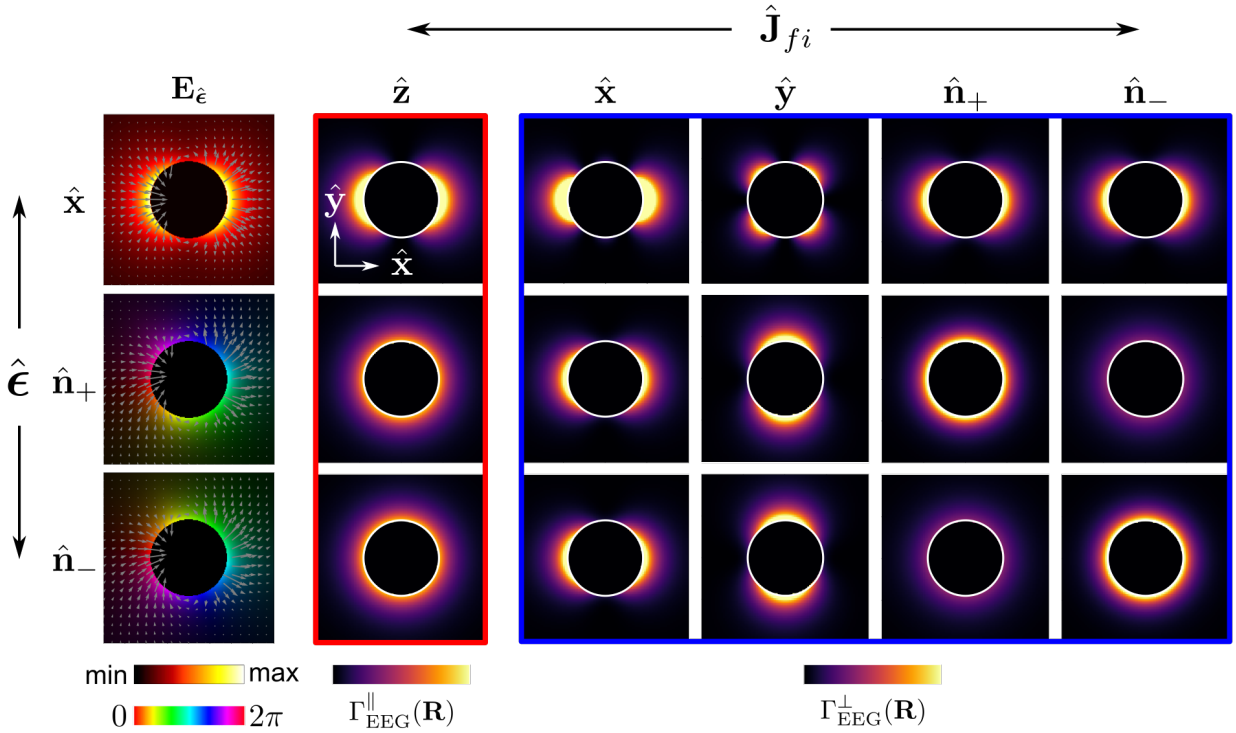

Figure 3.2: Conventional and transverse EEG spectrum images for a 90 nm diameter Ag sphere in the dipolar limit. Each row considers optical excitation polarization described by unit vector $\hat{\boldsymbol{\epsilon}}$. Column 1 presents the optical response field of the excited target, column 2 (red) contains spectrum images resulting from conventional EEG measurements, and columns 3-6 (blue) present transverse gain spectrum images for the $\hat{\mathbf{J}}_{fi}$ cases presented in Figure 1a. All results are evaluated at the dipole localized surface plasmon energy of 3.25 eV for electrons traveling along $\hat{\mathbf{z}}$ at $v = 0.7c$.

where m is the electron mass, w_0 is the beam waist at the focus, and $\hat{\mathbf{J}}_{fi} \in \{\hat{\mathbf{x}}, \hat{\mathbf{y}}, \hat{\mathbf{n}}_\pm\}$ (Figure 3.1b). Evidently, the $\mathrm{EEG}_\perp$ observable measures the Fourier transform of the response field projected onto $\hat{\mathbf{J}}_{fi}$ along the electron trajectory. The feasibility of detecting the $\mathrm{EEG}_\perp$ signal can be assessed using the ratio of transverse to conventional gain probabilities. Assuming a 60 keV electron, with a STEM electron beam waist of $w_0 = 1$ Å, we estimate the ratio of $\mathrm{EEG}_\perp$ to $\mathrm{EEG}_\parallel$ can be as large as $\sim 10^{-4}$. While this ratio is small, both the $\mathrm{EEG}_\parallel$ and $\mathrm{EEG}_\perp$ spectrum amplitudes scale with the stimulating laser intensity and could be detected on zero background with the development of high-quality state sorters [26, 47, 102–104]. Indeed, transitions between a first order HG and outgoing plane wave state have already been experimentally observed in the EEL observable [49]. Comparable $\mathrm{EEG}_\parallel$ and $\mathrm{EEL}_\parallel$ signal amplitudes have been demonstrated experimentally [105] with stimulating cw laser intensities up to $I_0 \sim 5 \times 10^8$ W/m^2 before the onset of photothermal heating induced particle melting.

Mode symmetries of the target can be observed directly in conventional and transverse EEG spectrum images, which can be acquired experimentally via hyperspectral imaging. For a single spherical target in the fully-retarded dipole limit, Eqs. (3.2) and (3.5) can be evaluated analytically for the various combinations

of optical polarization state $\hat{\boldsymbol{\epsilon}} \in \{\hat{\mathbf{x}}, \hat{\mathbf{y}}, \hat{\mathbf{n}}_{\pm}\}$ and initial and final electron transverse states such that $\hat{\mathbf{J}}_{fi} \in \{\hat{\mathbf{x}}, \hat{\mathbf{y}}, \hat{\mathbf{n}}_{\pm}\}$ when $|\Psi_i\rangle \neq |\Psi_f\rangle$ and $\hat{\mathbf{J}}_{fi} = \hat{\mathbf{z}}$ when $|\Psi_i\rangle = |\Psi_f\rangle$ (SI). Spectrum images are presented in Figure 3.2 for a single 90 nm diameter Ag sphere. Each row considers optical excitation polarization described by unit vector $\hat{\boldsymbol{\epsilon}}$. The first column presents the optical response fields $\mathbf{E}_{\hat{\boldsymbol{\epsilon}}}$ of the excited target in the plane through the sphere center. The gray vector field superimposed on each surface plot shows the in-plane response field at a point in time where $\mathbf{E}_{\hat{\boldsymbol{\epsilon}}}$ is primarily oriented along $\hat{\mathbf{x}}$. In the top panel, the underlying color map corresponds to $|\mathbf{E}_{\hat{\mathbf{x}}}(\mathbf{R})|$ within the $z = 0$ plane. In the circularly polarized cases $\hat{\boldsymbol{\epsilon}} = \hat{\mathbf{n}}_{\pm}$, the bright-to-dark contrast represents the field magnitude, while the phase of the response field at position $\mathbf{R}$ when $\mathbf{E}_{\hat{\boldsymbol{\epsilon}}}$ is oriented along $\hat{\mathbf{R}}$ is indicated by the underlying color map.

Spectrum images resulting from $\text{EEG}_{\parallel}$ measurements are presented in the second column (red) of Figure 3.2, which depend only on the $\hat{\mathbf{J}}_{fi} = \hat{\mathbf{z}}$ components of the response fields. It is worth noting that $\text{EEG}_{\parallel}$ spectroscopy cannot distinguish between $\hat{\boldsymbol{\epsilon}} = \hat{\mathbf{n}}_{\pm}$ cases for achiral targets [106]. Columns 3-6 (blue) present normalized transverse gain spectrum images for the specific $\hat{\mathbf{J}}_{fi}$ transitions presented in Figure 3.1b. The $\text{EEG}_{\perp}$ spectrum images arising from the spherical target each exhibit left-right and top-bottom reflection symmetries. Each optical polarization $\hat{\boldsymbol{\epsilon}}$ produces unique $\text{EEG}_{\perp}$ spectrum images that are distinguishable from one another in all cases, illustrating the utility of $\text{EEG}_{\perp}$ nanospectroscopy for directly interrogating excited mode symmetries.

To calculate EEG spectra and spectrum images for more realistic systems beyond spherical particles in the dipole approximation, we developed a fully numerical solution procedure stemming from the optically induced target response field calculated via numerical solution of Maxwell's equations [107]. Both $\text{EEG}_{\parallel}$ and $\text{EEG}_{\perp}$ spectra are evaluated using Eqs. (3.2) and (3.5), respectively, by numerically integrating the target's optically induced response field projected onto the direction of the transition current $\hat{\mathbf{J}}_{fi}$ dictated by the selection of incoming and outgoing transverse electron states over the electron trajectory (SI). We next investigate a dimer system composed of two 50 nm diameter Ag spheres separated by a 10 nm surface-to-surface distance in a background refractive index of unity. Its optical extinction, spontaneous EEL, $\text{EEG}_{\parallel}$, and $\text{EEG}_{\perp}$ spectra are presented in Figure 3.3. The dimer is excited by a plane wave with wave vector along $\hat{\mathbf{z}}$ and polarization along the dimer axis $\hat{\boldsymbol{\epsilon}} = \hat{\mathbf{x}}$. Its response field $\mathbf{E}_{\hat{\mathbf{x}}}$ in the $z = 0$ plane is presented in the top panel of Figure 3.3a at 3.2 eV, corresponding to the spectral location of the optically bright, in-phase collinear dipole LSP mode.

The resonant modes of plasmonic dimers have been investigated previously using $\text{EEL}_{\parallel}$ and $\text{EEG}_{\parallel}$ nanospectroscopies [95, 108, 109]. Placing the electron beam on the dimer axis precisely halfway between the spheres, the position labeled by the dark blue circle in Figure 3.3a, yields the dark blue EEL spectrum. At this impact parameter the lowest-energy excitation the probe couples to is the optically dark out-of-phase collinear dipole LSP mode near 3.5 eV. Alternatively, placing the electron beam at one end of the structure, indicated by the light blue circle in Figure 3.3a, excites both the in-phase and out-of-phase collinear dipole LSP modes at 3.2 eV and 3.5 eV, respectively, as well as higher-order coupled LSP modes as observed in

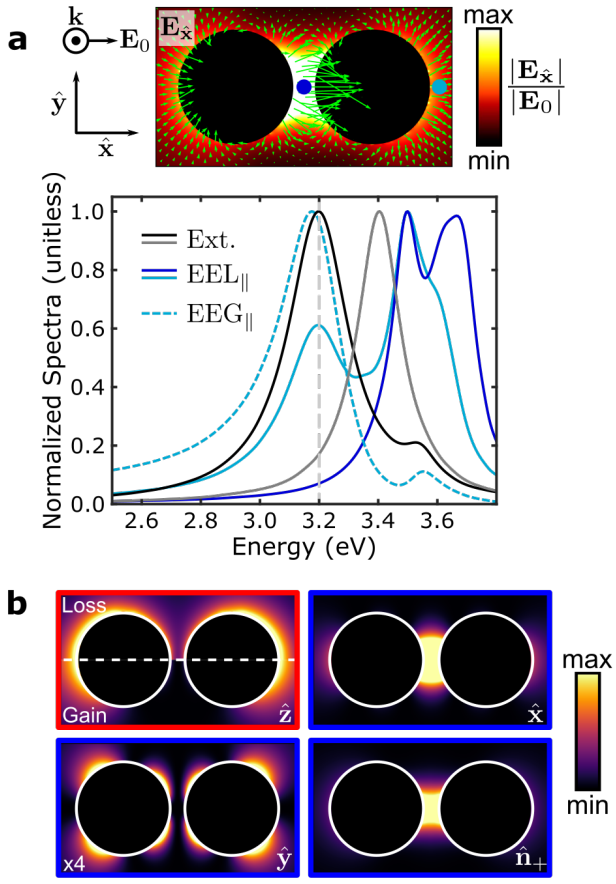

Figure 3.3: Electron energy loss and gain for an Ag sphere dimer. (a) Normalized $\mathrm{EEL}_{\parallel}$ and $\mathrm{EEG}_{\parallel}$ spectra for selected impact parameters indicated as colored dots in the top panel showing the LSP response field $\mathbf{E}_{\hat{\mathbf{x}}}$ near the dimer at 3.2 eV for $\hat{\boldsymbol{\epsilon}} = \hat{\mathbf{x}}$. The overlaid green arrows indicate the in-plane xy components of the response field. The marked impact parameters are each 5 nm from the NP surfaces. Normalized optical extinction spectra for the dimer (black) and individual sphere (gray) are included for comparison. The stimulating plane wave field, when present, is polarized along $\hat{\boldsymbol{\epsilon}} = \hat{\mathbf{x}}$ and the electron speed is $v = 0.7c$ in all cases. (b) Normalized $\mathrm{EEL}_{\parallel}$ and $\mathrm{EEG}_{\parallel}$ (red border) and $\mathrm{EEG}_{\perp}$ (blue border) spectrum images for the sphere dimer system excited by light polarized along $\hat{\mathbf{x}}$ at 3.2 eV. The transition current unit vector $\hat{\mathbf{J}}_{fi}$ is labeled at the bottom right of each spectrum image.

the EEL spectrum traced in solid light blue. The $\text{EEG}_{\parallel}$ spectrum at this impact parameter (dashed light blue trace) is dominated by the optically-bright dimer mode near 3.2 eV as expected based on the differences between $\text{EEL}_{\parallel}$ and $\text{EEG}_{\parallel}$ measurements (Figure 3.1a). The $\text{EEG}_{\perp}$ spectra at the light blue impact parameter (SI) are found to be qualitatively similar to the $\text{EEG}_{\parallel}$ spectrum in Figure 3.3a.

Figure 3.3b shows the normalized $\text{EEL}_{\parallel}$ and $\text{EEG}_{\parallel}$ spectrum images (red border) alongside the normalized $\text{EEG}_{\perp}$ spectrum images (blue borders) at 3.2 eV for $\hat{\boldsymbol{\epsilon}} = \hat{\mathbf{x}}$ and $\hat{\mathbf{J}}_{fi} \in \{\hat{\mathbf{x}}, \hat{\mathbf{y}}, \hat{\mathbf{n}}_{+}\}$. Notably, both $\text{EEL}_{\parallel}$ and $\text{EEG}_{\parallel}$ spectrum images exhibit negligible probability in the gap between the NPs despite the response electric field associated with this mode having the largest amplitude in this region. The elevated enhancement of the $\text{EEL}_{\parallel}$ probability at the top edges of the spheres (i.e., the points furthest from the dimer axis) relative to the $\text{EEG}_{\parallel}$ probability at the bottom edges is indicative of coupling to nearby higher-energy dimer modes in the $\text{EEL}_{\parallel}$ observable, such as the in- and out-of-phase dipolar LSP modes oriented transverse to the dimer axis. Signatures of the transverse modes are absent in the EEG observables as they are not stimulated by the $\hat{\boldsymbol{\epsilon}} = \hat{\mathbf{x}}$ plane wave excitation. In the $\hat{\mathbf{J}}_{fi} = \hat{\mathbf{y}}$ case, the regions of space where this $\text{EEG}_{\perp}$ probability is high at 3.2 eV closely track those where the response field in Figure 3.3a possesses an appreciable $\hat{\mathbf{y}}$ component. Similarly, if $|\Psi_i\rangle = |\Psi^{\text{HG}}_{10}\rangle$ or $|\Psi^{\text{LG}}_{\pm 10}\rangle$, making $\hat{\mathbf{J}}_{fi} = \hat{\mathbf{x}}$ or $\hat{\mathbf{n}}_{\pm}$, the spectrum image at 3.2 eV is strongly localized along the dimer axis between the spheres where the response field is predominantly polarized along $\hat{\mathbf{x}}$. This dimer example highlights the additional wealth of information regarding the spatially-varying vector content of the laser stimulated field that can be accessed using $\text{EEG}_{\perp}$ nanospectroscopy.

The electron transition helicity degree of freedom associated with $|\Psi^{\text{LG}}_{\pm 10}\rangle \rightarrow |\Psi_{00}\rangle$ transitions can additionally be leveraged to probe the chiral responses of targets such as the double rod Born-Kuhn structure [110] considered in Figure 3.4. The scheme in Figure 3.4a shows the left-handed dimer composed of two 30 nm by 100 nm Au rods arranged in an L-shape with a 40 nm relative displacement of the rod centers along $\hat{\mathbf{z}}$. Figure 3.4b shows the optical extinction spectra for incident wave vectors along $\hat{\mathbf{z}}$ and polarizations $\hat{\boldsymbol{\epsilon}} = \hat{\mathbf{n}}_{+}$ (red) and $\hat{\mathbf{n}}_{-}$ (blue). As observed for related rod structures [111, 112], both incident field helicities couple, albeit with unequal strengths, to the bonding and anti-bonding rod modes, marked as vertical dashed gray lines, at 2.03 eV and 2.12 eV, respectively. The optical circular dichroism (CD) spectrum, the difference between extinction spectra for $\hat{\boldsymbol{\epsilon}} = \hat{\mathbf{n}}_{\pm}$ polarized plane wave excitation, is shown in black and exhibits the rod system's chiral response.

While optical CD probes the global chirality of the target, $\text{EEG}_{\perp}$ nanospectroscopy allows the local helicity of the laser-stimulated response field to be probed directly on the nanometer length scale. Figure 3.4c presents the $\hat{\mathbf{J}}_{fi} = \hat{\mathbf{n}}_{+}$ (left) and $\hat{\mathbf{n}}_{-}$ (right) $\text{EEG}_{\perp}$ spectra of the rod system under $\hat{\boldsymbol{\epsilon}} = \hat{\mathbf{n}}_{+}$ plane wave excitation. The $\text{EEG}_{\perp}$ spectra clearly exhibit a strong dependence on the impact parameter and on the helicity of the electron transition current. In analogy to the optical CD observable, we define the position-dependent EEG CD as $\text{CD}^{\hat{\boldsymbol{\epsilon}}}_{\text{EEG}}(\mathbf{R}, \omega) = \Gamma^{\hat{\mathbf{J}}_{fi}=\hat{\mathbf{n}}_{+}}_{\text{EEG}}(\mathbf{R}, \omega) - \Gamma^{\hat{\mathbf{J}}_{fi}=\hat{\mathbf{n}}_{-}}_{\text{EEG}}(\mathbf{R}, \omega)$. The EEG CD spectra at each of the impact parameters indicated in Figure 3.4a are plotted in Figure 3.4d. Unlike the optical CD which is positive-valued at the energy of the bonding mode, the sign of $\text{CD}^{\hat{\mathbf{n}}_{+}}_{\text{EEG}}$ varies with position. Figure 3.4e

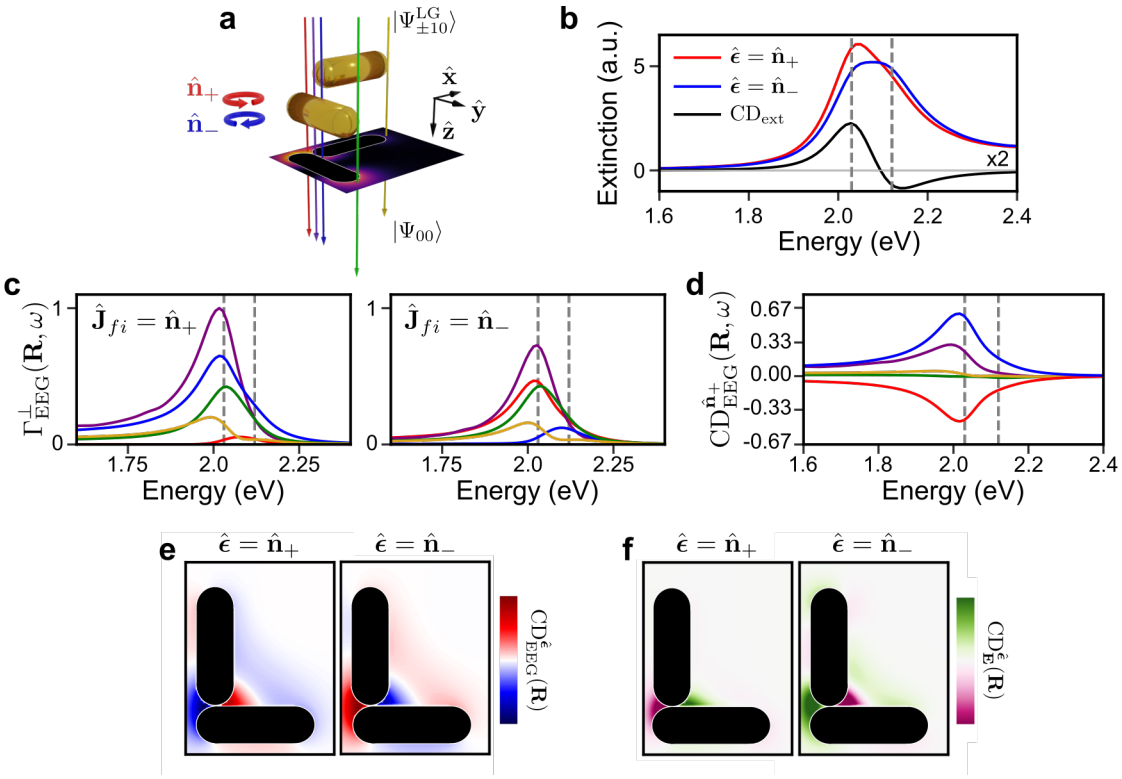

Figure 3.4: $\mathrm{EEG}_{\perp}$ characterization of a chiral plasmonic rod system. (a) Scheme of the Au rod system with colored arrows indicating locations of various electron trajectories. The $\mathrm{EEG}_{\parallel}$ spectrum image at 2.03 eV is included below the structure for $\hat{\boldsymbol{\epsilon}} = \hat{\mathbf{n}}_{+}$. (b) Optical extinction spectra for incident wave vectors along $\hat{\mathbf{z}}$ and $\hat{\boldsymbol{\epsilon}} = \hat{\mathbf{n}}_{+}$ (blue) and $\hat{\mathbf{n}}_{-}$ (red). The optical CD spectrum, scaled by a factor of 2 for improved visibility, is shown in black. (c) $\mathrm{EEG}_{\perp}$ spectra for $\hat{\boldsymbol{\epsilon}} = \hat{\mathbf{n}}_{+}$ and $\hat{\mathbf{J}}_{fi} = \hat{\mathbf{n}}_{+}$ (left) and $\hat{\mathbf{n}}_{-}$ (right). Trace colors correspond to the electron trajectories marked in panel (a). (d) EEG CD spectra for each of the electron trajectories in panel (a). (e) Spatial maps of the EEG CD at 2.03 eV. (f) Spatial variation of the local response field CD at $z = 0$ nm and 2.03 eV.

presents EEG CD images in the vicinity of the nanorods for stimulating laser fields of both helicities.

As shown in the SI, $\mathrm{CD}^{\hat{\boldsymbol{\epsilon}}}_{\mathrm{EEG}}(\mathbf{R},\omega) \propto \left|\mathbf{E}_{\hat{\boldsymbol{\epsilon}}}(\mathbf{R},q,\omega)\cdot\hat{\mathbf{n}}_+\right|^2 - \left|\mathbf{E}_{\hat{\boldsymbol{\epsilon}}}(\mathbf{R},q,\omega)\cdot\hat{\mathbf{n}}_-\right|^2$, which in turn is related to the optical spin density of the component of the target's near-field with wave vector equal to the transfer momentum $q = \omega/v$. While the EEG CD is nonlocal, i.e., it depends on the response field at every point along the electron trajectory, it is reminiscent of the local field CD, which is defined here as $\mathrm{CD}^{\hat{\boldsymbol{\epsilon}}}_{\mathbf{E}}(\mathbf{R},z,\omega) = |\mathbf{E}_{\hat{\boldsymbol{\epsilon}}}(\mathbf{R},z)\cdot\hat{\mathbf{n}}_+|^2 - |\mathbf{E}_{\hat{\boldsymbol{\epsilon}}}(\mathbf{R},z)\cdot\hat{\mathbf{n}}_-|^2$. This quantity is of physical interest as it dictates, for example, the differential coupling strength of a chiral emitter at position $\mathbf{r} = (\mathbf{R},z)$ and with transition dipole vectors $\hat{\mathbf{n}}_\pm$ to $\mathbf{E}_{\hat{\boldsymbol{\epsilon}}}(\mathbf{R},z)$ [113]. Spatial maps of $\mathrm{CD}^{\hat{\boldsymbol{\epsilon}}}_{\mathbf{E}}(\mathbf{R})$ are presented in Figure 3.4f in the $z = 0$ plane located halfway between the displaced rod centers for both incident optical helicities. Direct comparison of the EEG and local field CD spatial maps shows that while there are observable differences, they are qualitatively similar. This similarity is reasonable given that the response field evaluated along the electron trajectory attains its largest amplitude in the vicinity of the target, meaning these locations provide the dominant contributions to the $\mathrm{EEG}_\perp$ signal (SI). Indeed, the connection between $\mathrm{CD}^{\hat{\boldsymbol{\epsilon}}}_{\mathbf{E}}(\mathbf{R},z,\omega)$ and $\mathrm{CD}^{\hat{\boldsymbol{\epsilon}}}_{\mathrm{EEG}}(\mathbf{R},\omega)$ mirrors the connection between the local EMLDOS of physical importance and the longitudinally nonlocal generalized EMLDOS probed directly by conventional EEL measurements [80, 81].

3.4 Discussion

By leveraging transitions between phase-structured free electron transverse states combined with continuous-wave laser excitation we have developed a version of EEG nanospectroscopy capable of probing the 3D polarization-resolved response field of an excited target with nanoscale spatial resolution. We derive a general expression for the EEG probability spectrum for transitions between arbitrary incoming and outgoing transverse electron states that is valid in the fully-retarded regime. By monitoring selected transition channels between incoming and outgoing Hermite-Gauss and Laguerre-Gauss transverse states, specific vector components of the laser-stimulated response field can be selectively probed. Example calculations for several prototypical nanophotonic systems are investigated to highlight the utility of phase-shaped EEG nanospectroscopy for determining mode symmetries, which is currently challenging using other experimental techniques. We also demonstrate that $\mathrm{EEG}_\perp$ measurements allow the local helicity of the target's laser-stimulated response field to be probed directly. Although this work considered only cw laser-stimulated EEG measurements, which are only sensitive to bright modes of the target, the excited target states could also be populated by other means, for example thermally [114–116], which may allow optically dark modes to contribute to the EEG signal. This is an example of one key advantage of phase-shaped EEG relative to polarized EEL for 3D field tomography – the identity of the source generating the response field produced by the excited target is fully decoupled from the probing electron in EEG processes. Taken together, phase-shaped EEG nanospectroscopy builds on recently-developed STEM technology, such as vortex beam generation and state-sorters, and will constitute a powerful addition to the rapidly-developing nanoscale field imaging toolset in

the near-future.

3.5 Acknowledgments

All work was supported by the U.S. Department of Energy (DOE), Office of Science, Office of Basic Energy Sciences (BES), Materials Sciences and Engineering Division under Award No. DOE BES DE-SC0022921.

Chapter 4

Optical Polarization Analogs in Inelastic Free Electron Scattering

- Marc R. Bourgeois, Austin G. Nixon, Matthieu Chalifour, and David J. Masiello. Optical polarization analogs in inelastic free-electron scattering. *Sci. Adv.*, 9(51):eadj6038, 2023. [4]

4.1 Abstract

Advances in the ability to manipulate free electron phase profiles within the electron microscope have spurred development of quantum-mechanical descriptions of electron energy loss (EEL) processes involving transitions between phase-shaped transverse states. Here, we elucidate an underlying connection between two ostensibly distinct optical polarization analogs identified in EEL experiments as manifestations of the same conserved scattering flux. Our work introduces a procedure for probing general tensorial target characteristics including global mode symmetries and local polarization.

4.2 Introduction

Inherently necessitating the exchange of both energy and momentum, measurements involving the absorption and scattering of optical waves and energetic particles provide a wealth of information characterizing atomic, molecular, and nanoscale systems. Selection rules based on the optical polarization degrees of freedom, in particular, are indispensable tools for probing target excitation symmetries, albeit with spatial resolution limited by optical diffraction. With their atomic-scale de Broglie wavelength, high-energy ($100 - 200$ keV) electrons in the scanning transmission electron microscope (STEM) offer superior spatial localization but lack polarization degrees of freedom since they are accurately described by the scalar Schrödinger equation.

Despite this deficiency, it was shown early on that transverse linear momentum transfer $\hbar\mathbf{q}_\perp$ in widefield near-edge electron energy loss (EEL) processes could be exploited to selectively probe atomic inner shell excitations with distinct symmetries [78] and more recently to probe transversely polarized electric fields on the atomic length scale [117]. A formal connection between the photon polarization $\hat{\boldsymbol{\epsilon}}$ in X-ray absorption measurements and $\hbar\mathbf{q}_\perp$ during core-loss inelastic electron scattering measurements was established in the electrostatic limit [76, 77, 79, 118, 119], culminating in the experimental realization of magnetic circular dichroism measurements within a TEM [54, 120].

Improved monochromation and aberration correction technologies, on the other hand, have enabled STEM-EEL characterization of plasmonic [70, 121], nanophotonic [122, 123], and phononic [115, 116, 124] systems in the low-loss ($\lesssim$ 10 eV) regime with nanometer-scale spatial resolution. At such low energies [68, 101], the STEM-EEL observable primarily probes the component of the generalized electromagnetic density of optical states (EMDOS) of the target specimen projected along the TEM axis [80, 81]. However, following the demonstration of vortex electron beams carrying quantized orbital angular momentum (OAM) [44, 45], there has been considerable interest in studying OAM transfer between vortex free electron states and atomic [125, 126] as well as nanophotonic [87–89] targets. In particular, it was demonstrated that the symmetries of excited plasmonic modes could be controlled by pre- and post-selection of the transverse wave functions of the probing free electrons [49, 127]. More recently, a quasistatic theory was presented in which the transition dipole $\hat{\mathbf{d}}^{\perp}_{fi}$ arising during transitions between spatially localized phase-shaped transverse electron states plays the role of an optical polarization analog (OPA) in EEL processes, allowing access to additional components of the target's generalized EMLDOS [48]. Despite the coexistence of the $\hat{\mathbf{d}}^{\perp}_{fi}$ OPA in low-loss STEM-EEL measurements, and the $\hat{\mathbf{q}}_\perp$ OPA in core-loss scattering processes, the connection between these two OPAs has yet to be made explicit.

Here we present a general theoretical framework for describing fully retarded inelastic electron scattering and elucidate the notion of and relationships between OPAs in such measurements. Employing a formalism that explicitly accounts for the swift electron transverse degrees of freedom, we uncover an underlying connection between the two ostensibly distinct OPAs previously identified in linear momentum- (LM-) and OAM-resolved measurements under wide-field and focused beam conditions. Despite their apparent differences and regimes of applicability, the $\hat{\mathbf{q}}_\perp$ and $\hat{\mathbf{d}}^{\perp}_{fi}$ OPAs arising during LM and OAM transfer processes are both manifestations of the transverse components of the transition current density arising in our current-current response formalism. Numerical calculations highlighting the utility of phase-shaped EEL nanospectroscopy for determining mode symmetries and probing the 3D polarization-resolved response field of a plasmonic dimer target with nanoscale spatial resolution are presented.

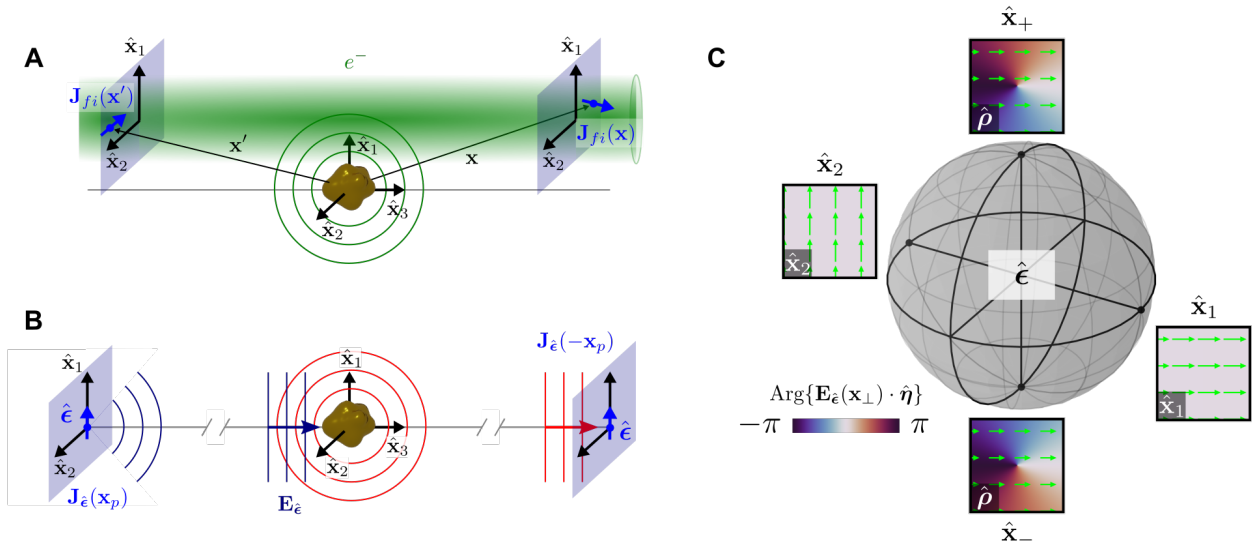

Figure 4.1: **Electron energy loss and optical extinction processes.** (**A**) Scheme showing the EEL process within the current-current response picture. (**B**) Scheme depicting the optical plane wave extinction process within the current-current response picture. Electromagnetic radiation sourced by a point dipole current density $\mathbf{J}_{\hat{\boldsymbol{\epsilon}}}$ located at position $\mathbf{x}_p$ and polarized along $\hat{\boldsymbol{\epsilon}}$ interacts via the target with a mirrored observer dipole at $-\mathbf{x}_p$ (**C**) Free space optical polarization states $\hat{\boldsymbol{\epsilon}}$ represented on the Poincaré sphere. Underlying color maps represent the transverse phase profiles $\mathbf{E}_{\hat{\boldsymbol{\epsilon}}}(\mathbf{x}_\perp, x_3 = 0)\cdot\hat{\boldsymbol{\eta}}$, where $\hat{\boldsymbol{\eta}}$ is a unit vector within the $\mathbf{x}_\perp$ plane.

4.3 Results

Within the first Born approximation, the rate of scattering from the initial light-matter state $|i\rangle|0\rangle$, describing initial electron state $|i\rangle$ and target ground state $|0\rangle$, to a given final state $|f\rangle|n\rangle$ is equal to that found using Fermi's golden rule with the interaction potential $\hat{V} = (e/2mc)(\hat{\mathbf{A}}\cdot\hat{\mathbf{p}} + \hat{\mathbf{p}}\cdot\hat{\mathbf{A}})$ in the generalized Coulomb gauge [128] defined by $\nabla\cdot[\varepsilon(\mathbf{x})\mathbf{A}(\mathbf{x},t)] = 0$ with zero scalar potential. The electron charge is $-e$ and Gaussian units are used throughout this work. Employing a mode expansion of the target's vector potential $\mathbf{A}(\mathbf{x},t) = \sum_n \hat{a}_n^\dagger \mathbf{A}_n^{(-)}(\mathbf{x})e^{+i\omega_n t} + \hat{a}_n \mathbf{A}_n^{(+)}(\mathbf{x})e^{-i\omega_n t}$, the state-to-state frequency-resolved EEL transition rate becomes (see Materials and Methods).

$$
\begin{aligned}
w_{fi}^{\mathrm{loss}}(\omega) &= \frac{2\pi}{\hbar^2}\sum_n \left|\frac{1}{c}\int d\mathbf{x}\ \mathbf{A}_n^{(-)}(\mathbf{x})\cdot\mathbf{J}_{fi}(\mathbf{x})\right|^2 \delta(\omega-\omega_{if})\delta(\omega-\omega_n) \\
&= -\frac{8\pi}{\hbar}\int d\mathbf{x}\,d\mathbf{x}'\ \mathrm{Im}\Big\{\mathbf{J}_{fi}^*(\mathbf{x})\cdot\mathbf{G}(\mathbf{x},\mathbf{x}',\omega)\cdot\mathbf{J}_{fi}(\mathbf{x}')\Big\}\delta(\omega-\omega_{if}) \\
&= \frac{4\pi^2}{\hbar\omega}\int d\mathbf{x}\,d\mathbf{x}'\ \mathbf{J}_{fi}^*(\mathbf{x})\cdot\boldsymbol{\varrho}(\mathbf{x},\mathbf{x}',\omega)\cdot\mathbf{J}_{fi}(\mathbf{x}')\delta(\omega-\omega_{if}),
\end{aligned}
\tag{4.1}
$$

where $E_{if} = \hbar\omega_{if}$ is the energy difference between initial $|i\rangle$ and final $|f\rangle$ electron states, $\boldsymbol{\varrho}(\mathbf{x},\mathbf{x}',\omega) = (-2\omega/\pi)\mathrm{Im}\{\mathbf{G}(\mathbf{x},\mathbf{x}',\omega)\}$ is the generalized EMDOS tensor, and $\mathbf{G}(\mathbf{x},\mathbf{x}',\omega)$ is the induced vector Helmholtz

Green's tensor. The free electron transition current density,

$$\mathbf{J}_{fi}(\mathbf{x}) = \frac{i\hbar e}{2m}\Big\{\psi_f^*(\mathbf{x})\nabla\psi_i(\mathbf{x}) - \psi_i(\mathbf{x})\nabla\psi_f^*(\mathbf{x})\Big\}, \tag{4.2}$$

is fully determined by the initial and final electron states and its orientation determines which components of the generalized EMDOS tensor contribute to $w_{fi}^{\text{loss}}(\omega)$ at each point in space (Figure 4.1A). Meanwhile, the optical extinction cross section is often presented as $\sigma_{\text{ext}}(\omega) = 4\pi(\omega/c)\text{Im}\big\{\hat{\boldsymbol{\epsilon}}^* \cdot \boldsymbol{\alpha}(\omega) \cdot \hat{\boldsymbol{\epsilon}}\big\}$, where $\boldsymbol{\alpha}(\omega)$ is the polarizability tensor characterizing the response of the target located at $\mathbf{x}_t$ to plane wave excitation with polarization unit vector $\hat{\boldsymbol{\epsilon}}$. The optical cross section can be alternatively expressed in a form very similar to Eq. (4.1), e.g., (see Materials and Methods)

$$\sigma_{\text{ext}}(\omega) = 4\pi\frac{\omega}{c}\frac{1}{|\mathbf{E}_{\hat{\boldsymbol{\epsilon}}}(\mathbf{x}_t,\omega)|^2}\text{Im}\bigg\{-\int d\mathbf{x}\, d\mathbf{x}'\, \mathbf{J}_{\hat{\boldsymbol{\epsilon}}}^*(\mathbf{x},\omega)\cdot\mathbf{G}(\mathbf{x},\mathbf{x}',\omega)\cdot\mathbf{J}_{\hat{\boldsymbol{\epsilon}}}(\mathbf{x}',\omega)\bigg\}, \tag{4.3}$$

by imagining that the incident plane wave field $\mathbf{E}_{\hat{\boldsymbol{\epsilon}}}$ is sourced by a point dipole with amplitude p located far away from the target at position $\mathbf{x}_p$ and characterized by current density $\mathbf{J}_{\hat{\boldsymbol{\epsilon}}}(\mathbf{x},\omega) = -i\omega p\delta(\mathbf{x}-\mathbf{x}_p)\hat{\boldsymbol{\epsilon}}$ as shown in Figure 4.1B. Here, $\hat{\mathbf{J}}_{\hat{\boldsymbol{\epsilon}}}$ is locked to $\hat{\boldsymbol{\epsilon}}$, which is in principle any arbitrary free photon pure polarization state described by a point on the Poincaré sphere (Figure 4.1C), where antipodal points $\{\hat{\boldsymbol{\epsilon}}_1, \hat{\boldsymbol{\epsilon}}_2\}$ and $\{\hat{\boldsymbol{\epsilon}}_+, \hat{\boldsymbol{\epsilon}}_-\}$ describe linearly and circularly polarized light, respectively. Spatial maps of the plane wave electric field $\mathbf{E}_{\hat{\boldsymbol{\epsilon}}}(\mathbf{x}_\perp, x_3 = 0)$ (green arrows) with wave vector along $\hat{\mathbf{x}}_3$ are shown for each of the four antipodal points indicated. Underlying color maps show the transverse phase profiles $\mathbf{E}_{\hat{\boldsymbol{\epsilon}}}(\mathbf{x}_\perp, x_3 = 0)\cdot\hat{\boldsymbol{\eta}}$, where $\hat{\boldsymbol{\eta}}$ is a unit vector within the $\mathbf{x}_\perp$ plane and is noted within each plot.

The connection between $\hat{\boldsymbol{\epsilon}}$ in optical measurements and $\hat{\mathbf{J}}_{fi}^{\perp}$ in EELS is determined by the identities of the initial and final free electron states. If the electron wave function can be separated within an orthogonal coordinate system with $\mathbf{x} = (x_1, x_2, x_3)$ and translational invariance along x_3, then the wave function can be written as $\psi(\mathbf{x}) = \Psi(\mathbf{x}_\perp)e^{ik_3x_3} = \Psi_1(x_1)\Psi_2(x_2)e^{ik_3x_3}$ and the transition current density decomposes into transverse and longitudinal parts $\mathbf{J}_{fi}(\mathbf{x}) = \mathbf{J}_{fi}^{\perp}(\mathbf{x}_\perp)e^{iq_\parallel x_3} + J_{fi}^{\parallel}(\mathbf{x})\hat{\mathbf{x}}_3$, where $q_\parallel = k_3^i - k_3^f$ is the longitudinal momentum transfer. These conditions on $\psi(\mathbf{x})$ may be satisfied within the Cartesian as well as polar, elliptical, and parabolic cylindrical coordinate systems [129]. Given the ability to perform EEL measurements with pre- and post-selection of free electron transverse states with rationally sculpted phase profiles, full control may be exerted over the characteristics of $\mathbf{J}_{fi}^{\perp}(\mathbf{x})$, permitting the construction of conventional OPAs as well as other more exotic structured light analogs [130], including radially and azimuthally polarized $\mathbf{J}_{fi}^{\perp}(\mathbf{x})$ (Supplementary Materials). In particular, OPAs can be defined by identifying pairs of initial and final states such that $\hat{\mathbf{J}}_{fi}^{\perp}(\mathbf{x}_\perp) \to \hat{\mathbf{J}}_{fi}^{\perp}$ is position-independent and described by a point on the Poincaré sphere shown in Figure 4.1C with antipodal points constructed from unit vectors $\hat{\mathbf{x}}_1$ and $\hat{\mathbf{x}}_2$. To do so, we note that $\mathbf{J}_{fi}(\mathbf{x})\cdot\hat{\mathbf{x}}_j$ $(j = 1, 2)$ vanishes provided (1) $\Psi_j(x_j)$ remains unchanged during interaction with the target, and (2) $\text{Arg}\big\{\Psi_j(x_j)\big\}$ is constant. Necessary conditions and a general OPA construction are discussed more fully in the Materials and Methods.

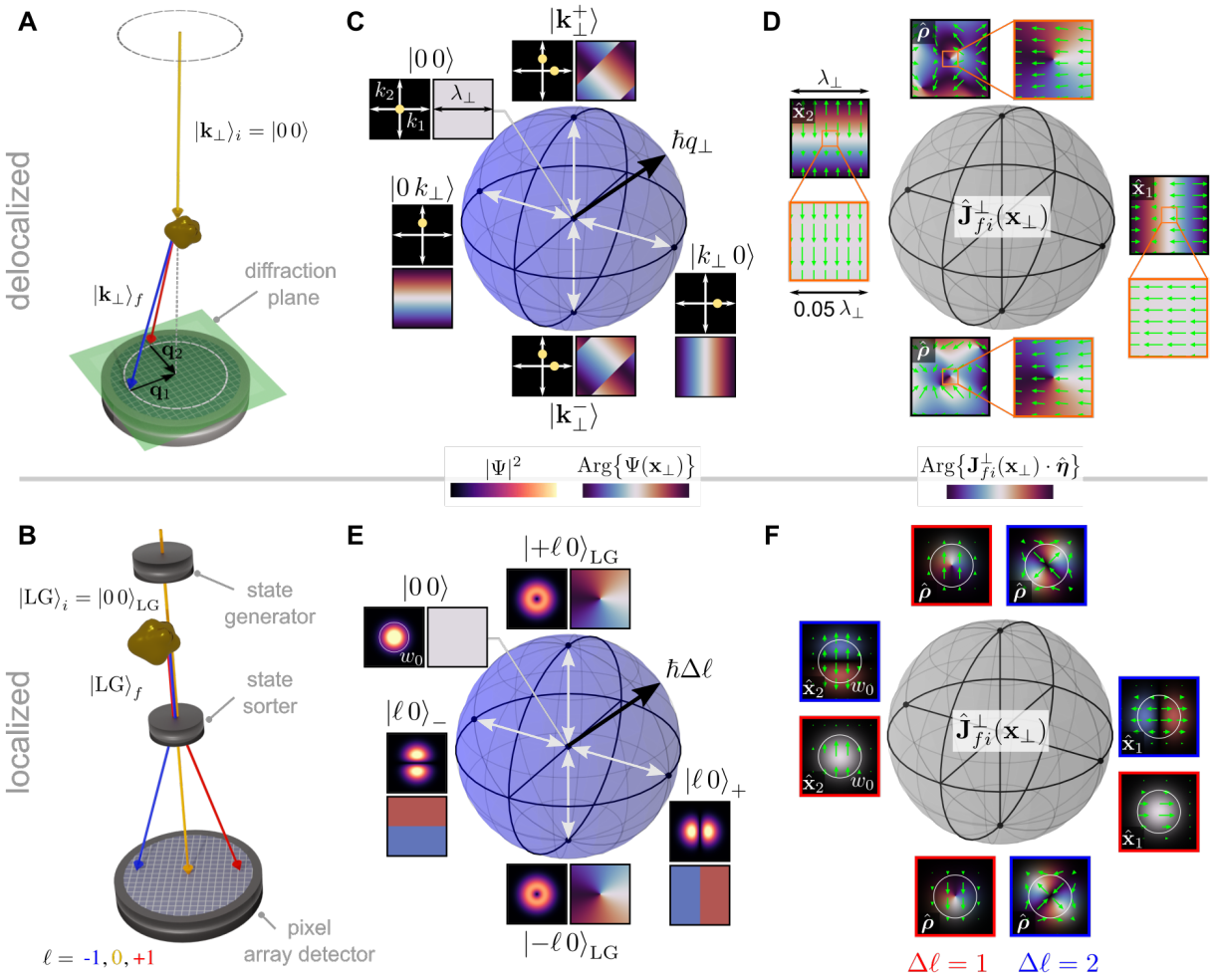

Figure 4.2: **Optical polarization analogs in phase-shaped EELS.** Schemes showing (**A**) plane wave $|0\,0\rangle \rightarrow |\mathbf{k}_\perp\rangle_f$ LM-resolved and (**B**) Laguerre-Gauss $|0\,0\rangle_{\mathrm{LG}} \rightarrow |\mathrm{LG}\rangle_f$ OAM-resolved EEL measurements. (**C**) Schematic representation of transitions between the $|0\,0\rangle$ transverse plane wave state with constant phase (sphere center) and other states with transverse wave vector magnitude $k_\perp$ and non-uniform phase arranged around the Poincaré sphere. Reciprocal space probability densities and real space transverse phase profiles over one transverse wavelength $\lambda_\perp = 2\pi/|\mathbf{q}_\perp|$ are shown for the states at the four antipodal points indicated. (**D**) Spatial maps of the transition current density $\mathbf{J}^\perp_{fi}(\mathbf{x}_\perp, x_3 = 0)$ (green arrows) for transverse state transitions represented by white arrows in panel (C). Underlying color maps represent the phase profiles of $\mathbf{J}^\perp_{fi}(\mathbf{x}_\perp)\cdot\hat{\boldsymbol{\eta}}$, where $\hat{\boldsymbol{\eta}}$ is noted within each plot. (**E**) Schematic representation of transitions between the $|0\,0\rangle_{\mathrm{LG}}$ state and superposition states with $\hbar\ell$ units of OAM arranged around the Poincaré sphere. Real space probability density and transverse phase profiles are shown for the states at the four antipodal states indicated for $\ell = 1$. The radius of the white circle is equal to the beam waist w_0. (**F**) $\mathbf{J}^\perp_{fi}(\mathbf{x}_\perp, x_3 = 0)$ (green arrows) for transverse state transitions represented by white arrows in panel (E) for $\Delta\ell = 1$ (red) and $\Delta\ell = 2$ (blue). Underlying color maps represent the phase profiles of $\mathbf{J}^\perp_{fi}(\mathbf{x}_\perp)\cdot\hat{\boldsymbol{\eta}}$.

Importantly, the requisite pre- and post-selection transverse phase measurements underlying the OPA construction presented here are currently achievable; LM- and OAM-resolved EEL processes, shown schematically in Figures 4.2A and 4.2b, respectively, constitute two well-known examples of such measurements. In its simplest realization, the LM-resolved measurement involves the preparation of an initial plane wave state $|\mathbf{k}_i\rangle$, which evolves into a different superposition of plane wave states via interaction with the target specimen. Post-selection of the final transverse state $|\mathbf{k}_f\rangle$ fixes the LM transfer $\hbar\mathbf{q} = \hbar(\mathbf{k}_i - \mathbf{k}_f)$ and can be accomplished via spatial filtering within the diffraction plane [117, 131]. Similarly, figure 4.2B depicts OAM-resolved EEL processes, where OAM state generators [104, 132–134] and sorters [47, 102] perform selection of initial and final vortex states with well-defined OAM. An expanded discussion of experimental considerations concerning phase-shaped EELS measurements is provided in the Supplementary Materials.

Consider, for example, transitions between electron plane wave states $|\mathbf{k}\rangle = |\mathbf{k}_\perp\rangle\,|k_3\rangle$, where $|\mathbf{k}_\perp\rangle = |k_1\,k_2\rangle$ denotes the transverse LM state with $|0\,0\rangle$ defining the plane wave oriented along the TEM axis. Figure 4.2C shows a Poincaré sphere with the surface composed of all transverse plane wave states with fixed transverse wave vector magnitude $k_\perp$, and the $|0\,0\rangle$ state characterized by constant spatial phase profile at the sphere center. For any transitions between the $|0\,0\rangle$ state and a state on the sphere surface, the transverse linear momentum transfer $\hbar\mathbf{q}_\perp = \hbar\mathbf{k}_\perp$ fixes the radius of the sphere. Spanning the equatorial plane are the $|k_\perp\,0\rangle$ and $|0\,k_\perp\rangle$ states characterized by phase profiles independent of x_2 and x_1, respectively. The superposition states $|\mathbf{k}_\perp^{\pm}\rangle = (1/\sqrt{2})[|k_\perp\,0\rangle \pm i\,|0\,k_\perp\rangle]$ are located at the vertical pair of antipodal points. The reciprocal space wave function density and real space transverse phase are shown over one transverse wavelength $\lambda_\perp = 2\pi/|\mathbf{q}_\perp|$ for the four antipodal points indicated.

Although $|0\,0\rangle \rightarrow |0\,0\rangle$ transitions lead to $\hat{\mathbf{J}}_{fi}(\mathbf{x})$ purely along $\hat{\mathbf{x}}_3$, $\mathbf{J}_{fi}(\mathbf{x}) = (-\hbar e/2mL^3)(2\mathbf{k}_i - \mathbf{q})e^{i\mathbf{q}\cdot\mathbf{x}}$ if the final state consists of a single plane wave component with wave vector $\mathbf{k}_f$, where $\mathbf{J}_{fi}^{\perp}(\mathbf{x}) \propto \mathbf{q}_\perp e^{i\mathbf{q}\cdot\mathbf{x}}$ and L is the box quantization length. Figure 4.2D presents $\mathbf{J}_{fi}^{\perp}(\mathbf{x}_\perp, x_3 = 0)$ for transitions between the $|0\,0\rangle$ state and the four antipodal states on the surface of the sphere in Figure 4.2C (marked as white arrows). The spatial periodicity of the plane wave wave functions is inherited by $\mathbf{J}_{fi}^{\perp}(\mathbf{x}_\perp)$, leading to spatial variation of the sign of the $\hat{\mathbf{x}}_1$ and $\hat{\mathbf{x}}_2$ components of $\mathbf{J}_{fi}^{\perp}(\mathbf{x}_\perp)$ at the equatorial antipodal points, as well as sign and orientation variation at the vertically oriented antipodal points. However, when $|\mathbf{q}_\perp|d \ll 1$, where d is the characteristic transverse length scale of the target, the magnified regions in Figure 4.2D show $\hat{\mathbf{J}}_{fi}^{\perp}(\mathbf{x})$ becomes approximately independent of position and is oriented along $\hat{\mathbf{q}}_\perp$ in the vicinity of the target. Thus, the resulting $\hat{\mathbf{J}}_{fi}^{\perp} \approx \hat{\mathbf{q}}_\perp$ Poincaré sphere becomes equivalent to that used to characterize optical plane wave polarization states in Figure 4.1C. This is precisely the dipole limit discussed previously in the core-loss literature identifying $\hat{\mathbf{q}}_\perp$ as the OPA in plane wave based measurements [54, 77, 79, 118].

Meanwhile, another Poincaré sphere can be constructed using the cylindrically symmetric and transversely localized Laguerre-Gauss (LG) $|\ell\,p\rangle_{\mathrm{LG}}$ transverse states (Figure 4.2E), where $\hbar\ell$ is the OAM, p labels the number of radial nodes, and w_0 is the beam waist. The $|\pm\ell\,0\rangle_{\mathrm{LG}}$ and superposition states $|\ell\,0\rangle_{+} = (1/\sqrt{2})\big(\,|+\ell\,0\rangle_{\mathrm{LG}} + |-\ell\,0\rangle_{\mathrm{LG}}\,\big)$ and $|\ell\,0\rangle_{-} = (1/i\sqrt{2})\big(\,|+\ell\,0\rangle_{\mathrm{LG}} - |-\ell\,0\rangle_{\mathrm{LG}}\,\big)$ are located at the vertical

and equatorial antipodal points, respectively. As in Figure 4.2C, the $|0\,0\rangle_{\mathrm{LG}}$ state with constant transverse phase is positioned at the sphere center such that transitions between the state at the center and states on the sphere surface are associated with transfers of $\Delta\ell$ units of OAM. The real space wave function densities and transverse phase profiles are presented for $\Delta\ell = 1$. $\mathbf{J}_{fi}(\mathbf{x})$ acquires components transverse to $\hat{\mathbf{x}}_3$ only when there is a transition between transverse free electron states. Figure 4.2F shows $\mathbf{J}^{\perp}_{fi}(\mathbf{x}_{\perp})$ for transitions (marked as white arrows in Figure 4.2E) between the uniform phase state at the sphere center and the four antipodal points shown on the surface for $\Delta\ell = 1$ (red) and $\Delta\ell = 2$ (blue). While the $\Delta\ell = 2$ transition current densities possess the symmetries required to excite quadrupolar target excitations, they do not constitute an OPA as defined here due to the spatial variation of $\hat{\mathbf{J}}^{\perp}_{fi}(\mathbf{x}_{\perp})$. This situation reflects the general relationship [41] between the LG OAM states and the Hermite-Gauss (HG) states, the latter of which are separable in the Cartesian coordinate system. Only in the particular case of $\Delta\ell = 1$ are the equatorial antipodal states related to the first order HG states, characterized by phase profiles independent of y and x, respectively, by $|\ell = 1\,0\rangle_{\pm} = |{}^{1\,0}_{0\,1}\rangle_{\mathrm{HG}}$ [48]. In this case, the orientation and spatial phase profiles of $\hat{\mathbf{J}}^{\perp}_{fi}$ at the four $\Delta\ell = 1$ antipodal points of Figure 4.2F are identical to those associated with the electric field of circularly polarized light presented in Figure 4.1C, satisfying the necessary OPA conditions.

Due to the delocalized (localized) nature of the plane wave (LG/HG) states, it is conventional to describe EEL measurements involving plane wave and LG/HG states in terms of the double differential scattering cross section $\partial^2\sigma/\partial E_{if}\partial\Omega$ and the state- and energy-resolved EEL probability Γ_{fi} observables, respectively. Specializing to the Cartesian coordinate system with $(x, y, z) = (\mathbf{R}, z)$ and impact parameter $\mathbf{R} = \mathbf{R}_0$, both observables are related to $w^{\mathrm{loss}}_{fi}(\omega)$ in Eq. (4.1) by (see Materials and Methods)

$$\begin{bmatrix} \frac{\partial^2\sigma}{\partial E_{if}\partial\Omega} \\ \Gamma_{fi}(\mathbf{R}_0,\omega) \end{bmatrix} = \begin{bmatrix} -L^6\left(\frac{2m}{4\pi\hbar^2}\right)^2\left(\frac{k_f}{k_i}\right)\int\frac{d(\hbar\omega)}{2\pi} \\ \frac{mL^2}{\hbar^2 k_i}\int\frac{dq_{\parallel}}{2\pi} \end{bmatrix} \times w^{\mathrm{loss}}_{fi}(\omega), \tag{4.4}$$

where $\gamma_{i/f} = 1/\sqrt{1-(v^0_{i/f}/c)^2}$, $k_{i/f} = mv_{i/f}/\hbar = \gamma_{i/f}mv^0_{i/f}/\hbar$, $v^0_{i/f}$ are the initial and final electron speeds, and the non-recoil approximation $\delta(\omega - \omega_{if}) \approx (1/v_i)\delta(q_{\parallel} - \omega/v_i)$ is invoked in the lower expression. These observables are compared for a representative nanophotonic system composed of two 60 nm × 30 nm × 15 nm Ag rods with a 10 nm surface-to-surface gap along the dimer ($\hat{\mathbf{y}}$) axis.

Figures 4.3A,B show normalized $\partial^2\sigma/\partial E_{if}\partial\Omega$ spectra (log scale) for 200 keV electrons in the loss energy window containing the rods' coupled surface plasmon modes, which were computed by adapting the *e*-DDA code [135, 136] to evaluate the observables in Eq. (4.4) using Eqs. (4.1) and (4.2) as described in the Supplementary Materials. In Figure 4.3A, the incoming electron plane wave is aligned along the TEM axis $(\theta, \phi) = (0, 0)$ and the outgoing plane waves emerge at angles $(\theta, \phi) = (0 - 20\ \mu\mathrm{rad}, \pi/2)$ such that $\hat{\mathbf{q}}_{\perp}$ is purely along $\hat{\mathbf{y}}$. In this low-loss regime, the dipole limit with $d_y \lesssim 0.05\lambda_{\perp}$ (Figure 4.2C) is achieved for $\theta \lesssim 1$ μrad. As expected, the spectrum in Figure 4.3A for $\theta = 1$ μrad is dominated by the bonding dipole mode at 2.31 eV, which is accessible by optical plane wave excitation polarized along $\hat{\mathbf{q}}_{\perp} = \hat{\mathbf{y}}$ (see Figure S1). A

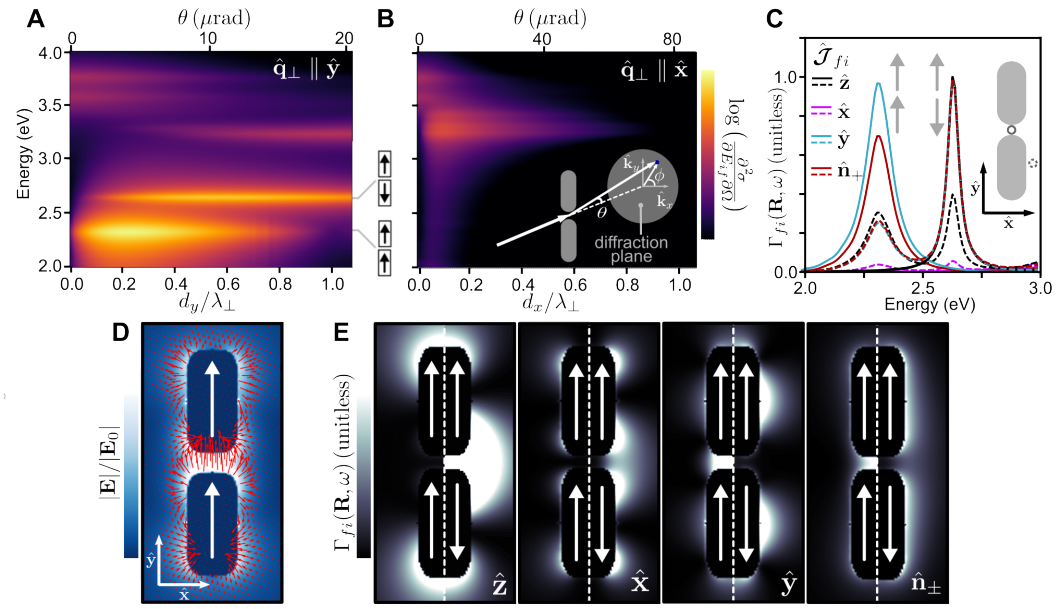

Figure 4.3: **Phase-shaped EEL measurements of an Ag rod dimer system.** (**A**) Double differential inelastic scattering cross section in the low-loss spectral region for scattering angles $(\theta, \phi) = (0 - 20\ \mu\text{rad}, \pi/2)$ such that $\mathbf{q}_\perp = q_\perp \hat{\mathbf{y}}$. (**B**) Same as (A) but for scattering angles $(\theta, \phi) = (0 - 80\ \mu\text{rad}, 0)$ such that $\mathbf{q}_\perp = q_\perp \hat{\mathbf{x}}$. (**C**) $\Gamma_{fi}(\mathbf{R}, \omega)$ within the spectral region containing the bonding (2.31 eV) and antibonding (2.64 eV) hybridized dipole modes for $\mathbf{R}_0$ on (solid) and off (dashed) the center of mass position. Trace colors denote $\hat{\boldsymbol{\mathcal{J}}}_{fi}$, where $\hat{\mathbf{n}}_\pm = (1/\sqrt{2})(\hat{\mathbf{x}} \pm i\hat{\mathbf{y}})$. (**D**) Optically-induced response field at the bonding mode energy for incident wave vector along $\hat{\mathbf{z}}$ and polarization along $\hat{\mathbf{y}}$. In-plane xy components of the vector field are shown in red. (**E**) Polarization-resolved spectrum images of bonding (left) and antibonding (right) modes for transitions between first order LG/HG states and the Gaussian state. $\hat{\boldsymbol{\mathcal{J}}}_{fi}$ is labeled in each spectrum image.

direct comparison is presented in Figure S2 of the double differential inelastic electron scattering and optical extinction cross section spectra for small electron scattering angles. As the detection angle increases in Figure 4.3A, $\lambda_\perp$ decreases and higher order excitations such as the $\hat{\mathbf{y}}$ oriented antibonding mode at 2.64 eV grow into the spectra [137]. Figure 4.3B presents $\partial^2\sigma/\partial E_{if}\partial\Omega$ spectra for detection angles $(\theta, \phi) = (0 - 80\ \mu\text{rad}, 0)$, such that $\hat{\mathbf{q}}_\perp$ is along $\hat{\mathbf{x}}$. Besides the longitudinally oriented modes above 3.5 eV that dominate at $\theta = 0$ in panels (A) and (B), the modes near 3.25 eV in the optical extinction spectra under $\hat{\mathbf{x}}$ polarization appear for $\mathbf{q}_x \neq 0$ (see Figure S1). A clear connection between optical $\sigma_{\text{ext}}(\omega)$ and $\partial^2\sigma/\partial E_{if}\partial\Omega$ exists at small detection angles consistent with the dipole limit (Figure 4.2D). The required angular resolution ($\lesssim 1\ \mu$rad in the present case) is currently achievable experimentally [131, 132, 138, 139].

In the case of localized LG state transitions (Figure 4.2E), Γ_{fi} can be put into the form

$$\Gamma_{fi}(\mathbf{R}_0, \omega) = \frac{-1}{\pi\hbar^2\omega}\text{Re}\left\{\int d\mathbf{R}dz\ \mathbf{J}^*_{fi}(\mathbf{R}, z, \omega) \cdot \mathbf{E}_{fi}(\mathbf{R}, z, \omega)\right\} \tag{4.5}$$

by introducing the induced field $\mathbf{E}_{fi}(\mathbf{x}, \omega) = -4\pi i\omega \int d\mathbf{x}'\ \mathbf{G}(\mathbf{x}, \mathbf{x}', \omega) \cdot \mathbf{J}_{fi}(\mathbf{x}', \omega)$ sourced by the transition current density $\mathbf{J}_{fi}(\mathbf{x}, \omega) = (mL/\hbar k_i)\mathbf{J}_{fi}(\mathbf{x})$ in the presence of the target, with $\omega = q_\parallel v_i$ within the non-

recoil approximation as explained in the Materials and Methods. When w_0 is small such that $\mathbf{E}_{fi}(\mathbf{x},\omega) \approx \mathbf{E}_{fi}(\mathbf{R}_0,z,\omega)$,

$$\Gamma_{fi}(\mathbf{R}_0,\omega) = \frac{-1}{\pi\hbar^2\omega}\mathrm{Re}\left\{\boldsymbol{\mathcal{J}}_{fi}^{*}\cdot\int dz\,\mathbf{E}_{fi}(\mathbf{R}_0,z,\omega)e^{-i\omega z/v_i}\right\}, \tag{4.6}$$

where $\boldsymbol{\mathcal{J}}_{fi} = \int d\mathbf{R}\,\mathbf{J}_{fi}(\mathbf{R},\omega)\,e^{-i\omega z/v_i} = (-e/mv_i)\{\langle\Psi_f|\hat{\mathbf{p}}_\perp|\Psi_i\rangle + \left[(2p_i-\hbar q_\parallel)/2\right]\langle\Psi_f|\Psi_i\rangle\,\hat{\mathbf{z}}\}$. Therefore, in the narrow beam limit, the observable $\Gamma_{fi}(\mathbf{R}_0,\omega)$ is proportional to the real part of the Fourier expansion coefficient of the target response field for the particular plane wave component propagating along the TEM axis with wave vector magnitude equal to the longitudinal transfer momentum $q_\parallel = \omega/v_i$ and polarization direction $\hat{\boldsymbol{\mathcal{J}}}_{fi}^{*}$. In this limit, $\hat{\boldsymbol{\mathcal{J}}}_{fi}^{\perp} = \mathbf{0}$ unless $\Delta\ell = \pm 1$ in which case $\hat{\boldsymbol{\mathcal{J}}}_{fi}^{\perp} = \hat{\mathbf{J}}_{fi}^{\perp} = \hat{\mathbf{d}}_{fi}^{\perp}$ (see Supplementary Materials) as shown in Figure 4.2F. Figure 4.3C presents $\Gamma_{fi}(\mathbf{R},\omega)$ evaluated numerically with the e-DDA code [135, 136, 140] as discussed in Supplementary Materials using Eq. (4.6) for $\hat{\boldsymbol{\mathcal{J}}}_{fi}^{\perp}$ at the antipodal points in Figure 4.2F as well as $\hat{\boldsymbol{\mathcal{J}}}_{fi}^{\perp} \parallel \hat{\mathbf{z}}$ for the transition $|0\,0\rangle_{\mathrm{LG}} \rightarrow |0\,0\rangle_{\mathrm{LG}}$ within the spectral region containing the bonding and antibonding hybridized dipole modes. Trace colors denote $\hat{\boldsymbol{\mathcal{J}}}_{fi}$, while solid and dashed lines indicate $\mathbf{R}_0$ positioned at, or displaced from, respectively, the dimer center of mass. At the center of mass position, a conventional EEL process with no transition between transverse state (solid black) does (does not) couple to the optically dark (bright) antibonding (bonding) mode. In contrast, when $\hat{\boldsymbol{\mathcal{J}}}_{fi} = \hat{\boldsymbol{\mathcal{J}}}_{fi}^{\perp}$, the loss functions exhibit peaks at the bonding, but not antibonding, mode. When $\mathbf{R}_0$ is displaced to a position of lower symmetry, all electron scattering processes considered couple to both bonding and antibonding modes.

Polarization-resolved spectrum images can be collected via hyperspectral imaging by scanning $\mathbf{R}_0$ over the target specimen. Although $\Gamma_{fi}(\mathbf{R},\omega)$ is nonlocal in the z-direction [80, 81], conventional ($\hat{\boldsymbol{\mathcal{J}}}_{fi} = \hat{\mathbf{z}}$) and polarization-resolved ($\hat{\boldsymbol{\mathcal{J}}}_{fi} = \hat{\boldsymbol{\mathcal{J}}}_{fi}^{\perp}$) spectrum images can often be rationalized by considering the electric field (Figure 4.3D). Figure 4.3E presents polarization-resolved spectrum images for loss energies matching the bonding (left) and antibonding (right) mode energy, and for transitions between electron transverse states indicated by the transition current unit vector $\hat{\boldsymbol{\mathcal{J}}}_{fi}$ labeled in each image. It is evident upon comparison of the spectrum images at the bonding mode energy and Figure 4.3D that the regions of space where $\Gamma_{fi}(\mathbf{R},\omega)$ is large closely track positions where $\mathbf{E}\cdot\hat{\boldsymbol{\mathcal{J}}}_{fi}$ is appreciable. The polarization-resolved spectrum images at the antibonding energy exhibit the expected nodal behavior at the origin for each $\hat{\boldsymbol{\mathcal{J}}}_{fi}$. This example demonstrates the additional wealth of information that can be accessed using OPAs in phase-shaped EEL measurements, highlighting commonalities and differences arising for pre- and post-selection of transverse plane wave and LG/HG states.

4.4 Discussion

Owing to recently developed experimental techniques for manipulating free electron wave functions, inelastic electron scattering between selected phase-shaped transverse states is emerging as a powerful addition to the rapidly-developing nanoscale imaging toolset. By employing a fully quantum mechanical treatment that explicitly accounts for the transverse electron degrees of freedom with fully-retarded light-matter interactions,

we show that the transition current density $\mathbf{J}^{\perp}_{fi}$ plays the role of OPA in EEL measurements, and provide a general prescription for constructing OPAs that mimic the polarization properties of free space optical plane waves. The insight gained from the perspective suggested by our approach is used to demonstrate an underlying connection between the two ostensibly distinct OPAs previously identified in the core- and low-loss regimes under wide-field and focused beam conditions, respectively, and discuss the conditions required to most closely approximate ideal OPAs. Example calculations for a plasmonic rod dimer are presented to highlight the utility of phase-shaped EEL nanospectroscopy for determining mode symmetries and for probing the 3D polarization-resolved response field of a target with nanoscale spatial resolution. Although primary focus is placed on developing free space photon OPAs, the procedure outlined for constructing $\hat{\mathbf{J}}^{\perp}_{fi}$ along arbitrary curvilinear coordinate directions is general and can be applied to generate more exotic structured light [130] analogs that can couple to other desired target mode symmetries. The fully-retarded formalism employed here is consistent with that used to describe laser-stimulated phase-shaped electron energy gain measurements [5], setting the stage for time-resolved phase-shaped measurements in ultrafast TEMs [101, 141]. The ability to perform high-fidelity pre- and post-selection of the free electron state, as well as understanding the role of transverse state coherence and its ability to be manipulated, in conventional and ultrafast TEM experiments remains a current area of interest to experiment and theory. These techniques complement other methods with state-of-the-art time and space resolution such as interferometric time-resolved photoemission electron microscopy [63], which has been employed to image nanoscale spin and field textures with nontrivial topology [142].

4.5 Materials and Methods

4.5.1 State- and Frequency-Resolved Electron Energy Loss Rate

Within the first Born approximation, the rate at which a free electron prepared in initial state $|i\rangle$ transitions to a final state $|f\rangle$, while simultaneously depositing a single excitation into the ℓth target mode (i.e., $|0_\ell\rangle \to |1_\ell\rangle$), is given by Fermi's golden rule

$$w^{\text{loss}}_{fi} = \frac{2\pi}{\hbar}\left|\langle f|\langle n_\ell|\hat{V}|0_\ell\rangle|i\rangle\right|^2 \delta(E^{\text{total}}_f - E^{\text{total}}_i). \tag{4.7}$$

Using the identify $\delta(E^{\text{total}}_f - E^{\text{total}}_i) = \hbar^{-1}\int d\omega\, \delta(\omega - \omega_{if})\delta(\omega - \omega_\ell)$, where $\hbar\omega_{if}$ is the energy loss of the free electron and $\hbar\omega_\ell$ is the energy of the excited target mode, the frequency-resolved transition rate can be expressed as

$$w^{\text{loss}}_{fi}(\omega) = \frac{2\pi}{\hbar^2}\left|\langle f|\langle 1_\ell|\hat{V}|0_\ell\rangle|i\rangle\right|^2 \delta(\omega - \omega_{if})\delta(\omega - \omega_\ell). \tag{4.8}$$

Working in the generalized Coulomb gauge [128] defined by $\nabla\cdot[\varepsilon(\mathbf{x})\mathbf{A}(\mathbf{x},t)] = 0$ with zero scalar potential, the interaction potential is $\hat{V} = (e/2mc)(\hat{\mathbf{A}}\cdot\hat{\mathbf{p}} + \hat{\mathbf{p}}\cdot\hat{\mathbf{A}})$, and the matrix element for an arbitrary electron transition ($|i\rangle \to |f\rangle$) can be written in terms of the transition current density $\mathbf{J}_{fi}$ defined in Eq. (4.2).

Explicitly,

$$\begin{aligned}
\langle f|\hat{V}|i\rangle &= \frac{e}{2mc}\int d\mathbf{x}\, d\mathbf{x}'\, \langle f|\mathbf{x}'\rangle\langle \mathbf{x}'|\hat{\mathbf{A}}\cdot\hat{\mathbf{p}}+\hat{\mathbf{p}}\cdot\hat{\mathbf{A}}|\mathbf{x}\rangle\langle\mathbf{x}|i\rangle \\
&= \frac{-i\hbar e}{2mc}\int d\mathbf{x}\, \hat{\mathbf{A}}(\mathbf{x})\cdot\psi_f^*(\mathbf{x})\nabla\psi_i(\mathbf{x}) - \frac{i\hbar e}{2mc}\int d\mathbf{x}\left(\psi_f^*(\mathbf{x})\psi_i(\mathbf{x})\big[\nabla\cdot\hat{\mathbf{A}}(\mathbf{x})\big]+\hat{\mathbf{A}}(\mathbf{x})\cdot\psi_f^*(\mathbf{x})\nabla\psi_i(\mathbf{x})\right) \\
&= \frac{-2i\hbar e}{2mc}\int d\mathbf{x}\, \hat{\mathbf{A}}(\mathbf{x})\cdot\psi_f^*(\mathbf{x})\nabla\psi_i(\mathbf{x}) - \frac{i\hbar e}{2mc}\int d\mathbf{x}\,\psi_f^*(\mathbf{x})\psi_i(\mathbf{x})\big[\nabla\cdot\hat{\mathbf{A}}(\mathbf{x})\big] \\
&= \frac{-2i\hbar e}{2mc}\int d\mathbf{x}\, \hat{\mathbf{A}}(\mathbf{x})\cdot\psi_f^*(\mathbf{x})\nabla\psi_i(\mathbf{x}) + \frac{i\hbar e}{2mc}\int d\mathbf{x}\,\hat{\mathbf{A}}(\mathbf{x})\cdot\Big\{\nabla\psi_f^*(\mathbf{x})\psi_i(\mathbf{x})+\psi_f^*(\mathbf{x})\nabla\psi_i(\mathbf{x})\Big\} \\
&= \frac{-1}{c}\int d\mathbf{x}\,\hat{\mathbf{A}}(\mathbf{x})\cdot\frac{i\hbar e}{2m}\Big\{\psi_f^*(\mathbf{x})\nabla\psi_i(\mathbf{x})-\psi_i(\mathbf{x})\nabla\psi_f^*(\mathbf{x})\Big\} \\
&= -\frac{1}{c}\int d\mathbf{x}\,\hat{\mathbf{A}}(\mathbf{x})\cdot\mathbf{J}_{fi}(\mathbf{x}).
\end{aligned} \tag{4.9}$$

In going from the third to fourth lines of Eq. (4.9), the surface term generated by integrating by parts has been assumed to vanish. The total transition rate associated with electron energy loss $\hbar\omega_{if}$ is found by summing over all possible final excited states of the target, which are denoted by ℓ in Eq. (4.8). This is facilitated by expanding the vector potential as $\mathbf{A}(\mathbf{x},t) = \sum_n \hat{a}_n^\dagger \mathbf{A}_n^{(-)}(\mathbf{x})e^{+i\omega_n t} + \hat{a}_n\mathbf{A}_n^{(+)}(\mathbf{x})e^{-i\omega_n t}$, where $\mathbf{A}_n^{(+)}(\mathbf{x}) = c\sqrt{2\pi\hbar/\omega_n}\,\mathbf{f}_n(\mathbf{x})$ and $\mathbf{A}_n^{(-)}(\mathbf{x}) = c\sqrt{2\pi\hbar/\omega_n}\,\mathbf{f}_n^*(\mathbf{x})$ are the positive and negative frequency components of the vector potential written in terms of spatial mode functions $\mathbf{f}_n(\mathbf{x})$, which satisfy the generalized Helmholtz equation. Since we are considering only electron energy loss, $\sum_\ell \langle 1_\ell|\hat{\mathbf{A}}(\mathbf{x}',t)|0_\ell\rangle = \sum_{n\ell} c\sqrt{2\pi\hbar/\omega_\ell}\,\mathbf{f}_\ell^*(\mathbf{x}')e^{i\omega_\ell t}\delta_{n\ell} = \sum_n \mathbf{A}_n^{(-)}(\mathbf{x}')$ and consequently for the conjugate process, $\sum_\ell \langle 0_\ell|\hat{\mathbf{A}}(\mathbf{x},t)|1_\ell\rangle^* = \sum_{n\ell} c\sqrt{2\pi\hbar/\omega_\ell}\,\mathbf{f}_\ell(\mathbf{x})e^{-i\omega_\ell t}\delta_{n\ell} = \sum_n \mathbf{A}_n^{(+)}(\mathbf{x})$. Inserting these matrix elements into Eq. (4.8) yields main text Eq. (5.9), i.e.,

$$\begin{aligned}
w_{fi}^{\text{loss}}(\omega) &= \sum_\ell \frac{2\pi}{c^2\hbar^2}\big|\langle 1_\ell|\int d\mathbf{x}\,\hat{\mathbf{A}}(\mathbf{x})\cdot\mathbf{J}_{fi}(\mathbf{x})|0_\ell\rangle\big|^2\delta(\omega-\omega_{if})\delta(\omega-\omega_\ell) \\
&= \sum_n \frac{2\pi}{c^2\hbar^2}\int d\mathbf{x}\,d\mathbf{x}'\,\big[\mathbf{A}_n^{(+)}(\mathbf{x})\cdot\mathbf{J}_{fi}^*(\mathbf{x})\big]\big[\mathbf{A}_n^{(-)}(\mathbf{x})\cdot\mathbf{J}_{fi}(\mathbf{x}')\big]\delta(\omega-\omega_{if})\delta(\omega-\omega_n) \\
&= \frac{4\pi^2}{\hbar}\int d\mathbf{x}\,d\mathbf{x}'\,\mathbf{J}_{fi}^*(\mathbf{x})\cdot\left[\sum_n\frac{1}{\omega_n}\mathbf{f}_n(\mathbf{x})\mathbf{f}_n^*(\mathbf{x}')\delta(\omega-\omega_n)\right]\cdot\mathbf{J}_{fi}(\mathbf{x}')\delta(\omega-\omega_{if}) \\
&= \frac{4\pi^2}{\hbar}\int d\mathbf{x}\,d\mathbf{x}'\,\mathbf{J}_{fi}^*(\mathbf{x})\cdot\left[-\frac{2}{\pi}\text{Im}\Big\{\mathbf{G}(\mathbf{x},\mathbf{x}',\omega)\Big\}\right]\cdot\mathbf{J}_{fi}(\mathbf{x}')\delta(\omega-\omega_{if}) \\
&= \frac{4\pi^2}{\hbar\omega}\int d\mathbf{x}\,d\mathbf{x}'\,\mathbf{J}_{fi}^*(\mathbf{x})\cdot\boldsymbol{\varrho}(\mathbf{x},\mathbf{x}',\omega)\cdot\mathbf{J}_{fi}(\mathbf{x}')\delta(\omega-\omega_{if}),
\end{aligned} \tag{4.10}$$

where $\mathbf{G}(\mathbf{x},\mathbf{x}',\omega)$ is the dyadic Green's function [101], which connects the electric field produced at point $\mathbf{x}$ to the sourcing current density $\mathbf{J}(\mathbf{x}',\omega)$ through the relationship

$$\mathbf{E}(\mathbf{x},\omega) = -4\pi i\omega\int d\mathbf{x}'\mathbf{G}(\mathbf{x},\mathbf{x}',\omega)\cdot\mathbf{J}(\mathbf{x}',\omega). \tag{4.11}$$

Due to the reciprocity property of the Green's dyadic $\mathbf{G}(\mathbf{x}_1, \mathbf{x}_2, \omega) = \mathbf{G}^{\mathbf{T}}(\mathbf{x}_2, \mathbf{x}_1, \omega)$,

$$\int d\mathbf{x}\, d\mathbf{x}'\, \mathbf{J}_{fi}^*(\mathbf{x}) \cdot \mathrm{Im}\Big\{\mathbf{G}(\mathbf{x}, \mathbf{x}', \omega)\Big\} \cdot \mathbf{J}_{fi}(\mathbf{x}') = \int d\mathbf{x}\, d\mathbf{x}'\, \mathrm{Im}\big\{\mathbf{J}_{fi}^*(\mathbf{x}) \cdot \mathbf{G}(\mathbf{x}, \mathbf{x}', \omega) \cdot \mathbf{J}_{fi}(\mathbf{x}')\big\}, \tag{4.12}$$

and Eq. (4.10) can be alternatively expressed as

$$\begin{aligned} w_{fi}^{\mathrm{loss}}(\omega) &= \frac{4\pi^2}{\hbar} \int d\mathbf{x}\, d\mathbf{x}'\, \mathbf{J}_{fi}^*(\mathbf{x}) \cdot \Big[-\frac{2}{\pi} \mathrm{Im}\Big\{\mathbf{G}(\mathbf{x}, \mathbf{x}', \omega)\Big\}\Big] \cdot \mathbf{J}_{fi}(\mathbf{x}') \delta(\omega - \omega_{if}) \\ &= -\frac{8\pi}{\hbar} \int d\mathbf{x}\, d\mathbf{x}'\, \mathrm{Im}\Big\{\mathbf{J}_{fi}^*(\mathbf{x}) \cdot \mathbf{G}(\mathbf{x}, \mathbf{x}', \omega) \cdot \mathbf{J}_{fi}(\mathbf{x}')\Big\} \delta(\omega - \omega_{if}). \end{aligned} \tag{4.13}$$

4.5.2 Optical Extinction Cross Section

The optical plane wave extinction cross section for an isolated dipolar target is

$$\sigma_{\mathrm{ext}}(\omega) = 4\pi \frac{\omega}{c} \mathrm{Im}\big\{\hat{\boldsymbol{\epsilon}}^* \cdot \boldsymbol{\alpha}(\omega) \cdot \hat{\boldsymbol{\epsilon}}\big\}, \tag{4.14}$$

where $\boldsymbol{\alpha}(\omega)$ is the dipole polarizability tensor characterizing the target response to plane wave excitation with polarization unit vector $\hat{\boldsymbol{\epsilon}}$. This expression can alternatively be expressed as

$$\sigma_{\mathrm{ext}}(\omega) = 4\pi \frac{\omega}{c} \frac{1}{|\mathbf{E}_{\hat{\boldsymbol{\epsilon}}}(\mathbf{x}_t, \omega)|^2} \mathrm{Im}\Big\{\mathbf{E}_{\hat{\boldsymbol{\epsilon}}}^*(\mathbf{x}_t, \omega) \cdot \boldsymbol{\alpha}(\omega) \cdot \mathbf{E}_{\hat{\boldsymbol{\epsilon}}}(\mathbf{x}_t, \omega)\Big\}, \tag{4.15}$$

where $\mathbf{E}_{\hat{\boldsymbol{\epsilon}}}(\mathbf{x}_t)$ is the plane wave electric field at the position of the target $\mathbf{x}_t$. A plane wave with polarization $\hat{\boldsymbol{\epsilon}}$ directed along $\hat{\mathbf{k}}$ can be viewed as though sourced by a point dipole at position $\mathbf{x}_p$ with current density $\mathbf{J}_{\hat{\boldsymbol{\epsilon}}}(\mathbf{x}, \omega) = -i\omega p \delta(\mathbf{x} - \mathbf{x}_p)\hat{\boldsymbol{\epsilon}}$ and $\hat{\mathbf{k}} = -\hat{\mathbf{x}}_p$ [101], since

$$\begin{aligned} \mathbf{E}_{\hat{\boldsymbol{\epsilon}}}(\mathbf{x}, \omega) &= -4\pi i\omega \int d\mathbf{x}' \mathbf{G}_0(\mathbf{x}, \mathbf{x}', \omega) \cdot \mathbf{J}_{\hat{\boldsymbol{\epsilon}}}(\mathbf{x}', \omega) \\ &= \Big[k^2 \mathbf{I} + \nabla\nabla\Big] \frac{e^{ik|\mathbf{x} - \mathbf{x}_p|}}{|\mathbf{x} - \mathbf{x}_p|} \cdot p\hat{\boldsymbol{\epsilon}}, \end{aligned} \tag{4.16}$$

where $\mathbf{J}_{\hat{\boldsymbol{\epsilon}}}$ and $\mathbf{E}_{\hat{\boldsymbol{\epsilon}}}$ are understood to oscillate harmonically as $e^{-i\omega t}$ and the free space Green dyadic is

$$\mathbf{G}_0(\mathbf{x}, \mathbf{x}', \omega) = -\frac{1}{4\pi\omega^2} \Big[k^2 \mathbf{I} + \nabla\nabla\Big] \frac{e^{ik|\mathbf{x} - \mathbf{x}'|}}{|\mathbf{x} - \mathbf{x}'|}. \tag{4.17}$$

Taking the source dipole position $\mathbf{x}_p$ to be a large distance from the target and using the fact that $\hat{\mathbf{k}} = -\hat{\mathbf{x}}_p$,

$$\mathbf{G}_0(\mathbf{x}, \mathbf{x}', \omega) \to -\frac{k^2}{4\pi\omega^2} \frac{e^{ik|\mathbf{x} - \mathbf{x}'|}}{|\mathbf{x} - \mathbf{x}'|} \mathbf{I}, \tag{4.18}$$

and

$$\mathbf{E}_{\hat{\boldsymbol{\epsilon}}}(\mathbf{x}, \omega) \to \frac{i}{\omega} \int d\mathbf{x}' k^2 \frac{e^{ik|\mathbf{x} - \mathbf{x}'|}}{|\mathbf{x} - \mathbf{x}'|} \mathbf{I} \cdot \mathbf{J}_{\hat{\boldsymbol{\epsilon}}}(\mathbf{x}', \omega), \tag{4.19}$$

which establishes that $\mathbf{E}_{\hat{\boldsymbol{\epsilon}}} \parallel \mathbf{J}_{\hat{\boldsymbol{\epsilon}}} \parallel \hat{\boldsymbol{\epsilon}}$ as desired. The optical extinction cross section can therefore be written as

$$\begin{aligned}
\sigma_{\text{ext}}(\omega) &= 4\pi\frac{\omega}{c}\frac{1}{|\mathbf{E}_{\hat{\boldsymbol{\epsilon}}}(\mathbf{x}_t,\omega)|^2}\text{Im}\left\{\int d\mathbf{x}\, d\mathbf{x}'\, \mathbf{J}^*_{\hat{\boldsymbol{\epsilon}}}(\mathbf{x},\omega)\cdot(+4\pi i\omega)\mathbf{G}_0(\mathbf{x},\mathbf{x}_t)\cdot\boldsymbol{\alpha}(\omega)\cdot(-4\pi i\omega)\mathbf{G}_0(\mathbf{x}_t,\mathbf{x}')\cdot\mathbf{J}_{\hat{\boldsymbol{\epsilon}}}(\mathbf{x}',\omega)\right\} \\
&= -4\pi\frac{\omega}{c}\frac{1}{|\mathbf{E}_{\hat{\boldsymbol{\epsilon}}}(\mathbf{x}_t,\omega)|^2}\text{Im}\left\{\int d\mathbf{x}\, d\mathbf{x}'\, \mathbf{J}^*_{\hat{\boldsymbol{\epsilon}}}(\mathbf{x},\omega)\cdot(+4\pi i\omega)\mathbf{G}_0(\mathbf{x},\mathbf{x}_t)\cdot\boldsymbol{\alpha}(\omega)\cdot(-4\pi i\omega)\mathbf{G}_0(\mathbf{x}_t,\mathbf{x}')\cdot\mathbf{J}_{\hat{\boldsymbol{\epsilon}}}(\mathbf{x}',\omega)\right\} \\
&= -4\pi\frac{\omega}{c}\frac{1}{|\mathbf{E}_{\hat{\boldsymbol{\epsilon}}}(\mathbf{x}_t,\omega)|^2}\text{Im}\left\{\int d\mathbf{x}\, d\mathbf{x}'\, \mathbf{J}^*_{\hat{\boldsymbol{\epsilon}}}(\mathbf{x},\omega)\cdot\mathbf{G}(\mathbf{x},\mathbf{x}',\omega)\cdot\mathbf{J}_{\hat{\boldsymbol{\epsilon}}}(\mathbf{x}',\omega)\right\}
\end{aligned} \tag{4.20}$$

where

$$\mathbf{G}(\mathbf{x},\mathbf{x}',\omega) = (+4\pi i\omega)\mathbf{G}_0(\mathbf{x},\mathbf{x}_t)\cdot\boldsymbol{\alpha}(\omega)\cdot(-4\pi i\omega)\mathbf{G}_0(\mathbf{x}_t,\mathbf{x}'), \tag{4.21}$$

with the form of $\mathbf{G}_0$ defined in Eq. (4.18).

Target responses beyond the single dipole approximation can be evaluated using the discrete dipole approximation [140], whereby the continuous target is represented by a collection of dipoles interacting self-consistently under a driving field $\mathbf{E}_{\hat{\boldsymbol{\epsilon}}}$. In this case, $\mathbf{G}(\mathbf{x},\mathbf{x}',\omega)$ can be expanded as [48, 87]

$$\mathbf{G}(\mathbf{x},\mathbf{x}',\omega) = \sum_{jj'}(+4\pi i\omega)\mathbf{G}_0(\mathbf{x},\mathbf{x}_j,\omega)\cdot\left(\boldsymbol{\alpha}^{-1}+4\pi\omega^2\mathbf{G}_0\right)^{-1}_{jj'}\cdot(-4\pi i\omega)\mathbf{G}_0(\mathbf{x}'_{j'},\mathbf{x}',\omega). \tag{4.22}$$

4.5.3 Optical Polarization Analogs

Suppose that the free electron wave function can be separated within an orthogonal coordinate system with variables x_1, x_2, x_3, i.e., $\psi(\mathbf{x}) = \Psi_1(x_1)\Psi_2(x_2)\Psi_3(x_3)$, then the transverse transition current can be expressed as

$$\begin{aligned}
\mathbf{J}^{\perp}_{fi}(\mathbf{x}) &= \frac{i\hbar e}{2m}\Big\{\Psi^*_{\perp f}(\mathbf{x}_\perp)\big[\nabla_\perp\Psi_{\perp i}(\mathbf{x}_\perp)\big] - \Psi_{\perp i}(\mathbf{x}_\perp)\big[\nabla_\perp\Psi^*_{\perp f}(\mathbf{x}_\perp)\big]\Big\}\Psi^*_{3f}(x_3)\Psi_{3i}(x_3) \\
&= \frac{i\hbar e}{2m}\Big\{\Psi^*_{1f}(x_1)\Psi^*_{2f}(x_2)\big[\nabla_\perp\Psi_{1i}(x_1)\Psi_{2i}(x_2)\big] - \Psi_{1i}(x_1)\Psi_{2i}(x_2)\big[\nabla_\perp\Psi^*_{1f}(x_1)\Psi^*_{2f}(x_2)\big]\Big\}\Psi^*_{3f}(x_3)\Psi_{3i}(x_3) \\
&= \frac{i\hbar e}{2m}\Big\{\Psi^*_{1f}(x_1)\Psi^*_{2f}(x_2)\left[\frac{1}{h_1}\frac{\partial\Psi_{1i}(x_1)}{\partial x_1}\Psi_{2i}(x_2)\hat{\mathbf{x}}_1 + \frac{1}{h_2}\Psi_{1i}(x_1)\frac{\partial\Psi_{2i}(x_2)}{\partial x_2}\hat{\mathbf{x}}_2\right] + \\
&\qquad - \Psi_{1i}(x_1)\Psi_{2i}(x_2)\left[\frac{1}{h_1}\frac{\partial\Psi^*_{1f}(x_1)}{\partial x_1}\Psi^*_{2f}(x_2)\hat{\mathbf{x}}_1 + \frac{1}{h_2}\Psi^*_{1f}(x_1)\frac{\partial\Psi^*_{2f}(x_2)}{\partial x_2}\hat{\mathbf{x}}_2\right]\Big\}\Psi^*_{3f}(x_3)\Psi_{3i}(x_3) \\
&= \frac{i\hbar e}{2m}\Big\{\frac{1}{h_1}\Psi^*_{2f}(x_2)\Psi_{2i}(x_2)\left[\Psi^*_{1f}(x_1)\frac{\partial\Psi_{1i}(x_1)}{\partial x_1} - \Psi_{1i}(x_1)\frac{\partial\Psi^*_{1f}(x_1)}{\partial x_1}\right]\hat{\mathbf{x}}_1 + \\
&\qquad + \frac{1}{h_2}\Psi^*_{1f}(x_1)\Psi_{1i}(x_1)\left[\Psi^*_{2f}(x_2)\frac{\partial\Psi_{2i}(x_2)}{\partial x_2} - \Psi_{2i}(x_2)\frac{\partial\Psi^*_{2f}(x_2)}{\partial x_2}\right]\hat{\mathbf{x}}_2\Big\}\Psi^*_{3f}(x_3)\Psi_{3i}(x_3)
\end{aligned} \tag{4.23}$$

where h_μ is the scale factor associated with coordinate x_μ. It is evident that the $\hat{\mathbf{x}}_\mu$ component of the transition current density vanishes when

$$\Psi^*_{f\nu}\Psi_{i\nu}\left[\Psi^*_{f\mu}\frac{\partial\Psi_{i\mu}}{\partial x_\mu} - \Psi_{i\mu}\frac{\partial\Psi^*_{f\mu}}{\partial x_\mu}\right] = 0, \tag{4.24}$$

where $\mu, \nu = 1, 2$ with $\mu \neq \nu$. Provided $\Psi^*_{f\nu}\Psi_{i\nu} \neq 0$, and writing the wave function in polar form $\Psi_\mu = A(x_\mu)e^{i\phi(x_\mu)}$ with $A \in \mathbb{R}_{>0}$ and $\phi \in [0, 2\pi]$, this condition can be rewritten as

$$A_f\left[\frac{\partial A_i}{\partial x_\mu} + i\phi_i A_i \frac{\partial \phi_i}{\partial x_\mu}\right] = A_i\left[\frac{\partial A_f}{\partial x_\mu} - i\phi_f A_f \frac{\partial \phi_f}{\partial x_\mu}\right]. \tag{4.25}$$

If $f = i$ and $\phi_i = \phi_f = \phi$, then this becomes

$$\frac{\partial \phi}{\partial x_\mu} = -\frac{\partial \phi}{\partial x_\mu}. \tag{4.26}$$

This condition is satisfied if the phase ϕ is strictly constant. In summary, the $\hat{\mathbf{x}}_\mu$ component of $\mathbf{J}^\perp_{fi}$ vanishes provided (1) $\Psi_{i\mu}(x_\mu) = \Psi_{f\mu}(x_\mu)$, and (2) $\mathrm{Arg}\{\Psi_\mu(x_\mu)\}$ is constant.

OPAs can be defined, therefore, provided that pairs of initial $\Psi_{\perp i}$ and final $\Psi_{\perp f}$ free electron transverse states can be identified such that the conditions

$$\begin{aligned}
\Psi^*_{f\nu}\Psi_{i\nu}\left[\Psi^*_{f\mu}\frac{\partial \Psi_{i\mu}}{\partial x_\mu} - \Psi_{i\mu}\frac{\partial \Psi^*_{f\mu}}{\partial x_\mu}\right] &= 0 \\
\Psi^*_{f\mu}\Psi_{i\mu}\left[\Psi^*_{f\nu}\frac{\partial \Psi_{i\nu}}{\partial x_\nu} - \Psi_{i\nu}\frac{\partial \Psi^*_{f\nu}}{\partial x_\nu}\right] &\neq 0
\end{aligned} \tag{4.27}$$

may be simultaneously satisfied. In such cases, a Poincaré sphere may be defined from $\hat{\mathbf{J}}^\perp_{fi} \in \{\hat{\mathbf{x}}_1, \hat{\mathbf{x}}_2, \hat{\mathbf{x}}_\pm = (1/\sqrt{2})(\hat{\mathbf{x}}_1 \pm i\hat{\mathbf{x}}_2)\}$, and it is possible to realize $\hat{\mathbf{J}}^\perp_{fi}$ at an arbitrary point on this Poincaré sphere using suitable coherent superpositions of the initial and final wavefunctions used to define the antipodal points. Two examples of such a Poincaré sphere construction within the Cartesian coordinate systems are presented in Figures 4.2D,F, which involve transitions between wave functions constructed from states with well-defined linear momentum (Figure 4.2C) and OAM (Figure 4.2E), respectively. The cases of radially $\hat{\boldsymbol{\rho}}$ and azimuthally $\hat{\boldsymbol{\varphi}}$ polarized $\hat{\mathbf{J}}^\perp_{fi}$ are discussed in the Supplementary Materials and shown in Figure S3.

4.5.4 Fully-Retarded Double Differential Inelastic Scattering Cross Section

The total frequency-resolved inelastic scattering cross section $\sigma(\omega)$ can be defined by dividing the state- and frequency-resolved loss rate $w^{\mathrm{loss}}_{fi}(\omega)$ from Eq. (4.13) by the incoming plane wave particle flux $\hbar k_i/mL^3$ and summing over final electron states with $\sum_{\mathbf{k}_f} \to \left(L/2\pi\right)^3 \int d\mathbf{k}_f$, which gives

$$\begin{aligned}
\sigma(\omega) &= \frac{mL^3}{\hbar k_i}\left(\frac{L}{2\pi}\right)^3 \int d\mathbf{k}_f w^{\mathrm{loss}}_{fi}(\omega) \\
&= \frac{mL^3}{\hbar k_i}\left(\frac{L}{2\pi}\right)^3 \int d\Omega\, dk_f\, k_f^2 w^{\mathrm{loss}}_{fi}(\omega).
\end{aligned} \tag{4.28}$$

The angular- and frequency-resolved cross section is then

$$\frac{\partial \sigma(\omega)}{\partial \Omega} = \frac{mL^3}{\hbar k_i}\left(\frac{L}{2\pi}\right)^3 \int dk_f\, k_f^2 w^{\mathrm{loss}}_{fi}(\omega). \tag{4.29}$$

In addition to integrating out the explicit frequency dependence, the integral over the final wave vector magnitude can be expressed as an integral over loss energy E_{if} due to the relativistic energy-momentum free particle dispersion relation. Explicitly, $dE_{if} = -(\hbar^2/m)k_f dk_f$, and

$$\frac{\partial\sigma}{\partial\Omega} = -L^6\left(\frac{2m}{4\pi\hbar^2}\right)^2 \int dE_{if} \left(\frac{k_f}{k_i}\right) \int \frac{d(\hbar\omega)}{2\pi}\, w_{fi}^{\text{loss}}(\omega), \tag{4.30}$$

where $k_{i/f} = mv_{i/f} = \gamma_{i/f} m v_{i/f}^0/\hbar$ and $\gamma_{i/f} = 1/\sqrt{1-(v_{i/f}^0/c)^2}$. Consequently,

$$\begin{aligned}\frac{\partial^2\sigma}{\partial E_{if}\partial\Omega} &= -L^6\left(\frac{2m}{4\pi\hbar^2}\right)^2 \left(\frac{k_f}{k_i}\right) \int \frac{d(\hbar\omega)}{2\pi}\, w_{fi}^{\text{loss}}(\omega) \\ &= -L^6\left(\frac{2m}{4\pi\hbar^2}\right)^2 \frac{\hbar}{2\pi}\left(\frac{k_f}{k_i}\right) w_{fi}^{\text{loss}}(\omega_{if}),\end{aligned} \tag{4.31}$$

which is identical to the double differential inelastic scattering cross section given in main text Eq. (4.4). Explicit analytic double differential cross section expressions in the case of an isolated dipolar target, discussion of the quasistatic limit of this theory, and additional details concerning numerical evaluation of the double differential cross section are included in the Supplementary Materials.

4.5.5 Fully-Retarded State- and Energy-resolved EEL Probability and the Narrow Beam Limit

The energy-resolved loss probability is found by multiplying the frequency-resolved loss rate in Eq. (4.13) by the time required for the electron to traverse the quantization length ($mL/\hbar k_i$), and by summing over all the possible final electron momenta directed along the TEM axis (with $k_f^z \parallel q_\parallel$), and dividing by $\hbar$, giving

$$\begin{aligned}\Gamma_{fi}(\mathbf{R}_0,\omega) &= \frac{mL^2}{\hbar^2 k_i}\int \frac{dq_\parallel}{2\pi}\, w_{fi}^{\text{loss}}(\omega) \\ &= -\frac{4}{\hbar}\frac{k_i}{m}\int dq_\parallel \int d\mathbf{x}\, d\mathbf{x}' \text{Im}\left\{\frac{mL}{\hbar k_i}\,\mathbf{J}_{fi}^*(\mathbf{x})\cdot\mathbf{G}(\mathbf{x},\mathbf{x}',\omega)\cdot\frac{mL}{\hbar k_i}\,\mathbf{J}_{fi}(\mathbf{x}')\right\}\delta(\omega-\omega_{if}),\end{aligned} \tag{4.32}$$

which is equivalent to the form given in main text Eq. (4.4). This state- and energy-resolved EEL probability can be re-expressed in terms of the induced electric field sourced by $\mathbf{J}_{fi}$ in the presence of the target using (4.11) with $\mathbf{J}_{fi}(\mathbf{x},\omega) = (mL/\hbar k_i)\mathbf{J}_{fi}(\mathbf{x})$. This yields

$$\begin{aligned}\Gamma_{fi}(\mathbf{R}_0,\omega) &= -\frac{4k_i}{\hbar m}\int dq_\parallel \,\text{Im}\left\{\int d\mathbf{x}\,\frac{mL}{\hbar k_i}\,\mathbf{J}_{fi}^*(\mathbf{x})\cdot\left(\frac{-1}{4i\pi\omega}\right)\mathbf{E}_{fi}(\mathbf{x},\omega)\right\}\delta(\omega-\omega_{if}) \\ &= -\int dq_\parallel \,\text{Re}\left\{\frac{k_i}{\pi m\hbar\omega}\int d\mathbf{x}\,\frac{mL}{\hbar k_i}\,\mathbf{J}_{fi}^*(\mathbf{x})\cdot\mathbf{E}_{fi}(\mathbf{x},\omega)\right\}\delta(\omega-\omega_{if}).\end{aligned} \tag{4.33}$$

The integral over longitudinal momentum transfers can be performed trivially by invoking the non-recoil approximation [68], whereby the energy associated with transverse recoils is neglected during the consideration of the trailing energy-conserving delta function in Eq. (4.33). The connection between ω_{if} and $q_\parallel$ is found

within the limit of $q_\parallel \ll k_i, k_f$ as

$$\begin{aligned} E_{if} \equiv \hbar\omega_{if} &= \sqrt{(mc^2)^2 + (c\hbar k_i)^2} - \sqrt{(mc^2)^2 + (c\hbar k_f)^2} \\ &= mc^2\sqrt{1 + \left(\frac{c\hbar k_i}{mc^2}\right)^2} - mc^2\sqrt{1 + \left(\frac{c\hbar k_f}{mc^2}\right)^2} \\ &\approx mc^2\left[1 + \frac{1}{2}\left(\frac{c\hbar k_i}{mc^2}\right)^2\right] - mc^2\left[1 + \frac{1}{2}\left(\frac{c\hbar k_f}{mc^2}\right)^2\right] \\ &= mc^2\frac{1}{2}\left(\frac{c\hbar k_i}{mc^2}\right)^2 - mc^2\frac{1}{2}\left(\frac{c\hbar k_f}{mc^2}\right)^2 \\ &= \frac{\hbar^2}{2m}(k_i^2 - k_f^2), \end{aligned} \tag{4.34}$$

such that $\omega_{if} \approx v_i q_\parallel$.

As a result,

$$\begin{aligned} \Gamma_{fi}(\mathbf{R}_0, \omega) &= -\frac{k_i}{\pi m\hbar\omega}\int dq_\parallel \,\mathrm{Re}\Big\{\int d\mathbf{x}\,\frac{mL}{\hbar k_i}\,\mathbf{J}_{fi}^*(\mathbf{x})\cdot\mathbf{E}_{fi}(\mathbf{x},\omega)\Big\}\delta\big(\omega - q_\parallel v_i\big) \\ &= -\frac{1}{\pi\hbar^2\omega}\int dq_\parallel \,\mathrm{Re}\Big\{\int d\mathbf{R}\,dz\,\frac{mL}{\hbar k_i}\,\mathbf{J}_{fi}^*(\mathbf{R},z)\cdot\mathbf{E}_{fi}(\mathbf{R},z,\omega)\Big\}\delta\big(q_\parallel - \omega/v_i\big) \\ &= -\frac{1}{\pi\hbar^2\omega}\mathrm{Re}\Big\{\int d\mathbf{R}\,dz\,\mathbf{J}_{fi}^*(\mathbf{R},z,\omega)\cdot\mathbf{E}_{fi}(\mathbf{R},z,\omega)\Big\}, \end{aligned} \tag{4.35}$$

which is main text Eq. (4.5). In the final line, the longitudinal momentum transfer appearing in $\mathbf{J}_{fi}(\mathbf{R},z,\omega)$ and $\mathbf{E}_{fi}(\mathbf{R},z,\omega)$ is locked to $q_\parallel = \omega/v_i$. The explicit connection between this fully-retarded form of the loss function and the quasistatic version in Ref. [48] is presented in the Supplementary Materials.

When the beam waist of the electron probe w_0 is small compared to the length scale over which the response field changes, then $\mathbf{E}_{fi}$ is approximately constant over the spatial domain where the current density is appreciable, allowing $\mathbf{E}_{fi}(\mathbf{R},z,\omega) \approx \mathbf{E}_{fi}(\mathbf{R}_0,z,\omega)$ in the last line of Eq. (4.35). The EEL probability in the narrow beam width limit, therefore, is

$$\begin{aligned} \Gamma_{fi}(\mathbf{R}_0, \omega) &\approx \frac{-1}{\pi\hbar^2\omega}\mathrm{Re}\Big\{\int d\mathbf{R}\,dz\,\mathbf{J}_{fi}^*(\mathbf{R},z,\omega)\cdot\mathbf{E}_{fi}(\mathbf{R}_0,z,\omega)\Big\} \\ &= \frac{-1}{\pi\hbar^2\omega}\mathrm{Re}\Big\{\int dz\,\Big[\int d\mathbf{R}\,\mathbf{J}_{fi}^*(\mathbf{R},z,\omega)\Big]\cdot\mathbf{E}_{fi}(\mathbf{R}_0,z,\omega)\Big\} \\ &= \frac{-1}{\pi\hbar^2\omega}\mathrm{Re}\Big\{\int dz\,\Big[\int d\mathbf{R}\,\mathbf{J}_{fi}^*(\mathbf{R},z,\omega)e^{i\omega z/v_i}\Big]e^{-i\omega z/v_i}\cdot\mathbf{E}_{fi}(\mathbf{R}_0,z,\omega)\Big\} \\ &= \frac{-1}{\pi\hbar^2\omega}\mathrm{Re}\Big\{\int dz\,\Big[\int d\mathbf{R}\,\mathbf{J}_{fi}^*(\mathbf{R},\omega)\Big]e^{-i\omega z/v_i}\cdot\mathbf{E}_{fi}(\mathbf{R}_0,z,\omega)\Big\} \\ &= \frac{-1}{\pi\hbar^2\omega}\mathrm{Re}\Big\{\boldsymbol{\mathcal{J}}_{fi}^*\cdot\int dz\,\mathbf{E}_{fi}(\mathbf{R}_0,z,\omega)e^{-i\omega z/v_i}\Big\}, \end{aligned} \tag{4.36}$$

where $\boldsymbol{\mathcal{J}}_{fi} = \int d\mathbf{R}\,\mathbf{J}_{fi}(\mathbf{R},\omega)\,e^{-i\omega z/v_i} = (-e/mv_i)\big\{\langle\Psi_f|\hat{\mathbf{p}}_\perp|\Psi_i\rangle + \big[(2p_i - \hbar q_\parallel)/2\big]\,\langle\Psi_f|\Psi_i\rangle\,\hat{\mathbf{z}}\big\}$ is z-independent. Additional details and analytic expressions for $\mathbf{J}_{fi}(\mathbf{x},\omega)$ and $\boldsymbol{\mathcal{J}}_{fi}$ in the case of transitions between localized

Hermite-Gauss and Laguerre-Gauss transverse states are included in the Supplementary Materials.

4.6 Acknowledgments

All work was supported by the U.S. Department of Energy (DOE), Office of Science, Office of Basic Energy Sciences (BES), Materials Sciences and Engineering Division under Award No. DOE BES DE-SC0022921. **Author contributions:** M.B. and D.M. conceived the project and devised the theoretical formalism. A.N. contributed to the general theoretical formalism and derived the analytic expressions for the transition currents and fields as well as the observables in the dipole limit. M.C. implemented the derived expressions in the *e*-DDA code and performed the numerical calculations. All authors contributed to the analysis and discussions. M.B. wrote the original manuscript. All authors contributed to the final manuscript. D.M. supervised the project. **Competing interests:** All authors declare that they have no competing interests. **Data and materials availability:** All data needed to evaluate the conclusions in the paper are present in the paper and/or the Supplementary Materials.

Chapter 5

Inelastic scattering of transversely structured free electrons from nanophotonic targets: Theory and computation

- Austin G. Nixon, Matthieu Chalifour, Marc R. Bourgeois, Michael Sanchez, and David J. Masiello. Inelastic scattering of transversely structured free electrons from nanophotonic targets: Theory and computation. *Phys. Rev. A*, 109:043502, Apr 2024. [3]

5.1 Introduction

Leveraging recent instrumental advancements in energy monochromation and aberration correction, inelastic scattering of free electrons has become an effective technique to spectroscopically characterize and image atomic and molecular [143–145], biological [146–148], solid state [124, 149–152], and nanophotonic [153, 154] systems with unprecedented spatial resolution. Simultaneously, optical spectroscopies and microscopies based upon the absorption, scattering, extinction, and emission of electromagnetic waves continue to be indispensable tools used to probe the same systems, albeit with spatial resolution limitations imposed by the optical diffraction limit. Light-based spectromicroscopies can often be enhanced by taking advantage of optical selection rules stemming from the intrinsic linear and spin angular momentum degrees of freedom of the photon [155]. In addition to the polarization degrees of freedom arising from the intrinsic spin angular momentum, photons can also be prepared in specific orbital angular momentum (OAM) states defined by

the azimuthal phase $e^{i\ell\phi}$ [41]. Due to the helical nature of their spiralling phase fronts, light beams characterized by such a quantized topological charge ℓ are commonly referred to as optical vortex or twisted light beams [156,157]. Motivated in part by the infinite dimensional Hilbert space offered by the OAM basis [158], the ability to prepare [159], sort [160], and measure [161] these optical OAM states has driven applications in quantum information science using photons with quantized azimuthal and radial labels [157, 162–166]. Moreover, transverse sculpting of the radiation field in general, has lead to the development of new gauge transformations, such as the twisted light gauge [167, 168], construction of free space optical skyrmionic beams [169], excitations of forbidden transitions in atomic isotopes [170], and the use of vortex γ ray photons to selectively probe high energy resonances in photonuclear reactions [171].

Unlike photons, electrons prepared and measured in currently available TEMs, STEMs, or ultrafast TEMs (UTEMs) are accurately described by the spinless free particle Schrödinger equation and consequently lack intrinsic polarization degrees of freedom [157]. Despite this limitation, linear-momentum-based selection rules based on quantum mechanical treatments of the inelastic scattering process have been long understood and exploited in core-loss EEL spectroscopy [76, 79, 172, 173] and have enabled measurements of magnetic circular dichroism [54, 77, 118, 174–176], characterization of site-specific defects in atomic crystals [177], as well as visualization of the electromagnetic fields of atomic-scale systems [117]. Inspired by the creation and manipulation of optical vortex states, developments of techniques for shaping the transverse phase profile [178] and OAM content of free electrons via holographic masks [44, 46, 179], spiral phase plates [45], and shaped laser pulses [133, 180] has been at the forefront of low-loss EEL spectroscopy ($\lesssim 50$ eV) [68]. Furthermore, borrowing ideas from quantum optics, the preparation of free electron qubits carrying information in the form of quantized energy or OAM states using laser pulses [100,181,182], holographic masks, or spiral phase plates [183–185], has driven the continued development of free electrons as holders and propagators of quantum information. In parallel, the ability to generate phase-structured incident electron states and sort them based upon their OAM content [47] has fueled numerous investigations of inelastic electron scattering between states with pre- and post-selected transverse phase profiles in the low-loss regime [4, 5, 48, 49, 87–89, 127, 186, 187].

In this paper, we expound upon a recently introduced theoretical framework describing the fully retarded inelastic scattering of phase-shaped free electron beams in the electron microscope [4]. Specifically, with emphasis placed on the low-loss regime, we investigate the theory of transversely phase-shaped EEL spectroscopy in both narrow beam and wide field limits and laser-stimulated EEG spectroscopy in the narrow beam limit. Sec. 5.1 presents a derivation of the energy-resolved inelastic electron scattering rate, including both EEL and EEG processes. Transversely structured free electron states that can be prepared within currently available TEMs and STEMs are subsequently reviewed in Sec. 5.2. Section 5.3 introduces the transition current density associated with transitions between such states. Expressions for EEL and EEG observables are derived in Sec. 5.4 for both wide field and focused electron beams, including those with nonuniform transverse phase-structure, such as twisted electron beams. Numerical implementation of the presented inelastic electron scattering theory based on the method of coupled dipoles is described in Sec.

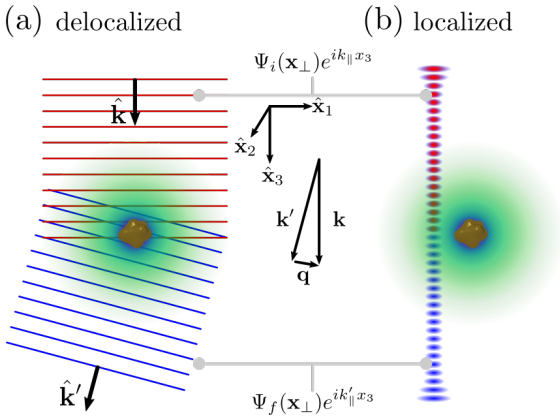

Figure 5.1: Scheme showing the inelastic scattering of transversely delocalized and localized free electrons with wave functions of the separable form $\Psi(\mathbf{x}_\perp)e^{ik_\parallel x_3}$. (a) Initial electron plane wave (red) with wave vector $\mathbf{k} = (\mathbf{k}_\perp, k_\parallel)$ interacting with the vector potential (shaded green) of a target specimen. Following the interaction, the electron is post-selected for the plane wave state $\mathbf{k}' = (\mathbf{k}'_\perp, k'_\parallel)$ (blue). The momentum recoil wave vector associated with this transition is $\mathbf{q} = \mathbf{k} - \mathbf{k}'$. (b) A transversely localized electron beam with pre-selected transverse wave function $\Psi_i(\mathbf{x}_\perp)$ (red) interacting with the same target and post-selected in $\Psi_f(\mathbf{x}_\perp)$ (blue).

5.5, including EEL and EEG probabilities and the EEL double differential scattering cross section (DDCS). Numerical calculations are presented for prototypical nanophotonic systems, underscoring particular advantages of our numerical approach, including its: (1) flexibility regarding target size, shape, composition, and number, (2) facile extension to accommodate arbitrary initial and final free electron transverse states, and (3) ability to capture signatures of matter-wave diffraction and interference arising from scattering from individual and multiple nanoscale targets. Gaussian units are used throughout.

Inelastic free electron scattering: State- and energy-resolved EEL and EEG rates

Here we review the retarded theory of inelastic electron scattering for the calculation of EEL and laser-stimulated EEG processes [4, 5, 68, 75, 80, 90–92, 94]. The target material is described through its bound electromagnetic responses characterized by dielectric function $\xi(\omega)$, while the electron probe is examined for both delocalized and localized electron wave functions. The light-matter potential governing such interactions takes the form

$$\hat{V} = \frac{e}{2mc}\Big(\hat{\mathbf{A}}\cdot\hat{\mathbf{p}} + \hat{\mathbf{p}}\cdot\hat{\mathbf{A}}\Big) \tag{5.1}$$

under minimal coupling in the generalized Coulomb gauge [128] $\nabla\cdot\xi(\mathbf{x})\hat{\mathbf{A}}(\mathbf{x},t) = 0$, where the $\hat{\rho}\hat{\Phi}$ term makes no contribution in the absence of free charges describing the target. The probing electron's charge and mass are $-e$ and m, and c is the speed of light in vacuum. $\hat{\mathbf{A}}$ and $\hat{\mathbf{p}}$ are quantum mechanical operators for the vector potential of the target and linear momentum of the free electron probe, respectively.

Owing to the inherently weak nature of electron-photon coupling, the inelastic scattering probability can be obtained using first order time-dependent perturbation theory. The transition rate describing the scattering of an electron from initial state $|\psi_i\rangle$ to final state $|\psi_f\rangle$ while simultaneously exciting/de-exciting the target from initial state $|\Phi_\nu\rangle$ to final state $|\Phi_{\nu'}\rangle$ is given by

$$w_{fi} = \frac{2\pi}{\hbar} \sum_{\nu\nu'} \left| \langle \Phi_{\nu'} | \langle \psi_f | \hat{V} | \psi_i \rangle | \Phi_\nu \rangle \right|^2 \delta(E_f - E_i), \tag{5.2}$$

where $E_i = \hbar\varepsilon_i + \hbar\omega_\nu$ and $E_f = \hbar\varepsilon_f + \hbar\omega_{\nu'}$ are the initial and final energies of the composite system, $\hbar\varepsilon_{i/f} = \gamma_{i/f} mc^2$ represents the initial/final energy of the probing electron, and $\gamma_{i/f} = \left[1 - (v_{i/f}/c)^2\right]^{-1/2}$ are the initial/final Lorentz contraction factors. Sec. 5.2 details specific TEM and STEM electron states, including those that are phase-shaped transversely to their propagation direction (see Fig. 4.1), but for now we remain agnostic to their identity. After some algebra, the transition matrix elements of the scattering potential in Eq. (5.1) can be expressed as

$$\begin{aligned} V_{\nu' f \nu i}(t) &= \langle \Phi_{\nu'} | \langle \psi_f | \hat{V}(t) | \psi_i \rangle | \Phi_\nu \rangle \\ &= \langle \Phi_{\nu'} | -\frac{1}{c} \int d\mathbf{x}\, \mathbf{A}(\mathbf{x}, t) \cdot \mathbf{J}_{fi}(\mathbf{x}, t) | \Phi_\nu \rangle, \end{aligned} \tag{5.3}$$

where $\mathbf{J}_{fi}(\mathbf{x}, t) = \mathbf{J}_{fi}(\mathbf{x}) e^{-i(\varepsilon_i - \varepsilon_f)t}$ is the transition current density [4] with

$$\mathbf{J}_{fi}(\mathbf{x}) = \frac{i\hbar e}{2m} \left[\psi_f^*(\mathbf{x}) \nabla \psi_i(\mathbf{x}) - \psi_i(\mathbf{x}) \nabla \psi_f^*(\mathbf{x}) \right] \tag{5.4}$$

defined in terms of the probe scattering states $\psi_i(\mathbf{x}, t) = \psi_i(\mathbf{x}) e^{-i\varepsilon_i t}$ and $\psi_f(\mathbf{x}, t) = \psi_f(\mathbf{x}) e^{-i\varepsilon_f t}$. By continuity, i.e., $\nabla \cdot \mathbf{J}_{fi}(\mathbf{x}, t) = -\dot{\rho}_{fi}(\mathbf{x}, t)$, $\mathbf{J}_{fi}(\mathbf{x}, t)$ is connected to the transition charge density $\rho_{fi}(\mathbf{x}, t) = -e\psi_f^*(\mathbf{x}, t)\psi_i(\mathbf{x}, t)$.

EEL and EEG scattering rates each derive from Eq. (5.3), but involve different vector potentials of distinct physical origin. In the case of EEL, solving the vector Helmholtz equation on the domain of the target produces a set of eigenmode functions $\mathbf{f}_\nu(\mathbf{x})$ and associated eigenmode frequencies ω_ν [1], which serve as a basis to expand the target vector potential [128]. In terms of this set $\{\mathbf{f}_\nu(\mathbf{x})\}_\nu$, $\mathbf{A}(\mathbf{x}, t) = \sum_\nu [\mathbf{A}_\nu^{(+)}(\mathbf{x}) a_\nu e^{-i\omega_\nu t} + \mathbf{A}_\nu^{(-)}(\mathbf{x}) a_\nu^\dagger e^{i\omega_\nu t}]$, with $\mathbf{A}_\nu^{(+)}(\mathbf{x}) = c\sqrt{2\pi\hbar/\omega_\nu}\mathbf{f}_\nu(\mathbf{x})$, $\mathbf{A}_\nu^{(-)}(\mathbf{x}) = c\sqrt{2\pi\hbar/\omega_\nu}\mathbf{f}_\nu^*(\mathbf{x})$, and $[\mathbf{A}_\nu^{(+)}]^\dagger = \mathbf{A}_\nu^{(-)}$, where $a_\nu^\dagger$ (a_ν) are creation (annihilation) operators responsible for inducing optical excitations (de-excitations) in the νth target mode. In the case of EEG, the target vector potential can still be expanded onto the $\{\mathbf{f}_\nu(\mathbf{x})\}_\nu$ basis, however, it is the response vector potential induced by a stimulating laser field. In either case, Eq.

[1] As presented, the eigenmode expansion of the vector potential is rigorously correct only for lossless dielectric cavities. Losses can be incorporated from the outset by instead expanding the vector potential onto the basis of quasinormal modes [188–190]. The resulting EEL rate expressions exhibit equivalent dependence on the Green's dyadic irrespective of the presence or absence of losses

(5.3) becomes

$$V_{\nu' f\nu i}(t) = -\frac{1}{c}\Big[\sqrt{n_\nu}\delta_{\nu',\nu-1}\int d\mathbf{x}\,\mathbf{A}^{(+)}_\nu(\mathbf{x})\cdot\mathbf{J}_{fi}(\mathbf{x})e^{-i\omega_\nu t} + \sqrt{n_\nu+1}\delta_{\nu',\nu+1}\int d\mathbf{x}\,\mathbf{A}^{(-)}_\nu(\mathbf{x})\cdot\mathbf{J}_{fi}(\mathbf{x})e^{i\omega_\nu t}\Big]e^{-i(\varepsilon_i-\varepsilon_f)t}, \tag{5.5}$$

where n_ν is the occupancy of the νth target mode. When carrying out the derivations of inelastic electron scattering processes, the first and second terms in Eq. (5.5) correspond to EEG and EEL events, respectively. The energy conserving delta function in Eq. (5.2), when written in the following equivalent forms

$$\delta(E_f-E_i) = \frac{1}{\hbar}\int d\omega \begin{cases}\delta(\omega-\varepsilon_{if})\delta(\omega-\omega_{\nu'\nu}) & \text{(EEL)}\\ \delta(\omega+\varepsilon_{if})\delta(\omega-\omega_{\nu\nu'}) & \text{(EEG)},\end{cases} \tag{5.6}$$

with $\varepsilon_{if}=\varepsilon_i-\varepsilon_f$ and $\omega_{\nu\nu'}=\omega_\nu-\omega_{\nu'}$, will aid in this connection to EEL and EEG.

In EEL events, the probing electron may transfer energy to and retrieve energy from any of the target modes which must be summed over to account for all such loss processes where the electron acts as both pump and probe. After summing over target states ν,ν', the EEL scattering rate becomes

$$w^{\text{loss}}_{fi} = \frac{2\pi}{\hbar c^2}\sum_\nu\int d\mathbf{x}d\mathbf{x}'\,\mathbf{J}^*_{fi}(\mathbf{x})\cdot\mathbf{A}^{(+)}_\nu(\mathbf{x})\mathbf{A}^{(-)}_\nu(\mathbf{x}')\cdot\mathbf{J}_{fi}(\mathbf{x}')\delta(E_f-E_i), \tag{5.7}$$

while, in the case of EEG, the stimulating laser field is taken to populate the specific target state ν leaving only a sum over final target states ν' to be performed, resulting in

$$w^{\text{gain}}_{fi} = \frac{2\pi}{\hbar c^2}\int d\mathbf{x}d\mathbf{x}'\,\mathbf{J}^*_{fi}(\mathbf{x})\cdot\mathbf{A}^{(-)}_\nu(\mathbf{x})\mathbf{A}^{(+)}_\nu(\mathbf{x}')\cdot\mathbf{J}_{fi}(\mathbf{x}')\delta(E_f-E_i). \tag{5.8}$$

Again note that the target vector potentials $\mathbf{A}^{(\pm)}_\nu(\mathbf{x})$ in the EEG rate in Eq. (5.8) are understood to originate in response to external laser stimulation and are not induced by the probing electron's transition current $\mathbf{J}_{fi}(\mathbf{x})$.

From Eqs. (5.6) and (5.7), together with the relationship $w_{fi}=\int d\omega\, w_{fi}(\omega)$, the frequency-resolved EEL rate $w^{\text{loss}}_{fi}(\omega)$ can be derived. By expressing the target vector potential in terms of mode functions, i.e., $\mathbf{A}^{(+)}_\nu(\mathbf{x})\mathbf{A}^{(-)}_\nu(\mathbf{x}')=(2\pi\hbar c^2/\omega_\nu)\mathbf{f}_\nu(\mathbf{x})\mathbf{f}^*_\nu(\mathbf{x}')$, Eq. (5.7) can be written in terms of the target's electromagnetic Green's tensor, $\overleftrightarrow{\mathbf{G}}(\mathbf{x},\mathbf{x}',\omega)=\sum_\nu\mathbf{f}_\nu(\mathbf{x})\mathbf{f}^*_\nu(\mathbf{x}')/(\omega^2-\omega^2_\nu+i0^+)$. More specifically, the EEL rate is formulated in terms of the imaginary part of the Green's dyadic, $\text{Im}\big\{\overleftrightarrow{\mathbf{G}}(\mathbf{x},\mathbf{x}',\omega)\big\}=-\sum_\nu(\pi/2\omega_\nu)\mathbf{f}_\nu(\mathbf{x})\mathbf{f}^*_\nu(\mathbf{x}')\delta(\omega-\omega_{\nu'\nu})$. As a result, the state- and frequency-resolved EEL transition rate then becomes

$$\begin{aligned} w^{\text{loss}}_{fi}(\omega) &= -\frac{8\pi}{\hbar}\int d\mathbf{x}d\mathbf{x}'\,\mathbf{J}^*_{fi}(\mathbf{x})\cdot\text{Im}\Big[\overleftrightarrow{\mathbf{G}}(\mathbf{x},\mathbf{x}',\omega)\Big]\cdot\mathbf{J}_{fi}(\mathbf{x}')\delta(\omega-\varepsilon_{if})\\ &= -\frac{8\pi}{\hbar}\int d\mathbf{x}d\mathbf{x}'\,\text{Im}\Big[\mathbf{J}^*_{fi}(\mathbf{x})\cdot\overleftrightarrow{\mathbf{G}}(\mathbf{x},\mathbf{x}',\omega)\cdot\mathbf{J}_{fi}(\mathbf{x}')\Big]\delta(\omega-\varepsilon_{if}),\end{aligned} \tag{5.9}$$

where the bottom line holds for reciprocal media characterized by $\overleftrightarrow{\mathbf{G}}(\mathbf{x},\mathbf{x}',\omega) = \overleftrightarrow{\mathbf{G}}^{T}(\mathbf{x}',\mathbf{x},\omega)$. Note that for general phase-shaped EEL processes described by Eq. (5.9), the transition current density can point arbitrarily in 3D space and is not restricted to lie along the TEM axis.

Alternatively, for the case of laser-stimulated EEG, Eqs. (5.6) and (5.8) determine the frequency-resolved EEG rate. The positive (negative) frequency portion of the target's laser-induced response field can be expressed in terms of its induced vector potential as $\mathbf{E}_{\nu}^{(\pm)}(\mathbf{x}) = (\pm i\omega_{\nu}/c)\,\mathbf{A}_{\nu}^{(\pm)}(\mathbf{x})$. When the stimulating laser excites a coherent state of the target $|\alpha_{\nu}\rangle$, the frequency resolved EEG rate

$$w_{fi}^{\text{gain}}(\omega) = 2\pi\left(\frac{|\alpha_{\nu}|}{\hbar\omega_{\nu}}\right)^{2}\left|\int d\mathbf{x}\,\mathbf{E}_{\nu}^{(+)}(\mathbf{x})\cdot\mathbf{J}_{fi}(\mathbf{x})\right|^{2}\delta(\omega+\varepsilon_{if})\delta(\omega-\omega_{\nu\nu'}) \tag{5.10}$$

is proportional to the volume integral of the 3D vector transition current density $\mathbf{J}_{fi}(\mathbf{x})$ projected onto the laser-induced electric field $\mathbf{E}_{\nu}^{(+)}(\mathbf{x})$ of the target. For simplicity, the applied monochromatic continuous-wave laser field is chosen to couple to the target's νth excited state only. In the low photon occupancy limit ($|\alpha_{\nu}| \approx 1$), this coherent state description yields

$$w_{fi}^{\text{gain}}(\omega) = 2\pi\left(\frac{1}{\hbar\omega_{\nu}}\right)^{2}\left|\int d\mathbf{x}\,\mathbf{E}_{\nu}^{(+)}(\mathbf{x})\cdot\mathbf{J}_{fi}(\mathbf{x})\right|^{2}\delta(\omega+\varepsilon_{if})\delta(\omega-\omega_{\nu\nu'}), \tag{5.11}$$

which has been stated previously [5]. As will be shown in Section 5.4.1, if the appropriate choices for the initial and final electron states are made, Eqs. (5.9) and (5.11) reduce to the conventional EEL and EEG probabilities found in the literature [5,68,90,91], but, as expressed here, are generalized to potentially describe polarized EEL and EEG measurements where the wave function of the probing electron is phase-structured in the plane orthogonal to its motion. Therefore, the approach producing Eqs. (5.9), (5.10), and (5.11) casts phase-shaped EEL and EEG interactions both within the same framework and on equal footing.

5.2 Transversely phase-structured free electron states

This section introduces various spinless free electron states relevant to the forthcoming discussion of phase-structured EEL and EEG measurements in TEM and STEM instruments. The states are: (i) energy eigenstates and thereby separable into spatial and temporal parts as $\psi(\mathbf{x},t) = \psi(\mathbf{x})e^{-i\varepsilon t}$ and (ii) separable within an orthogonal coordinate system $\mathbf{x} = (x_1, x_2, x_3)$ into transverse and longitudinal functions $\psi(\mathbf{x}) = \Psi(x_1,x_2)e^{ik_{\parallel}x_3}$. The electron wave functions are translationally invariant along the TEM axis, defined as $x_3 \equiv z$. Transversely delocalized states are investigated first, beginning with plane wave and vortex Bessel beam states originating as separable solutions in the Cartesian and cylindrical coordinate systems, respectively. Subsequently, transversely localized and nondiffracting wave functions, including Hermite-Gauss (HG) and twisted electron Laguerre-Gauss (LG) states, are presented.

Plane wave solutions are separable in Cartesian coordinates with well-defined linear momentum $\mathbf{p} = \hbar\mathbf{k}$.

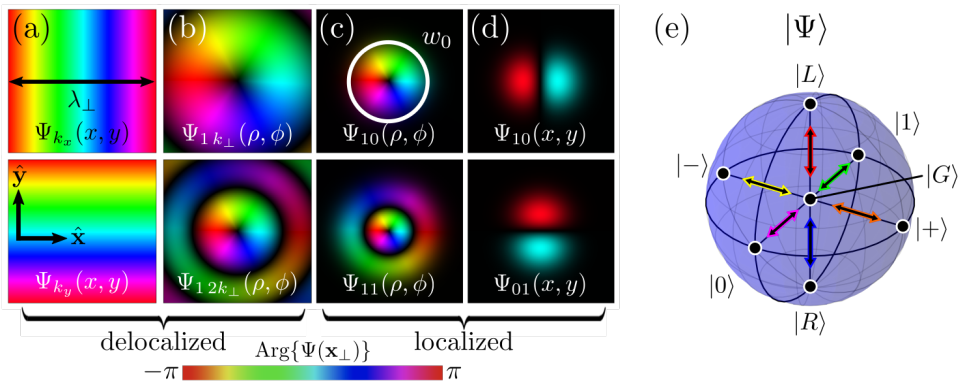

Figure 5.2: Transverse free electron states. Wave functions $\Psi(x,y)$ are visualized in the $z=0$ plane with position-dependent phase indicated by the color of the respective intensity profiles. Black represents low wave function density. (a) Plane wave states with $\mathbf{k}_\perp$ along $\hat{\mathbf{x}}$ (top) and $\hat{\mathbf{y}}$ (bottom). (b) Bessel beam states $\Psi_{\ell k_\perp}(\rho,\phi)$ with $\ell=1$, and radial wave number $k_\perp$ (top) and $2k_\perp$ (bottom). (c) LG states $\Psi_{\ell p}(\rho,\phi)$ with $\ell=1$, and $p=0$ (top) and $p=1$ (bottom). (d) HG states $\Psi_{nm}(x,y)$ with $n=1$ and $m=0$ (top), and $n=0$ and $m=1$ (bottom). (e) In the $\ell=\pm1$ OAM subspace, the first order LG states $|L/R\rangle$ can be used as basis states spanning the Bloch sphere with antipodal points $\{|0\rangle,|1\rangle\}$, $\{|+\rangle,|-\rangle\}$, and $\{|L\rangle,|R\rangle\}$; states with constant spatial phase are defined as $|G\rangle$ and placed at the sphere center. Colored arrows represent transitions between $|G\rangle$ and the states at the labeled antipodal points.

The spatial wave function describing a free electron in the 3D Cartesian space $\mathbf{x}=(x,y,z)$ is

$$\psi_{\mathbf{k}}(x,y,z)=\left(\frac{1}{\sqrt{L}}\right)^3 e^{i\mathbf{k}\cdot\mathbf{x}}, \tag{5.12}$$

where $\mathbf{k}=(\mathbf{k}_\perp,k_\parallel)$ is the wave vector and L is the box quantization length. Phase plots of two transverse plane wave states, $\Psi_{k_x}(x,y)$ and $\Psi_{k_y}(x,y)$, with orthogonal wave vectors $\mathbf{k}_\perp=k_x\hat{\mathbf{x}}$ and $\mathbf{k}_\perp=k_y\hat{\mathbf{y}}$ and corresponding transverse wavelengths $\lambda_{\perp x}=2\pi/k_x$ and $\lambda_{\perp y}=2\pi/k_y$, and are displayed in the upper and lower panels of Fig. 5.2(a) for $\lambda_{\perp x}=\lambda_{\perp y}=\lambda_\perp$, respectively. Electrons can also be prepared in coherent superposition states, with one example of such a state being $\psi^{\chi}_{k_xk_y}(x,y,z)=L^{-3/2}\left[e^{ik_xx}+e^{ik_yy}e^{i\chi}\right]e^{ik_\parallel z}/\sqrt{2}$, where the relative phase χ between the two orthogonal electron wave vector components k_x and k_y can take values $0\leq\chi\leq2\pi$ [54,77,118].

When expressed in the cylindrical coordinate system defined by $\mathbf{x}=(\rho,\phi,z)$, the separable solutions are nondiffracting Bessel waves of the form [126,191–193],

$$\psi_{\ell k_\perp}(\rho,\phi,z)\propto J_{|\ell|}(k_\perp\rho)e^{i\ell\phi}e^{ik_\parallel z}. \tag{5.13}$$

Here, $J_{|\ell|}(k_\perp\rho)$ are Bessel functions of the first kind, ℓ is the azimuthal quantum number of the cylindrically symmetric state, while $k_\perp$ is the radial wave vector component and $k_\parallel$ is the longitudinal wave vector component, respectively [26]. Such states are eigenstates of the z-component of the OAM operator $\hat{L}_z=-i\hbar\partial/\partial\phi$ with eigenvalue $\ell\hbar$. Specific examples of Bessel states are shown in Fig. 5.2(b) for two different values of $k_\perp$.

Transversely localized free electron states can be constructed within the paraxial approximation to the Schrödinger equation, where the electron momentum along the TEM axis is much greater than its transverse momentum, i.e., $k_\perp \ll |\mathbf{k}|$. Since they are eigenstates of the $\hat{L}_z$ operator, LG states carry a quantized azimuthal component ℓ. In the nondiffracting, i.e., collimated, limit defined by infinite Rayleigh range, the LG wave functions have the form of quantized Landau states [26, 191] given by

$$\psi_{\ell p}(\rho,\phi,z) = \frac{\left(\sqrt{2}\rho/w_0\right)^{|\ell|}}{w_0\sqrt{L}}\sqrt{\frac{2p!}{\pi(|\ell|+p)!}}\mathrm{L}_p^{|\ell|}\left(\frac{2\rho^2}{w_0^2}\right)e^{-\frac{\rho^2}{w_0^2}}e^{i\ell\phi}e^{ik_\parallel z}, \tag{5.14}$$

where $\mathrm{L}_p^{|\ell|}$ are the Laguerre polynomials, with ℓ and p being the azimuthal and radial quantum numbers, respectively, and w_0 is the z-independent beam waist. Fig. 5.2(c) displays two different LG modes with finite beam waists w_0.

Similarly, the HG family of transversely localized wave functions are solutions to the paraxial wave equation in the Cartesian coordinate system. Since the nondiffracting LG and HG states each comprise a complete orthonormal basis, any LG (HG) state can be synthesized from the appropriate coherent superposition of HG (LG) states [194]. Unlike the LG transverse states, the HG states lack a well-defined azimuthal phase, and owing to the fact that they are not eigenstates $\hat{L}_z$, do not carry a single OAM unit of ℓ. In the nondiffracting limit, the HG states take the form

$$\psi_{nm}(x,y,z) = \frac{2^{-\frac{n+m}{2}}}{w_0\sqrt{L}}\sqrt{\frac{2}{\pi n!m!}}H_n\left(\frac{x\sqrt{2}}{w_0}\right)H_m\left(\frac{y\sqrt{2}}{w_0}\right)e^{-\frac{x^2+y^2}{w_0^2}}e^{ik_\parallel z}, \tag{5.15}$$

and are labeled by the indices n and m, corresponding to the order of the x- and y-dependent Hermite polynomials, H_n and H_m, respectively. Fig. 5.2(d) displays the first-order x- and y-oriented HG modes with beam waists w_0, in contrast to the corresponding delocalized $\Psi_{k_x}(x,y)$ and $\Psi_{k_y}(x,y)$ plane waves displayed in Fig. 5.2(a).

Mirroring applications of optical OAM states, free electrons with quantized transverse degrees of freedom have recently been recognized as potential carriers of quantum information, specifically as free electron OAM qubits. Realization of such OAM qubits has been made possible via holographic masks and spiral phase plates [44–46, 179] or through tailored light sources [133, 180]. Stemming from the separability of the electron wave function following condition (ii), the orthogonal transverse degrees of freedom can be used as orthonormal basis states $|0\rangle$ and $|1\rangle$ on the Bloch sphere (Fig. 5.2(e)). Known as the horizontal and vertical basis states, respectively, linear combinations of $|0\rangle$ and $|1\rangle$ assemble the remaining antipodal points $|L/R\rangle = (1/\sqrt{2})\big[|0\rangle \pm i|1\rangle\big]$ and $|\pm\rangle = (1/\sqrt{2})\big[|0\rangle \pm |1\rangle\big]$. One example are the first order LG states $\Psi_{\pm 10}(\rho,\phi) = \langle x_1x_2|L/R\rangle$ which span the truncated $\ell = \pm 1$, two dimensional Hilbert space [184, 185, 194], and lie on the north and south poles of the Bloch sphere. Owing to the fact that $\Psi_{\pm 10}(\rho,\phi)$ can be expressed as linear combinations of the first order HG states [41], $\Psi_{10}(x,y) = \langle x_1x_2|0\rangle$ and $\Psi_{01}(x,y) = \langle x_1x_2|1\rangle$ are the wave functions associated with the vertical and horizontal basis states, respectively. At the center of the Bloch

sphere lies the Gaussian mode $\Psi_{00}(x,y) = \Psi_{00}(\rho,\phi) = \langle x_1 x_2|G\rangle = \sqrt{2/\pi w_0^2}e^{-(x^2+y^2)/w_0^2} = \sqrt{2/\pi w_0^2}e^{-\rho^2/w_0^2}$. More generally, higher order electron vortex states with topological charge of $\pm\ell$ can be used to construct Bloch spheres for ℓ values other than unity [158]. Following the work of Ref. [4], under the appropriate limits, certain superpositions of electron plane wave states can likewise be mapped onto points on the Bloch sphere (Fig. 5.2(e)). In this scenario, the horizontal and vertical plane wave wave functions $\Psi_{k_x}(x,y) = \langle x_1 x_2|0\rangle$ and $\Psi_{k_y}(x,y) = \langle x_1 x_2|1\rangle$ can be used to construct the north and south antipodal point wave functions $\Psi^{\pm\pi/2}_{k_x k_y}(x,y)$. Specifically, $\Psi^{\pm\pi/2}_{k_x k_y}(x,y) = \langle x_1 x_2|L/R\rangle = (1/\sqrt{2})\big[\Psi_{k_x}(x,y) + \Psi_{k_y}(x,y)e^{i\chi}\big]$ with $\chi = \pm\pi/2$. At the center of the Bloch sphere is located the electron plane wave $\Psi_{k_\parallel}(x,y) = \langle x_1 x_2|G\rangle = 1/L$ with spatially uniform transverse phase and purely longitudinal wave vector $\mathbf{k} = k_\parallel \hat{\mathbf{z}}$. As will be shown in the following section, transitions between OAM or linear momentum electron states residing on the Bloch sphere produce transition current densities with unique vector and phase profiles.

5.3 Transition current density

Here the transition current density $\mathbf{J}_{fi}(\mathbf{x})$ defined in Eq. (5.4) is examined for selected transitions between electron states introduced in the previous section. This section begins with a summary of general properties of $\mathbf{J}_{fi}(\mathbf{x})$ that arise from the restrictions imposed on the forms of the wave functions, then highlights several general and specific forms of the transition current density for transitions involving delocalized and localized electron states. A note regarding the arguments of the transition current density: recall that the origin of time dependence in $\mathbf{J}_{fi}(\mathbf{x},t) = \mathbf{J}_{fi}(\mathbf{x})e^{i\varepsilon_{fi}t}$ as seen in Eq. (5.3) is a consequence of condition (i) imposed upon the electron wave functions introduced in the first paragraph of Sec. 5.2. Therefore, as a matter of convenience and unless stated otherwise, we work with the time-independent version of the transition current density. In addition, when discussing the transition current density for Bessel, LG, and HG free electron states, the subscripts of $\mathbf{J}_{fi}(\mathbf{x})$ refer explicitly to the final and initial transverse electron states. Panels (a) and (b) of Fig. (5.3) present LG and Bessel beam transitions, respectively, panel (c) involves transitions between plane wave states, panels (d) and (e) showcase the transition current density using focused first order HG states.

Stemming from conditions (i) and (ii) required of the electron wave functions as stipulated in Sec. 5.2, the transition current density given by Eq. (5.4) can be re-expressed as the sum of longitudinal ($\parallel$) and transverse ($\perp$) contributions, defined relative to the TEM axis, according to

$$\begin{aligned}\mathbf{J}_{fi}(\mathbf{x}) &= \mathbf{J}_{fi}(\mathbf{x}_\perp)e^{iq_\parallel z} \\ &= \big[\mathbf{J}^{\perp}_{fi}(\mathbf{x}_\perp) + J^{\parallel}_{fi}(\mathbf{x}_\perp)\hat{\mathbf{z}}\big]e^{iq_\parallel z}.\end{aligned} \tag{5.16}$$

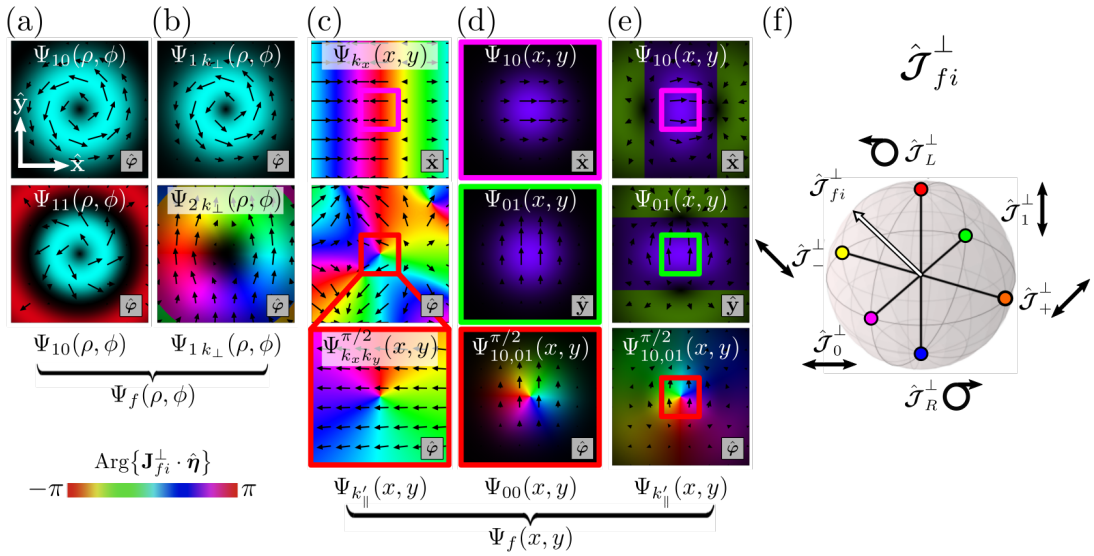

Figure 5.3: Transition current density vector fields $\mathbf{J}_{fi}(\mathbf{x})$ in the $z=0$ plane. The arrows within each panel show the direction and strength of the transverse component $\mathbf{J}^\perp_{fi}(\mathbf{x})$, while the underlying color map indicates the phase $(\mathbf{J}^\perp_{fi}(\mathbf{x})\cdot\hat{\boldsymbol{\eta}})$ and intensity $(|\mathbf{J}^\perp_{fi}(\mathbf{x})|)$. $\hat{\boldsymbol{\eta}}$ is displayed in the bottom right hand corner of each panel. The initial transverse wave functions for the transition current density vector fields are labeled in the top-center of each panel, while the final state is shown at the bottom of each column. (a) Transition current densities involving LG $\Psi_{\ell p}(\rho,\phi)$ initial and final states. The top panel shows the case of $\Psi_{10}(\rho,\phi)\to\Psi_{10}(\rho,\phi)$ with no transverse transition; the $\Psi_{11}(\rho,\phi)\to\Psi_{10}(\rho,\phi)$ transition in the lower panel involves a transition in radial, but not OAM, quantum numbers. (b) Transitions between Bessel states $\Psi_{\ell k_\perp}(\rho,\phi)$. The top panel shows the transition current density for $\Psi_{1k_\perp}(\rho,\phi)\to\Psi_{1k_\perp}(\rho,\phi)$ with no transverse state transition, while the lower panel considers the transition current density for $\Psi_{1k_\perp}(\rho,\phi)\to\Psi_{2k_\perp}(\rho,\phi)$ with an OAM change of $\Delta\ell=1$. (c) Incoming electron plane wave states transitioning to the pin hole state $\Psi_{k'_\parallel}(x,y)$. The initial state is characterized by $\mathbf{q}_\perp=k_x\hat{\mathbf{x}}$ in the top panel, while the lower panels involve the incident superposition plane wave state $\Psi^{\pi/2}_{k_xk_y}(x,y)$. The lower panel is a magnified view of the middle panel in the vicinity of the origin. (d) Transition current densities for first-order HG and LG wave functions transitioning to the Gaussian state. (e) Transition current densities for transitions from selected HG and LG states to the pin hole state. (f) $\hat{\boldsymbol{\mathcal{J}}}^\perp_{fi}$ for transitions between free electron OAM or linear momentum states which create transition current vector fields resembling the polarization vectors of light on the Poincaré sphere. The antipodal points $\{\hat{\boldsymbol{\mathcal{J}}}^\perp_0,\hat{\boldsymbol{\mathcal{J}}}^\perp_1\}$, $\{\hat{\boldsymbol{\mathcal{J}}}^\perp_+,\hat{\boldsymbol{\mathcal{J}}}^\perp_-\}$, and $\{\hat{\boldsymbol{\mathcal{J}}}^\perp_L,\hat{\boldsymbol{\mathcal{J}}}^\perp_R\}$ are color coded to match the box colors outlining the panels in columns (c) through (e), as well as the electron state transition arrows in Fig. 5.2(e).

Explicitly, these components are

$$\begin{aligned}\mathbf{J}_{fi}^{\perp}(\mathbf{x}_{\perp}) &= \frac{i\hbar e}{2mL}\left[\Psi_f^*(\mathbf{x}_{\perp})\nabla_{\perp}\Psi_i(\mathbf{x}_{\perp}) - \Psi_i(\mathbf{x}_{\perp})\nabla_{\perp}\Psi_f^*(\mathbf{x}_{\perp})\right] \\ J_{fi}^{\parallel}(\mathbf{x}_{\perp}) &= -\frac{\hbar e}{2mL}Q_{\parallel}\Psi_f^*(\mathbf{x}_{\perp})\Psi_i(\mathbf{x}_{\perp}),\end{aligned} \tag{5.17}$$

where $Q_{\parallel} = k_{\parallel} + k'_{\parallel}$. It can be seen from the perpendicular component of Eq. (5.17), that interchange of the initial and final transverse states is equivalent to conjugation of the reciprocal scattering process, i.e., $\mathbf{J}_{if}(\mathbf{x}) = \mathbf{J}_{fi}^*(\mathbf{x})$.

5.3.1 Plane wave states

First we consider transitions between individual incoming $\psi_{\mathbf{k}_i}(x,y,z)$ and outgoing $\psi_{\mathbf{k}_f}(x,y,z)$ plane wave states of the probe, defined in Eq. (5.12), such that $\hbar\mathbf{q} = \hbar(\mathbf{k}_i - \mathbf{k}_f)$ is the momentum recoil associated with the transition. The transition current density associated with this case is

$$\mathbf{J}_{\mathbf{k}_f\mathbf{k}_i}(x,y,z) = -\frac{e\hbar}{2mL^3}(2\mathbf{k}_i - \mathbf{q})e^{i\mathbf{q}\cdot\mathbf{x}}. \tag{5.18}$$

Inspection of Eq. (5.18) reveals that the transverse component of the transition current density is directly proportional to the transverse recoil momentum, i.e., $\mathbf{J}_{\mathbf{k}_f\mathbf{k}_i}^{\perp}(x,y,z) \propto \mathbf{q}_{\perp}$. The phase and vector structure of the transition current density for an initial plane wave state with transverse wave vector $\mathbf{k}_{\perp} = k_x\hat{\mathbf{x}}$ transitioning to the outgoing plane wave state $\psi_{k'_{\parallel}}(x,y,z) = L^{-3/2}e^{ik'_{\parallel}z}$ is shown in the first panel of Fig. 5.3(c). This final state is referred to as the pin hole state as it is selected by placement of a pin hole on the TEM axis in the Fourier plane. In Fig. 5.3(c), it is evident that the periodicity of the plane wave states apparent in Fig. 5.2(a) is inherited by the transition current density.

When prepared in a superposition plane wave state $\psi_{k_xk_y}^{\chi}(x,y,z)$ and post-selected in the diffraction plane for the pin hole state, the resulting transition current density of the probe is

$$\mathbf{J}_{k'_{\parallel},k_xk_y}^{\chi}(x,y,z) = -\frac{e\hbar}{2\sqrt{2}mL^3}\left[k_xe^{ik_xx}\hat{\mathbf{x}} + k_ye^{i\chi}e^{ik_yy}\hat{\mathbf{y}} + Q_{\parallel}\left(e^{ik_xx} + e^{i\chi}e^{ik_yy}\right)\hat{\mathbf{z}}\right]e^{iq_{\parallel}z}. \tag{5.19}$$

The phase and vector information of this transition current density are displayed in the final two panels of Fig. 5.3(c) for $\chi = \pi/2$ at two different magnification levels. Owing to the spatial dependence of the wave functions, the $\hat{\mathbf{x}},\hat{\mathbf{y}}$-components of Eq. (5.19) are functionally dependent upon x and y. It was shown in Ref. [4] when working in the dipole scattering regime, whereby $\mathbf{q}_{\perp}$ is such that $|\mathbf{q}_{\perp}|d \ll 1$, with d the transverse length scale of the target, $\mathbf{J}_{fi}^{\perp}(\mathbf{x}_{\perp})$ becomes approximately independent of position in the vicinity of the target. Under these circumstances when the perpendicular components of the transition current density become independent of position, $\mathbf{J}_{fi}^{\perp}(\mathbf{x}_{\perp}) \to \boldsymbol{\mathcal{J}}_{fi}^{\perp}$. After normalization, $\hat{\boldsymbol{\mathcal{J}}}_{fi}^{\perp} = \boldsymbol{\mathcal{J}}_{fi}^{\perp}/|\boldsymbol{\mathcal{J}}_{fi}^{\perp}|$ can thus be mapped onto the Poincaré sphere (Fig. 5.3(f)) [4]. In this limit, for $\chi = \pi/2$, the transverse component of Eq. (5.19) becomes circularly polarized such that it mimics the polarization of a left-handed circularly

polarized photon, evident in the final panel of Fig. 5.3(c) boxed in red. All together, when $|\mathbf{q}_\perp|d \ll 1$, the transition current densities given by Eqs. (5.18) and (5.19) can be tailored through appropriate pre- and post-selection to resemble any polarization state of light on the Poincaré sphere as shown in Fig. 5.3(f).

5.3.2 Bessel and Laguerre-Gauss states

By virtue of the ability to prepare free electrons in defocused vortex (Bessel) or focused vortex (LG) states, the corresponding transition current density can exhibit both radial and azimuthal transverse vector components. The transition current density associated with transitions between Bessel beam states $\psi_{\ell k_\perp}(\rho,\phi,z)$ and $\psi_{\ell' k'_\perp}(\rho,\phi,z)$ is [4]

$$\begin{aligned}\mathbf{J}_{\ell' k'_\perp,\ell k_\perp}(\rho,\phi,z) = \frac{i\hbar e}{2m}\Psi_{\ell k_\perp}(\rho,\phi)\Psi^*_{\ell' k'_\perp}(\rho,\phi)\Bigg[\Bigg\{\frac{k_\perp}{2}J_{|\ell|}(k_\perp\rho)^{-1}\left[J_{|\ell|-1}(k_\perp\rho)-J_{|\ell|+1}(k_\perp\rho)\right]\\ -\frac{k'_\perp}{2}J^*_{|\ell'|}(k'_\perp\rho)^{-1}\left[J^*_{|\ell'|-1}(k'_\perp\rho)-J^*_{|\ell'|+1}(k'_\perp\rho)\right]\Bigg\}\hat{\boldsymbol{\rho}}+\frac{i}{\rho}(\ell+\ell')\hat{\boldsymbol{\phi}}+iQ_\parallel\hat{\mathbf{z}}\Bigg]e^{iq_\parallel z},\end{aligned} \tag{5.20}$$

for arbitrary $\ell, k_\perp$ and $\ell', k'_\perp$. The transition current density for $\ell' = \ell = 1$ and $k'_\perp = k_\perp$, with $\Delta\ell = 0$ is displayed in the first panel of Fig. 5.3(b), showcasing the expected azimuthal character inherent to twisted electron beams. Bessel beam states can also lead to unique phase and vector profiles as seen in the lower panel of Fig. 5.3(b), wherein $\Delta\ell = 1$ resulting in a transition current density with a phase-structure similar to that of circularly polarized light, as well as to the wave functions shown in Fig. 5.2(b).

Additionally, the focused LG states in Eq. (5.14) can also produce transition current densities with well-defined units of OAM transferred. The transition current density for an initial LG electron state $\psi_{\ell p}(\rho,\phi,z)$ transitioning to a final state $\psi_{\ell' p'}(\rho,\phi,z)$ is given by

$$\begin{aligned}\mathbf{J}_{\ell' p',\ell p}(\rho,\phi,z) = \frac{i\hbar e}{2m}\Psi_{\ell p}(\rho,\phi)\Psi^*_{\ell' p'}(\rho,\phi)\Bigg[\frac{1}{\rho}\Bigg\{\left(|\ell|-|\ell'|\right)\\ -\frac{4\rho^2}{w_0^2}\left(\mathrm{L}_p^{|\ell|}\left(\frac{2\rho^2}{w_0^2}\right)\mathrm{L}_{p'}^{|\ell'|*}\left(\frac{2\rho^2}{w_0^2}\right)\right)^{-1}\left(\mathrm{L}_{p'}^{|\ell'|*}\left(\frac{2\rho^2}{w_0^2}\right)\mathrm{L}_p^{|\ell|+1}\left(\frac{2\rho^2}{w_0^2}\right)-\mathrm{L}_p^{|\ell|}\left(\frac{2\rho^2}{w_0^2}\right)\mathrm{L}_{p'}^{|\ell'|+1,*}\left(\frac{2\rho^2}{w_0^2}\right)\right)\Bigg\}\hat{\boldsymbol{\rho}}\\ +\frac{i}{\rho}(\ell+\ell')\hat{\boldsymbol{\phi}}+iQ_\parallel\hat{\mathbf{z}}\Bigg]e^{iq_\parallel z}\end{aligned} \tag{5.21}$$

valid for arbitrary ℓ, p and ℓ', p'. Stemming from the commonalities in the underlying wave functions, it is unsurprising that Eq. (5.20) and Eq. (5.21) look similar. This resemblance is most obvious when considering events wherein no transverse transition occurs, as seen when comparing the first panels of Fig. 5.3(a) and Fig. 5.3(b), for transitions between LG and Bessel states, respectively. Here, shown in the top panel of Fig. 5.3(a), is Eq. (5.21) for $p' = p = 0$ and $\ell' = \ell = 1$, which highlights the azimuthal vector component of the LG transition current density and is similar to the corresponding Bessel beam case displayed in the top panel of Fig. 5.3(b) for $1k_\perp$ transitioning to $1k_\perp$. The bottom panel of Fig. 5.3(a) shows the transition current density for $\Delta p = 1$. For inelastic scattering events where the electron does not transfer OAM to the target,

$\ell' = \ell$ and $p' = p$, and Eq. (5.21) reduces to

$$\mathbf{J}_{\ell'=\ell,p'=p}(\rho,\phi,z) = -\frac{\hbar e}{2mL}\left|\Psi_{\ell p}(\rho,\phi)\right|^2\left[\frac{2\ell}{\rho}\hat{\boldsymbol{\phi}} + Q_\parallel\hat{\mathbf{z}}\right]e^{iq_\parallel z}, \tag{5.22}$$

which is the focused vortex beam form of the transition current density of a free electron moving along $\hat{\mathbf{v}} = \hat{\mathbf{z}}$ [26, 56]. The azimuthal component of Eq. (5.22) is responsible for the spiraling behavior of the electron current typical for vortex beams, and upon spatial integration over (ρ,ϕ) yields an electron current with an axial inertial OAM equal to $\ell\hbar$ [26].

5.3.3 Hermite-Gauss states

Transitions between transverse HG states that are naturally expressed in the Cartesian basis provide transition current densities with any desired $\hat{\mathbf{x}},\hat{\mathbf{y}}$-vectorial structure. Following the approach of Ref. [4], a general form for $\mathbf{J}_{n'm',nm}(x,y,z)$ involving arbitrary HG states can be derived from Eq. (5.4). The transition current density for $\psi_{nm}(x,y,z)$ transitioning to $\psi_{n'm'}(x,y,z)$ is

$$\begin{aligned}\mathbf{J}_{n'm',nm}(x,y,z) = \frac{i\hbar e}{2mw_0L}\Big[&\big\{\sqrt{n}\Psi_{n-1,m}(x,y)\Psi^*_{n'm'}(x,y) - \sqrt{n+1}\Psi_{n+1,m}(x,y)\Psi^*_{n'm'}(x,y)\\ &- \sqrt{n'}\Psi_{nm}(x,y)\Psi^*_{n'-1,m'}(x,y) + \sqrt{n'+1}\Psi_{nm}(x,y)\Psi^*_{n'+1,m'}(x,y)\big\}\hat{\mathbf{x}}\\ &+ \big\{\sqrt{m}\Psi_{n,m-1}(x,y)\Psi^*_{n'm'}(x,y) - \sqrt{m+1}\Psi_{n,m+1}(x,y)\Psi^*_{n'm'}(x,y)\\ &- \sqrt{m'}\Psi_{nm}(x,y)\Psi^*_{n',m'-1}(x,y) + \sqrt{m'+1}\Psi_{nm}(x,y)\Psi^*_{n',m'+1}(x,y)\big\}\hat{\mathbf{y}}\\ &+ iw_0Q_\parallel\Psi_{nm}(x,y)\Psi^*_{n'm'}(x,y)\hat{\mathbf{z}}\Big]e^{iq_\parallel z},\end{aligned} \tag{5.23}$$

for arbitrary n,m,n',m'. As seen in the form of the perpendicular component of Eq. (5.23), careful choice regarding the pre- and post-selection of the initial/final HG transverse electron states can be intuited to yield a transition current density with non-trivial $\hat{\mathbf{x}},\hat{\mathbf{y}}$-vectorial behavior in the plane orthogonal to the direction of propagation. Working in the $\ell = \pm 1$ OAM Hilbert space, $\mathbf{J}_{n'm',nm}(x,y,z)$ is displayed in the columns of Fig. 5.3(d) for first order electron wave functions $\psi_{10}(x,y,z)$ and $\psi_{01}(x,y,z)$, and their linear combination $\psi^{\chi=\pi/2}_{10,01}(x,y,z) = (1/\sqrt{2L})\left[\psi_{10}(x,y,z) + \psi_{01}(x,y,z)e^{i\pi/2}\right]$, respectively, all transitioning to the final Gaussian wave function $\psi_{00}(x,y,z) = (1/\sqrt{L})\Psi_{00}(x,y)e^{ik'_\parallel z}$. In the zero width limit whereby $w_0 \to 0$, for the first order transitions discussed above, the transverse components of the transition current density become spatially independent and $\mathbf{J}^\perp_{fi}(\mathbf{x}) \to \boldsymbol{\mathcal{J}}^\perp_{fi}$. Under these constraints, the transition current density unit vector $\boldsymbol{\mathcal{J}}^\perp_{fi}$ can thus imitate the polarization vector $\hat{\boldsymbol{\epsilon}}$ of free space light, as illustrated on the electron analog of the Poincaré sphere presented in Fig. 5.3(f). When no transverse transition of the probe occurs, i.e., $n' = n$ and $m' = m$ in Eq. (5.23), the transition current density reduces to

$$\mathbf{J}_{n'=n,m'=m}(x,y,z) = -\frac{e\hbar}{2mL}Q_\parallel\left|\Psi_{nm}(x,y)\right|^2 e^{iq_\parallel z}\hat{\mathbf{z}}, \tag{5.24}$$

which is oriented parallel to the TEM axis regardless of the values for n and m. In the zero width limit, Eq. (5.24) reduces to the classical current of a point electron source [68] when $n = m = 0$. Overall, the purely longitudinal behavior of Eq. (5.24) differs from the vortex electron beam case in Eq. (5.22) wherein the current density has a $\hat{\boldsymbol{\phi}}$-component perpendicular to the electron's direction of motion.

Alternatively, when the nm HG state transitions to the forward directed pin hole state rather than a transversely focused Gaussian state, the transition current density becomes

$$\begin{aligned}\mathbf{J}_{k'_{\parallel},nm}(x,y,z) = \frac{i\hbar e}{2mw_0L^2}\Big[&\big\{\sqrt{n}\Psi_{n-1,m}(x,y) - \sqrt{n+1}\Psi_{n+1,m}(x,y)\big\}\hat{\mathbf{x}}\\ &+\big\{\sqrt{m}\Psi_{n,m-1}(x,y) - \sqrt{m+1}\Psi_{n,m+1}(x,y)\big\}\hat{\mathbf{y}}\\ &+ iw_0Q_{\parallel}\Psi_{n,m}(x,y)\hat{\mathbf{z}}\Big]e^{iq_{\parallel}z}.\end{aligned} \tag{5.25}$$

Eq. (5.25) is displayed in Fig. 5.3(e) for the same initial HG states as those used in Fig. 5.3(d), transitioning instead to the pin hole state $\psi_{k'_{\parallel}}(x,y,z)$. For the focused superposition state $\psi^{\chi}_{10,01}(x,y,z) = (1/\sqrt{2L})\big[\psi_{10}(x,y,z) + \psi_{01}(x,y,z)e^{i\chi}\big]$ transitioning to the pin hole state $\psi_{k'_{\parallel}}(x,y,z)$, the transition current density explicitly has the form

$$\begin{aligned}\mathbf{J}^{\chi}_{k'_{\parallel},10,01}(x,y,z) = \frac{i\hbar e}{2\sqrt{2}mw_0L^2}\Big[&\big\{\Psi_{00}(x,y) - \sqrt{2}\Psi_{20}(x,y) - \Psi_{11}(x,y)e^{i\chi}\big\}\hat{\mathbf{x}}\\ &+\big\{\big(\Psi_{00}(x,y) - \sqrt{2}\Psi_{02}(x,y)\big)e^{i\chi} - \Psi_{11}(x,y)\big\}\hat{\mathbf{y}}\\ &+ iw_0Q_{\parallel}\big\{\Psi_{10}(x,y) + \Psi_{01}(x,y)e^{i\chi}\big\}\hat{\mathbf{z}}\Big]e^{iq_{\parallel}z}.\end{aligned} \tag{5.26}$$

The difference between Eqs. (5.19) and (5.26) originates from the choice of the initial electron wave function being either a superposition of linear momentum or OAM states, respectively. Imposing the same conditions placed upon the wave functions in Eq. (5.23) to obtain a transition current density whose transverse vectorial components are spatially independent, Eqs. (5.25) and (5.26) can be used to construct transition current densities on the surface of the Poincaré sphere as presented in Fig. 5.3(f). Therefore, transitions between specific states on the Bloch sphere (Fig. 5.2(e)) produce transition current densities which mimic the polarization structure of free space light and can thus be mapped onto the Poincaré sphere (Fig. 5.3(f)).

5.4 State- and energy-resolved Observables

Building from Secs. 5.1, 5.2, and 5.3, in this section the EEL, EEG, and DDCS observables between phase-shaped states of the electron probe are derived. Measurements of EEL and EEG processes are discussed first, including the narrow beam width limit common in the low-loss electron scattering regime, before moving on to presentation of the DDCS. A comparison of the EEL and EEG scattering processes, and their relation to the properties of the transition current density under interchange of initial/final electron states is briefly presented. We illustrate that the transversely phase-shaped EEL, EEG, and DDCS observables, reduce to

the familiar forms found in the literature under the appropriate limits.

5.4.1 Electron energy loss and gain probabilities in the narrow beam width limit

In considering low-loss EEL and EEG scattering events in the narrow beam width limit appropriate to the STEM it is customary to work within the nonrecoil approximation, where the change in the energy of the electron is dictated entirely by its momentum change along the axis of propagation [68]. In this limit, the forward recoil momentum $\hbar q_\parallel \hat{\mathbf{z}}$ is small compared to the electron's initial momentum $\hbar \mathbf{k}_i$ so that its change in energy can be approximated by $\hbar\varepsilon_{if} = \sqrt{(mc^2)^2 + (\hbar c \mathbf{k}_i)^2} - \sqrt{(mc^2)^2 + (\hbar c(\mathbf{k}_i - \mathbf{q}))^2} \approx \hbar \mathbf{v}_i \cdot \mathbf{q}$, where $\hbar \mathbf{k}_i / m = \gamma_i \mathbf{v}_i$ and $\hbar \mathbf{k}_i = \mathbf{p}_i$ for relativistic matter waves. Upon insertion of $\varepsilon_{if} = \mathbf{v}_i \cdot \mathbf{q}$ into the trailing delta function in Eq. (5.9), the state- and frequency-resolved EEL rate becomes

$$w_{fi}^{\text{loss}}(\omega) = -\frac{8\pi}{\hbar v_i} \int d\mathbf{x} d\mathbf{x}' \, \text{Im}\Big[\mathbf{J}_{fi}^*(\mathbf{x}) \cdot \overleftrightarrow{\mathbf{G}}(\mathbf{x}, \mathbf{x}', \omega) \cdot \mathbf{J}_{fi}(\mathbf{x}')\Big] \delta(q_\parallel - \omega / v_i), \tag{5.27}$$

where $\overleftrightarrow{\mathbf{G}}(\mathbf{x}, \mathbf{x}', \omega)$ is the target's electromagnetic Green's tensor introduced in Sec. 5.1. The state- and energy-resolved EEL probability $P_{fi}^{\text{loss}}(\omega) = (L/v_i) w_{fi}^{\text{loss}}(\omega)$ is obtained by integrating Eq. (5.27) over the time it takes the probe electron to traverse the path length L as it interacts with the target specimen. From $P_{fi}^{\text{loss}}(\omega)$, the state- and energy-resolved EEL probability is determined by summing over all possible final electron states with $\sum_{k_\parallel^f} \to +(L/2\pi) \int_{-\infty}^{\infty} dq_\parallel$ and dividing by $\hbar$, resulting in the EEL probability per unit energy

$$\Gamma_{fi}^{\text{loss}}(\omega) = -\frac{4}{\hbar^2} \int d\mathbf{x} d\mathbf{x}' \, \text{Im}\Big[\left(\frac{L}{v_i}\right) \mathbf{J}_{fi}^*(\mathbf{x}; q_\parallel = \frac{\omega}{v_i}) \cdot \overleftrightarrow{\mathbf{G}}(\mathbf{x}, \mathbf{x}', \omega) \cdot \left(\frac{L}{v_i}\right) \mathbf{J}_{fi}(\mathbf{x}'; q_\parallel = \frac{\omega}{v_i})\Big]. \tag{5.28}$$

Here $\mathbf{J}_{fi}(\mathbf{x}; q_\parallel = \omega/v_i) = \mathbf{J}_{fi}(\mathbf{x})|_{q_\parallel = \omega/v_i} = \mathbf{J}_{fi}(\mathbf{x}_\perp) e^{i q_\parallel z}|_{q_\parallel = \omega/v_i} = \mathbf{J}_{fi}(\mathbf{x}_\perp) e^{i(\omega/v_i) z}$ makes explicit the locking of the longitudinal recoil wave number $q_\parallel$ to ω/v_i imposed by the nonrecoil approximation in Eqs. (5.27) and (5.28). Due to the frequent appearance of the L/v_i factor here and in the following equations, we define a new transition current as $\mathbf{J}_{fi}(\mathbf{x}, \omega = q_\parallel v_i) \equiv (L/v_i) \mathbf{J}_{fi}(\mathbf{x}; q_\parallel = \omega/v_i)$ with dimensions of charge flux per unit frequency. For clarity, we also abandon the general notation $\mathbf{x} = (\mathbf{x}_\perp, z)$ in favor of $\mathbf{x} = (\mathbf{R}, z)$ as is common in the low-loss STEM EEL and EEG literature.

Using the current $\mathbf{J}_{fi}(\mathbf{x}, \omega = q_\parallel v_i)$, the EEL probability can also be cast in terms of the target's transition electric field $\mathbf{E}_{fi}(\mathbf{x}, \omega = q_\parallel v_i) = -4\pi i \omega \int d\mathbf{x}' \, \overleftrightarrow{\mathbf{G}}(\mathbf{x}, \mathbf{x}', \omega) \cdot \mathbf{J}_{fi}(\mathbf{x}', \omega = q_\parallel v_i)$ resolved in frequency. $\mathbf{E}_{fi}$ represents the electric field produced by the target in response to stimulation by the probing electron. Expressed in terms of this field, the EEL probability per unit energy becomes

$$\Gamma_{fi}^{\text{loss}}(\omega) = -\frac{1}{\pi \hbar^2 \omega} \text{Re}\left[\int d\mathbf{x} \, \mathbf{J}_{fi}^*(\mathbf{x}, \omega = q_\parallel v_i) \cdot \mathbf{E}_{fi}(\mathbf{x}, \omega = q_\parallel v_i)\right], \tag{5.29}$$

which recovers the classical relationship [68, 195] between $\Gamma_{fi}^{\text{loss}}(\omega)$ and the work performed by the electron

against its own induced field. When the electron beam waist w_0 is negligible compared to the length scale over which the response field changes, $\mathbf{E}_{fi}$ can be taken as constant over the spatial domain where the current density is appreciable and approximated by its value $\mathbf{E}_{fi}(\mathbf{R}, z, \omega = q_\parallel v_i) \approx \mathbf{E}_{fi}(\mathbf{R}_0, z, \omega = q_\parallel v_i)$ at the impact parameter $\mathbf{R}_0$. In this narrow beam width limit, Eq. (5.29) becomes

$$\begin{aligned}\Gamma_{fi}^{\rm loss}(\mathbf{R}_0,\omega) &= -\frac{1}{\pi\hbar^2\omega}{\rm Re}\left[\int dz\left(\int d\mathbf{R}\,\mathbf{J}_{fi}^*(\mathbf{R},z,\omega=q_\parallel v_i)e^{i\omega z/v_i}\right)e^{-i\omega z/v_i}\cdot\mathbf{E}_{fi}(\mathbf{R}_0,z,\omega=q_\parallel v_i)\right]\\ &= -\frac{1}{\pi\hbar^2\omega}{\rm Re}\left[\boldsymbol{\mathcal{J}}_{fi}^*\cdot\int dz\,\mathbf{E}_{fi}(\mathbf{R}_0,z,\omega=q_\parallel v_i)e^{-i\omega z/v_i}\right],\end{aligned} \tag{5.30}$$

where the transition current $\boldsymbol{\mathcal{J}}_{fi} = \int d\mathbf{R}\,\mathbf{J}_{fi}(\mathbf{R}, z, \omega = q_\parallel v_i)e^{-i\omega z/v_i} = (-e/mv_i)\big[\langle\Psi_f|\hat{\mathbf{p}}_\perp|\Psi_i\rangle + (\hbar Q_\parallel/2)\langle\Psi_f|\Psi_i\rangle\hat{\mathbf{z}}\big]$ is z- and ω-independent. It has the transverse and longitudinal components $\boldsymbol{\mathcal{J}}_{fi}^\perp = -(e/mv_i)\langle\Psi_f|\hat{\mathbf{p}}_\perp|\Psi_i\rangle$ and $\boldsymbol{\mathcal{J}}_{fi}^\parallel = -(\hbar eQ_\parallel/2mv_i)\langle\Psi_f|\Psi_i\rangle\hat{\mathbf{z}}$, respectively, which allow the EEL probability in Eq. (5.30) to be separated into the perpendicular and parallel contributions

$$\begin{aligned}\Gamma_{fi\perp}^{\rm loss}(\mathbf{R}_0,\omega) &= -\frac{1}{\pi\hbar^2\omega}{\rm Re}\left[\boldsymbol{\mathcal{J}}_{fi}^{\perp *}\cdot\int dz\,\mathbf{E}_{fi}(\mathbf{R}_0,z,\omega=q_\parallel v_i)e^{-i\omega z/v_i}\right]\\ \Gamma_{fi\parallel}^{\rm loss}(\mathbf{R}_0,\omega) &= -\frac{1}{\pi\hbar^2\omega}{\rm Re}\left[\boldsymbol{\mathcal{J}}_{fi}^{\parallel *}\cdot\int dz\,\mathbf{E}_{fi}(\mathbf{R}_0,z,\omega=q_\parallel v_i)e^{-i\omega z/v_i}\right].\end{aligned} \tag{5.31}$$

Based on the forms of $\boldsymbol{\mathcal{J}}_{fi}^\perp$ and $\boldsymbol{\mathcal{J}}_{fi}^\parallel$ above, it is evident that $\boldsymbol{\mathcal{J}}_{fi}^\perp = \mathbf{0}$ and $\boldsymbol{\mathcal{J}}_{fi}^\parallel = -(\hbar eQ_\parallel/2mv_i)\hat{\mathbf{z}}$ in the event of no transverse transition (i.e., $\Psi_i = \Psi_f$ and $\Gamma_{fi\perp}^{\rm loss} = 0$), while $\boldsymbol{\mathcal{J}}_{fi}^\perp \neq \mathbf{0}$ and $\boldsymbol{\mathcal{J}}_{fi}^\parallel = \mathbf{0}$ when a transition occurs in the probe's transverse wave function (i.e., $\Psi_i \neq \Psi_f$ and $\Gamma_{fi\parallel}^{\rm loss} = 0$). In the former case, $\Gamma_{fi\parallel}^{\rm loss}(\mathbf{R}_0,\omega)$ in Eq. (5.31) reduces to the the well known classical form for the EEL probability [68,80,81,101] in the zero width limit $w_0 \to 0$. Specifically, $\Gamma_{fi\parallel}^{\rm loss}(\mathbf{R}_0,\omega) \to \Gamma_{\rm cl}(\mathbf{R}_0,\omega) = -(2e/\hbar)^2\int dzdz'\,{\rm Im}[\hat{\mathbf{z}}\cdot\overleftrightarrow{\mathbf{G}}(\mathbf{R}_0,z;\mathbf{R}_0,z',\omega)\cdot\hat{\mathbf{z}}\,e^{-i\omega(z-z')/v_i}]$, which is the EEL probability per unit energy for a uniformly moving classical electron with current density $\mathbf{J}_{\rm cl}(\mathbf{x},\omega) = -e\delta(\mathbf{R}-\mathbf{R}_0)e^{i\omega z/v_i}\,\hat{\mathbf{z}}$ at impact parameter $\mathbf{R}_0$.

To construct the laser-stimulated phase-shaped EEG observable in the narrow beam width limit, we again introduce $\varepsilon_{if} = \mathbf{v}_i\cdot\mathbf{q}$ into the trailing delta function in the frequency-resolved EEG rate presented in Eq. (5.11). As a result, the state- and frequency-resolved EEG rate and scattering probability is

$$w_{fi}^{\rm gain}(\omega) = \frac{2\pi}{v_i}\left(\frac{1}{\hbar\omega_\nu}\right)^2\left|\int d\mathbf{x}\,\mathbf{E}_\nu^{(+)}(\mathbf{x})\cdot\mathbf{J}_{fi}(\mathbf{x})\right|^2\delta(q_\parallel+\omega/v_i)\delta(\omega-\omega_{\nu\nu'}) \tag{5.32}$$

and $P_{fi}^{\rm gain}(\omega) = \big(L/v_i\big)w_{fi}^{\rm gain}(\omega)$. In parallel to loss, the EEG probability per unit energy is determined from $P_{fi}^{\rm gain}(\omega)$ after integrating over final states $\sum_{k_\parallel^f} \to +(L/2\pi)\int_{-\infty}^{\infty}dq_\parallel$ and dividing by $\hbar$, resulting in

$$\Gamma_{fi}^{\rm gain}(\omega) = \frac{1}{\hbar}\left(\frac{1}{\hbar\omega_\nu}\right)^2\left|\int d\mathbf{x}\,\mathbf{E}_\nu^{(+)}(\mathbf{x})\cdot\mathbf{J}_{fi}(\mathbf{x},\omega=-q_\parallel v_i)\right|^2\delta(\omega-\omega_{\nu\nu'}). \tag{5.33}$$

As in the case of loss, if the target's induced electric field varies little over the spatial domain of the probe's transition current density, then $\mathbf{E}_\nu^{(+)}(\mathbf{R},z) \approx \mathbf{E}_\nu^{(+)}(\mathbf{R}_0,z)$ to lowest order and the state- and energy-resolved

EEG probability takes the form

$$\begin{aligned}\Gamma_{fi}^{\text{gain}}(\mathbf{R}_0,\omega) &= \frac{1}{\hbar}\left(\frac{1}{\hbar\omega_\nu}\right)^2\left|\int dz\,\mathbf{E}_\nu^{(+)}(\mathbf{R}_0,z)e^{-i\omega z/v_i}\cdot\left[\int d\mathbf{R}\,\mathbf{J}_{fi}(\mathbf{R},z,\omega=-q_\parallel v_i)e^{i\omega z/v_i}\right]\right|^2\delta(\omega-\omega_{\nu\nu'})\\ &= \frac{1}{\hbar}\left(\frac{1}{\hbar\omega_\nu}\right)^2\left|\int dz\,e^{-i\omega z/v_i}\mathbf{E}_\nu^{(+)}(\mathbf{R}_0,z)\cdot\boldsymbol{\mathcal{J}}_{fi}\right|^2\delta(\omega-\omega_{\nu\nu'}),\end{aligned} \tag{5.34}$$

with z- and ω-independent transition current $\boldsymbol{\mathcal{J}}_{fi}$ defined below Eq. (5.30). As in the case of EEL, the EEG probability can also be broken into perpendicular and parallel components

$$\begin{aligned}\Gamma_{fi\perp}^{\text{gain}}(\mathbf{R}_0,\omega) &= \frac{1}{\hbar}\left(\frac{1}{\hbar\omega_\nu}\right)^2\left|\mathcal{J}_{fi}^{\perp}\right|^2\left|\int dz\,e^{-i\omega z/v_i}\mathbf{E}_\nu^{(+)}(\mathbf{R}_0,z)\cdot\hat{\boldsymbol{\mathcal{J}}}_{fi}^{\perp}\right|^2\delta(\omega-\omega_{\nu\nu'})\\ \Gamma_{fi\parallel}^{\text{gain}}(\mathbf{R}_0,\omega) &= \frac{1}{\hbar}\left(\frac{1}{\hbar\omega_\nu}\right)^2\left|\mathcal{J}_{fi}^{\parallel}\right|^2\left|\int dz\,e^{-i\omega z/v_i}\mathbf{E}_\nu^{(+)}(\mathbf{R}_0,z)\cdot\hat{\boldsymbol{\mathcal{J}}}_{fi}^{\parallel}\right|^2\delta(\omega-\omega_{\nu\nu'}),\end{aligned} \tag{5.35}$$

where $\boldsymbol{\mathcal{J}}_{fi}=\hat{\boldsymbol{\mathcal{J}}}_{fi}|\boldsymbol{\mathcal{J}}_{fi}|=\hat{\boldsymbol{\mathcal{J}}}_{fi}\mathcal{J}_{fi}$. Similarly, when the transverse wave functions $\Psi_i=\Psi_f$, $\Gamma_{fi}^{\text{gain}}(\mathbf{R}_0,\omega)=\Gamma_{fi\parallel}^{\text{gain}}(\mathbf{R}_0,\omega)$ and recovers the conventional EEG probability [5, 68, 90–92] in the narrow beam limit $w_0\to 0$. Through combination of optical polarization and pre- and post-selection of the probe's transverse phase profile to define its polarization, cross-polarized measurements in the STEM can be leveraged to directly interrogate optically-excited target mode symmetries in 3D with nanoscale spatial resolution [5].

The above expressions for EEL and EEG probabilities involve interrogation of the target's induced response field by the transition current densities $\mathbf{J}_{fi}(\mathbf{x},\omega=+q_\parallel v_i)$ and $\mathbf{J}_{fi}(\mathbf{x},\omega=-q_\parallel v_i)$ of the probe. It is natural to consider the relationship between these currents upon interchanging initial and final probe states in both the transverse and axial directions. The reciprocal behavior of pre- and post-selection of the probe's transverse states, i.e., $\mathbf{J}_{fi}^{\perp}(\mathbf{R})=\mathbf{J}_{if}^{\perp *}(\mathbf{R})$, were discussed previously in Sec. 5.3. Additionally, along the TEM axis, the longitudinal component $J_{fi}^{\parallel}(\mathbf{R})=J_{if}^{\parallel *}(\mathbf{R})$ expresses the relationship between anti-Stokes (EEG) and Stokes (EEL) scattering processes at the level of the transition current density. Taken together,

$$\begin{aligned}\mathbf{J}_{fi}(\mathbf{x},\omega=+q_\parallel v_i) &= \left(\frac{L}{v_i}\right)\left[\mathbf{J}_{if}^{\perp *}(\mathbf{R})+J_{if}^{\parallel *}(\mathbf{R})\hat{\mathbf{z}}\right]e^{i(\omega/v_i)z}\\ &= \left(\frac{L}{v_i}\right)\left(\left[\mathbf{J}_{if}^{\perp}(\mathbf{R})+J_{if}^{\parallel}(\mathbf{R})\hat{\mathbf{z}}\right]e^{-i(\omega/v_i)z}\right)^*\\ &= \mathbf{J}_{if}^{*}(\mathbf{x},\omega=-q_\parallel v_i).\end{aligned} \tag{5.36}$$

These symmetries of the transition current density under interchange of initial and final states, and their effect on the observables, is detailed further in the Appendix.

5.4.2 Double differential inelastic scattering cross section in the wide field limit

When dealing with plane wave electron states, the scattering cross section is a common observable of interest. It is attained from the EEL transition rate $w_{fi}^{\text{loss}}(\omega)$ in Eq. (5.9) by first summing over the electron final states $\sum_{\mathbf{k}_f} \to (L/2\pi)^3 \int d\mathbf{k}_f$ and subsequently dividing by the incoming plane wave particle flux $\hbar k_i/mL^3$. The total frequency-resolved scattering cross section is given by

$$\sigma(\omega) = \frac{mL^3}{\hbar k_i}\Big(\frac{L}{2\pi}\Big)^3 \int d\Omega_f \, k_f^2 \, dk_f \, w_{fi}(\omega), \tag{5.37}$$

and by integration over frequency, the angle-resolved scattering cross section is

$$\begin{aligned} \frac{\partial \sigma}{\partial \Omega_f} &= \frac{mL^3}{\hbar k_i}\Big(\frac{L}{2\pi}\Big)^3 \int d\omega \, k_f^2 \, dk_f \, w_{fi}(\omega) \\ &= -\frac{mL^3}{\hbar k_i}\Big(\frac{L}{2\pi}\Big)^3 \int d\omega \, dE_{if} \left(\frac{\gamma_f m}{\hbar^2 k_f}\right) k_f^2 \, w_{fi}(\omega), \end{aligned} \tag{5.38}$$

where $dE_{if} = -(\hbar^2/m)k_f dk_f$ and $d\Omega_f = \sin\theta_f d\theta_f d\phi_f$. Lastly, noting that $\partial\sigma/\partial\Omega_f = \int dE_{if} \partial^2\sigma/(\partial E_{if}\partial\Omega_f)$, the double differential scattering cross section (DDCS) is defined as

$$\begin{aligned} \frac{\partial^2 \sigma}{\partial E_{if}\partial \Omega_f} &= -\frac{m^2 L^3}{\hbar^3}\Big(\frac{L}{2\pi}\Big)^3 \left(\frac{k_f}{k_i}\right) \int d\omega \, w_{fi}(\omega) \\ &= \Big(\frac{mL^3}{\pi\hbar^2}\Big)^2 \left(\frac{k_f}{k_i}\right) \int d\omega \, d\mathbf{x} d\mathbf{x}' \, \mathrm{Im}\Big[\mathbf{J}_{fi}^*(\mathbf{x}) \cdot \overleftrightarrow{\mathbf{G}}(\mathbf{x},\mathbf{x}',\omega) \cdot \mathbf{J}_{fi}(\mathbf{x}')\Big] \delta(\omega - \varepsilon_{if}), \end{aligned} \tag{5.39}$$

which reduces to the DDCS common for an isolated dipolar target Eq. (5.41) in core-loss EEL scattering [4, 118, 196] when the electrostatic limit where $c \to \infty$ is taken. Further analytic progress is possible in the case of a single target dipole located at position $\mathbf{x}_d$ and characterized by frequency-dependent polarizability tensor $\overleftrightarrow{\boldsymbol{\alpha}}(\omega)$. In this case, the induced Green's function reduces to $\overleftrightarrow{\mathbf{G}}(\mathbf{x},\mathbf{x}',\omega) = -(4\pi\omega^2)\overleftrightarrow{\mathbf{G}}^0(\mathbf{x},\mathbf{x}_d,\omega) \cdot \overleftrightarrow{\boldsymbol{\alpha}}(\omega) \cdot \overleftrightarrow{\mathbf{G}}^0(\mathbf{x}_d,\mathbf{x}',\omega)$, where $\overleftrightarrow{\mathbf{G}}^0(\mathbf{x},\mathbf{x}',\omega) = -1/(4\pi\omega^2)[(\omega/c)^2\overleftrightarrow{\mathbf{I}} + \nabla\nabla]e^{i(\omega/c)|\mathbf{x}-\mathbf{x}'|}/|\mathbf{x}-\mathbf{x}'|$ is the vacuum dipole Green's function, and the DDCS can be expressed analytically. Specifically, with a single incoming plane wave scattering to a single outgoing plane wave as described by the transition current density given by Eq. (5.18), the fully retarded DDCS becomes

$$\frac{\partial^2 \sigma}{\partial E_{if}\partial \Omega_f} = \frac{e^2}{\hbar^2\pi}\left(\frac{k_f}{k_i}\right)\frac{1}{\varepsilon_{if}^2}\,\mathrm{Im}\Bigg\{\mathbf{Q}\cdot\left[\left(\frac{\varepsilon_{if}}{c}\right)^2\overleftrightarrow{\mathbf{I}} - \mathbf{qq}\right]\cdot\frac{\overleftrightarrow{\boldsymbol{\alpha}}(\varepsilon_{if})}{\left|(\varepsilon_{if}/c)^2 - q^2\right|^2}\cdot\left[\left(\frac{\varepsilon_{if}}{c}\right)^2\overleftrightarrow{\mathbf{I}} - \mathbf{qq}\right]\cdot\mathbf{Q}\Bigg\}, \tag{5.40}$$

where $\mathbf{Q} = 2\mathbf{k}_i - \mathbf{q}$. In the quasistatic limit ($c \to \infty$), Eq. (5.40), reduces to the more familiar form [50]

$$\frac{\partial^2 \sigma}{\partial E_{if}\partial \Omega} = \frac{e^2}{\hbar^2\pi}\left(\frac{k_f}{k_i}\right)\frac{1}{\varepsilon_{if}^2}\,\mathrm{Im}\left[\mathbf{Q}\cdot\mathbf{qq}\cdot\frac{\overleftrightarrow{\boldsymbol{\alpha}}(\varepsilon_{if})}{q^4}\cdot\mathbf{qq}\cdot\mathbf{Q}\right]. \tag{5.41}$$

5.5 Numerical Implementation

This section details the numerical implementation of the inelastic scattering observables presented above in Secs. 5.4.1 and 5.4.2 for transversely phase-structured free electrons in both the focused beam and wide field limits. Our implementation generalizes the electron-driven discrete dipole approximation (e-DDA) [135,136], built on top of the DDCSAT [140] framework, which previously utilized the vacuum electric field $\mathbf{E}^0_{fi}$ of a point electron as the source instead of an optical plane wave field. Other fully retarded and quasistatic numerical methods for simulating extended nanophotonic targets have been formulated to model low-loss electron beam interactions, such as the finite-difference time-domain [197,198], metal nanoparticle boundry element (MNPBEM) [199], and finite element [200,201] methods. In addition, transversely structured electron beams have been implemented in MNPBEM [48,89,127,187], albeit in the quasistatic limit only. Our treatment of the inelastic scattering of transversely structured electron beams in e-DDA is distinguished by its incorporation of fully retarded electron-sample interactions in both focused beam and wide field limits.

e-DDA/DDA originate from the method of coupled dipoles [202], whereby the target is discretized into a finite collection of point electric dipoles

$$\mathbf{p}_k(\omega) = \sum_{l=1}^{N} \Big[\overleftrightarrow{\boldsymbol{\alpha}}(\omega)^{-1} - (-4\pi\omega^2)\overleftrightarrow{\mathbf{G}}^0(\omega) \Big]^{-1}_{kl} \cdot \mathbf{E}^0_{fi}(\mathbf{x}_l, \omega) \tag{5.42}$$

of polarizability $\overleftrightarrow{\boldsymbol{\alpha}}(\omega)$, each driven by the vacuum transition field $\mathbf{E}^0_{fi}(\mathbf{x}_i, \omega)$ at frequency ω and mutually interacting via their fully-retarded electric dipole fields $-4\pi\omega^2 \sum_l \overleftrightarrow{\mathbf{G}}^0_{kl}(\omega) \cdot \mathbf{p}_l(\omega)$ until reaching self-consistency at that same frequency. Here $\overleftrightarrow{\mathbf{G}}^0_{kl}(\omega)$ are the kl-matrix elements of the vacuum dipole Green's function $\overleftrightarrow{\mathbf{G}}^0(\mathbf{x}, \mathbf{x}', \omega)$.

Upon inversion of Eq. (5.42), all EEL observables described above may be calculated from the resulting $\mathbf{p}_k(\omega)$ together with the applied field $\mathbf{E}^0_{fi}(\mathbf{x}_k, \omega)$ (Eq. (5.47)) evaluated at each dipole. Specifically, the focused beam EEL probability and the wide field DDCS expressions in Eq. (5.28) and Eq. (5.39), respectively, can be adapted to a form that is compatible with the e-DDA code via the EEL rate per unit frequency

$$\begin{aligned} w^{\text{loss}}_{fi}(\omega) &= -\frac{8\pi}{\hbar} \int d\mathbf{x} d\mathbf{x}' \, \text{Im}\Big[\mathbf{J}^*_{fi}(\mathbf{x}) \cdot \overleftrightarrow{\mathbf{G}}(\mathbf{x}, \mathbf{x}', \omega) \cdot \mathbf{J}_{fi}(\mathbf{x}') \Big] \delta(\omega - \varepsilon_{if}) \\ &= \frac{2}{\hbar} \Big(\frac{v_i}{L} \Big)^2 \text{Im}\Big[\sum_k \mathbf{E}^{0*}_{fi}(\mathbf{x}_k, \omega) \cdot \mathbf{p}_k(\omega) \Big] \delta(\omega - \varepsilon_{if}). \end{aligned} \tag{5.43}$$

Here the target's induced Green's function $\overleftrightarrow{\mathbf{G}}(\mathbf{x}, \mathbf{x}', \omega)$ is expanded in terms of the polarizabilities of the N dipoles representing the target. That is

$$\overleftrightarrow{\mathbf{G}}(\mathbf{x}, \mathbf{x}', \omega) = -4\pi\omega^2 \sum_{jj'} \overleftrightarrow{\mathbf{G}}^0(\mathbf{x}, \mathbf{x}_j, \omega) \cdot \big[\overleftrightarrow{\boldsymbol{\alpha}}^{-1}(\omega) - (-4\pi\omega^2)\overleftrightarrow{\mathbf{G}}^0(\omega) \big]^{-1}_{jj'} \cdot \overleftrightarrow{\mathbf{G}}^0(\mathbf{x}_{j'}, \mathbf{x}', \omega), \tag{5.44}$$

which can be derived from the response field of a polarizable body described in terms of its induced Green's

function $\overleftrightarrow{\mathbf{G}}(\mathbf{x},\mathbf{x}',\omega)$ driven by the external current density $\mathbf{J}^0(\mathbf{x})$ or by the free propagation (via $\overleftrightarrow{\mathbf{G}}^0(\mathbf{x},\mathbf{x}',\omega)$) of the target's induced current density $\mathbf{J}(\mathbf{x}) = \sum_j (-i\omega)\mathbf{p}_j(\omega)\delta(\mathbf{x}-\mathbf{x}_j)$ as $\mathbf{E}(\mathbf{x},\omega) = -4\pi i\omega \int d\mathbf{x}'\, \overleftrightarrow{\mathbf{G}}(\mathbf{x},\mathbf{x}',\omega)\cdot \mathbf{J}^0(\mathbf{x}') = -4\pi i\omega \int d\mathbf{x}'\, \overleftrightarrow{\mathbf{G}}^0(\mathbf{x},\mathbf{x}',\omega)\cdot\mathbf{J}(\mathbf{x}')$.

5.5.1 Numerical evaluation of state- and energy-resolved EEL and EEG probabilities

From Eq. (5.43), the state- and energy-resolved EEL probability can be obtained following the same procedure in Sec. 5.4.1. Specifically, the transversely phase-shaped EEL probability becomes

$$\Gamma_{fi}^{\text{loss}}(\omega) = \frac{1}{\pi\hbar^2}\text{Im}\Big[\sum_k \mathbf{E}_{fi}^{0*}(\mathbf{x}_k, \omega = q_\parallel v_i)\cdot\mathbf{p}_k(\omega = q_\parallel v_i)\Big], \tag{5.45}$$

when working within the nonrecoil approximation introduced in Sec. 5.4, as appropriate to focused beams prepared in the STEM configuration. The vacuum transition electric field $\mathbf{E}_{fi}^0$ appearing within Eq. (5.42) and Eq. (5.45) can, in principle, be any of the fields sourced by the transversely focused transition current densities described in Sec. 5.3. However, due to their complexity, only those transitions involving OAM transfers $\Delta\ell = 1$ depicted as colored arrows in Fig. 5.2(e), and more specifically the resulting electric fields sourced by the transition current densities seen in Fig. 5.3(c) and 5.3(d), have been implemented within the *e*-DDA code. Explicit forms for these fields are provided in the Appendix. Phase-shaped EEG probability spectra of nanophotonic targets under continuous-wave laser stimulation can also be evaluated numerically using the *e*-DDA as detailed previously [5]. Briefly, the EEG probability in Eq. (5.34) is numerically integrated by quadrature using the optically-induced response field of the target $\mathbf{E}_\nu^{(+)}$ calculated using DDCSAT and the $\hat{\mathbf{J}}_{fi}$ defined by selection of a specific pair of incoming and outgoing free electron states.

Figure 5.4 presents a comparison of normalized focused beam EEL and EEG spectra for a 25 nm radius silver sphere calculated using *e*-DDA with dielectric data taken from Ref. [203]. Probing electrons have a speed of $0.7c$. Panel (a) shows phase-structured EEL (solid traces) and EEG (dashed traces) spectra at impact parameter $\mathbf{R}_0 = (1/\sqrt{2})(40\text{ nm}, 40\text{ nm})$. The optical excitation polarization $\hat{\boldsymbol{\epsilon}}$ in the EEG calculations is along $\hat{\mathbf{x}}$. Gray and magenta colors correspond to pre- and post-selection of HG transitions $\Psi_{00}(x,y) \to \Psi_{00}(x,y)$ with $\hat{\boldsymbol{\mathcal{J}}}_{fi}^{\parallel} = \hat{\mathbf{z}}$, and $\Psi_{10}(x,y) \to \Psi_{00}(x,y)$ with $\hat{\boldsymbol{\mathcal{J}}}_{fi}^{\perp} = \hat{\mathbf{x}}$, respectively. While the *e*-DDA calculations can capture coupling to the higher-order multipoles, as seen in Fig. 5.4(a), the dipolar localized surface plasmon (LSP) is clearly evident near 3.4 eV. Here it is apparent that both transitions with $\hat{\boldsymbol{\mathcal{J}}}_{fi}$ oriented parallel and perpendicular to the electron trajectory couple to the quadrupolar LSP mode near 3.6 eV, albeit with different strengths. The EEG spectra, meanwhile, are dominated by the optically bright dipolar response of the sphere, whereas the higher-order, dark modes are inaccessible by the stimulating optical pump field.

EEL spectrum images obtained by plotting $\Gamma_{fi}^{\text{loss}}(\mathbf{R}_0,\omega)$ as a function of the impact parameter $\mathbf{R}_0$ at the dipole LSP energy 3.4 eV are shown in Fig. 5.4(b). In the conventional EEL case, where $\hat{\boldsymbol{\mathcal{J}}}_{fi}^{\perp} = \mathbf{0}$ resulting

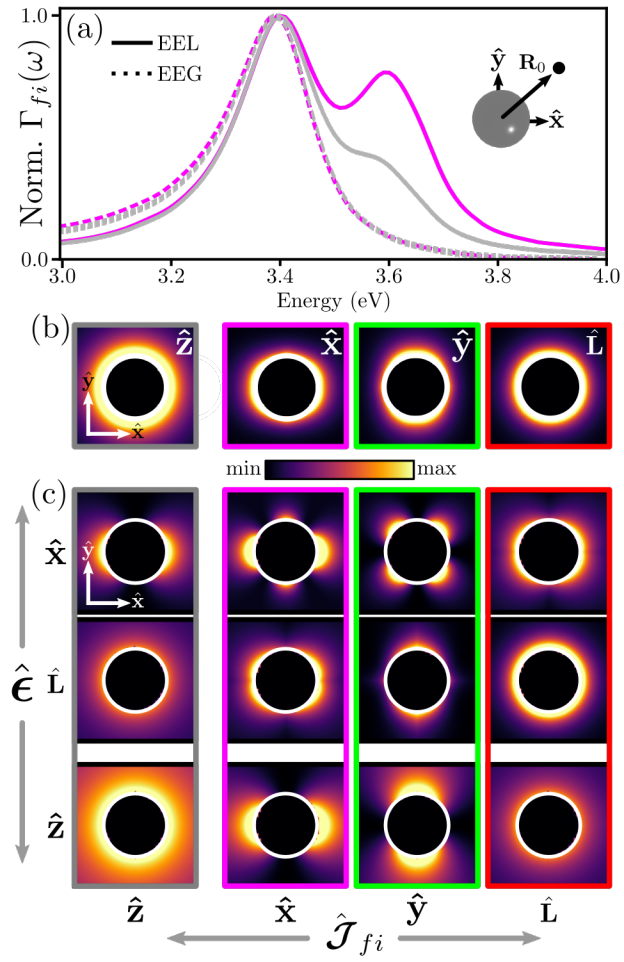

Figure 5.4: Phase-shaped EEL and EEG point spectra and spectrum images of a silver plasmonic sphere of 25 nm radius evaluated using *e*-DDA. (a) Phase-shaped EEL (solid) and EEG (dashed) point spectra, evaluated in the narrow beam limit, at impact parameter $\mathbf{R}_0 = (1/\sqrt{2})(40\text{ nm}, 40\text{ nm})$. The optical polarization is $\hat{\boldsymbol{\epsilon}} = \hat{\mathbf{x}}$ in the laser-stimulated EEG calculations. Gray and magenta colors correspond to $\hat{\boldsymbol{\mathcal{J}}}_{fi}$ along $\hat{\mathbf{z}}$ and $\hat{\mathbf{x}}$, respectively. (b) Phase-shaped EEL spectrum images at the dipole LSP resonance energy of 3.4 eV. Each column corresponds to the labeled $\hat{\boldsymbol{\mathcal{J}}}_{fi}$. (c) Phase-shaped EEG spectrum images at 3.4 eV. The optical excitation polarization state $\hat{\boldsymbol{\epsilon}}$ varies between rows, while each column corresponds to the labeled $\hat{\boldsymbol{\mathcal{J}}}_{fi}$. For $\hat{\boldsymbol{\epsilon}} = \{\hat{\mathbf{x}}, \hat{\mathbf{L}}\}$, the optical axis is chosen to be along $\hat{\mathbf{z}}$, while for $\hat{\boldsymbol{\epsilon}} = \hat{\mathbf{z}}$ it is chosen to be along $\hat{\mathbf{x}}$. Panels with $\hat{\boldsymbol{\mathcal{J}}}_{fi} = \{\hat{\mathbf{x}}, \hat{\mathbf{y}}, \hat{\mathbf{L}}\}$ and with $\hat{\boldsymbol{\epsilon}} = \{\hat{\mathbf{x}}, \hat{\mathbf{L}}\}$ share a common scale, while panels with $\hat{\boldsymbol{\mathcal{J}}}_{fi} = \hat{\mathbf{z}}$ are separately scaled. The incident velocity of the probing electron is $\mathbf{v}_i = 0.7c\,\hat{\mathbf{z}}$ in all cases.

in $\hat{\boldsymbol{\mathcal{J}}}_{fi} = \hat{\boldsymbol{\mathcal{J}}}^{\parallel}_{fi} = \hat{\mathbf{z}}$ (gray, left), the spectrum image exhibits the expected circular symmetry. Meanwhile, when $\hat{\boldsymbol{\mathcal{J}}}^{\perp}_{fi} \neq \mathbf{0}$, producing a $\hat{\boldsymbol{\mathcal{J}}}^{\perp}_{fi}$ oriented along $\hat{\mathbf{x}}$ ($\hat{\mathbf{y}}$), and outlined in magenta (green), the spectrum image shows slight elongation along the direction of the transition current density. As required by symmetry, the circularly-polarized $\hat{\boldsymbol{\mathcal{J}}}^{\perp}_{fi} = \hat{\mathbf{L}}$ (red) couples with radial symmetry to the spherical target. In Fig. 5.4(b), the $\hat{\boldsymbol{\mathcal{J}}}^{\parallel}_{fi} = \hat{\mathbf{z}}$ plot is normalized to a maximum of 10^{-2} eV^{-1}, while the $\hat{\boldsymbol{\mathcal{J}}}^{\perp}_{fi} \in \{\hat{\mathbf{x}}, \hat{\mathbf{y}}, \hat{\mathbf{L}}\}$ cases share a common normalization factor of 10^{-8} eV^{-1} for a beam waist of 1 nm. The small perpendicular to parallel ratio of signals represents a hurdle to phase-shaped EEL spectroscopy measurements regarding limits of detection, although measurements of this type have been achieved previously [49]. Phase-shaped EEG spectrum images at the same dipole LSP energy 3.4 eV are presented in Fig. 5.4(c). The optical excitation polarization state $\hat{\boldsymbol{\epsilon}}$ varies between rows, while each column corresponds to the labeled component of $\hat{\boldsymbol{\mathcal{J}}}_{fi}$. For $\hat{\boldsymbol{\epsilon}} = \{\hat{\mathbf{x}}, \hat{\mathbf{L}}\}$, the optical axis is chosen to be along $\hat{\mathbf{z}}$. There $\hat{\boldsymbol{\mathcal{J}}}^{\perp}_{fi} = \hat{\mathbf{x}}$, $\hat{\mathbf{y}}$, and $\hat{\mathbf{L}}$ share a common scale factor, while $\hat{\boldsymbol{\mathcal{J}}}_{fi} = \hat{\mathbf{z}}$ is separately scaled. The ratio of the transverse to longitudinal EEG probabilities is $\Gamma^{\text{gain}}_{fi\perp}/\Gamma^{\text{gain}}_{fi\parallel} \approx 10^{-5}$, for a 200 keV electron beam with a waist 1 nm. These findings are consistent with earlier theoretical [5] and experimental [105] studies. For the $\hat{\boldsymbol{\epsilon}} = \hat{\mathbf{z}}$ case, the optical axis is chosen to be along $\hat{\mathbf{x}}$ and the ratio of transverse to longitudinal EEG signals remains similarly small ($\sim 10^{-5}$), but all signals are smaller by $\sim 10^{-3}$ in this excitation geometry. Comparison of Figs. 5.4(b) and 5.4(c) highlights the differing identities of the excitation sources and roles played by $\mathbf{J}_{fi}$ in EEL and laser-stimulated EEG processes. When considering EEL events, the STEM electron acts as both a spatially dependent pump and probe sourced by the transition current density $\mathbf{J}_{fi}(\mathbf{R}_0)$ at impact parameter $\mathbf{R}_0$. In stark contrast, as alluded to in Sec. 5.1, the pump and the probe are decoupled for laser-stimulated EEG processes. Specifically, as seen in Eq. (5.11), the pump is the optical source exciting the target's induced field $\mathbf{E}^{(+)}_{\nu}$, which is then probed by the electron's transition current density $\mathbf{J}_{fi}(\mathbf{R}_0)$ at $\mathbf{R}_0$.

5.5.2 Numerical evaluation of the inelastic double differential cross section

From Eqs. (5.39) and (5.43), the wide field inelastic DDCS can be expressed as

$$\begin{aligned}\frac{\partial^2\sigma}{\partial E_{if}\partial\Omega_f} &= -\frac{m^2L^6}{(2\pi)^3\hbar^3}\left(\frac{k_f}{k_i}\right)\int d\omega\, w^{\text{loss}}_{fi}(\omega) \\ &= -\frac{1}{4\pi^3}\frac{k_f}{k_i}\left(\frac{v_i m L^2}{\hbar^2}\right)^2 \text{Im}\Big[\sum_j \mathbf{E}^{0*}_{fi}(\mathbf{x}_j, \omega = \varepsilon_{if})\cdot\mathbf{p}_j(\omega = \varepsilon_{if})\Big].\end{aligned} \tag{5.46}$$

We have implemented within *e*-DDA the plane wave transition fields defined in Appendix Eqs. (5.50) and (5.52), sourced by the transition currents Eqs. (5.18) and (5.19), respectively, for the cases of scattering from either a single or a coherent superposition of two incident plane waves, to a single outgoing plane wave state.

The DDCSs for inelastic scattering of wide field plane wave electron states from plasmonic nanorod monomers and dimers are presented in Fig. 5.5. Probing electrons have an initial kinetic energy of 200 keV and wave vector directed along the TEM axis, i.e., $\hat{\mathbf{k}}_i = \hat{\mathbf{z}}$, while the outgoing wave vectors $\mathbf{k}_f$ possess a

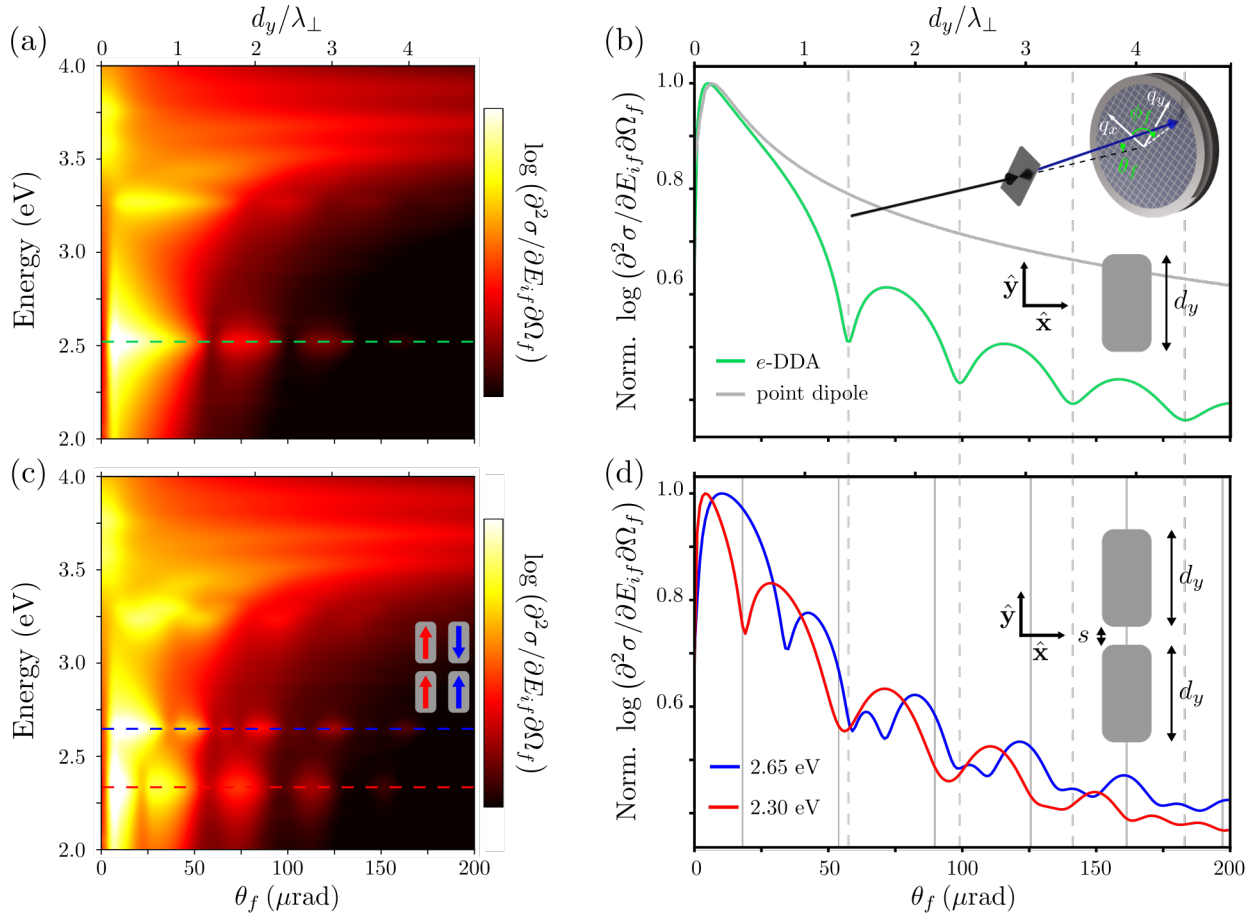

Figure 5.5: DDCSs for plasmonic nanorod monomer and dimer systems evaluated using e-DDA. (a) Numerically calculated DDCS (logarithmic scale) for a silver nanorod with Cartesian dimensions of 30 nm × 60 nm × 15 nm. The incident electron is directed along $\hat{\mathbf{z}}$ with 200 keV kinetic energy and the collected scattering direction is varied from $\theta_f = 0$ μrad (along $\hat{\mathbf{z}}$) to $\theta_f = 200$ μrad, with $\phi_f = \pi/2$ fixed such that $\mathbf{q}_\perp = q_\perp\hat{\mathbf{y}}$. The quantity $d/\lambda_\perp$ (upper horizontal axis) is the rod length (60 nm) along the momentum recoil direction divided by the transverse recoil wavelength $\lambda_\perp = 2\pi/q_\perp$. (b) Lineout of the DDCS in panel (a) at 2.5 eV (green). The gray trace is the DDCS of an anisotropic point dipole evaluated using the analytic expression in Eq. (5.40). Vertical gray dashed lines indicate single particle diffraction minima. Insets show schematic depictions of the scattering and target geometries. (c) Same as (a), but for a homodimer target composed of two copies of the nanostructure considered in (a) and (b) arranged tip-to-tip along the y-axis with an $s = 10$ nm gap. (d) Lineouts from (c) at 2.30 eV (red) and 2.65 eV (blue). Vertical gray dashed lines indicate single slit diffraction minima, while solid gray lines denote double slit interference minima at 2.30 eV.

nonzero y-component such that the transverse momentum recoil $\hbar\mathbf{q}_\perp$ is along $\hat{\mathbf{y}}$. Working in the low loss energy regime in order to observe the plasmonic modes of interest, Fig. 5.5(a) shows the calculated DDCS (logarithmic scale) for an anisotropic silver rod with Cartesian dimensions 30 nm × 60 nm × 15 nm (width, length, height) as a function of scattering angle θ_f and loss energy. The nanorod is orientated with its longest dimension d_y along the direction of collected transverse recoils ($\phi_f = \pi/2$), leading to the lowest energy long-axis dipole mode near 2.50 eV dominating the DDCS. Since the transversely polarized components of the transition field $\mathbf{E}^0_{fi}$ in Eq. (5.50) are proportional to $\mathbf{q}_\perp$, transversely oriented LSP modes of the nanorod do not contribute to the DDCS at $\theta_f = 0$ μrad. The apparent features at $\theta_f = 0$ μrad and energies above 3.50 eV in Fig. 5.5(a) arise from longitudinal multipoles oriented along $\hat{\mathbf{z}}$.

Figure 5.5(b) shows a lineout from panel (a) at the long-axis dipole LSP energy marked by the dashed green line. The gray trace in Fig. 5.5(b) is calculated using the analytic form of the DDCS given in Eq. (5.40) for a single point dipole representing the target. The anisotropy of the nanorod response is captured by detuning the shorter axis dipole LSP energies above 2.50 eV in the dipole's effective polarizability. As a consequence, $\partial^2\sigma/\partial E_{if}\partial\Omega_f \propto |\mathbf{E}^0_{fi}\cdot\hat{\mathbf{y}}|^2$, which ensures $\partial^2\sigma/\partial E_{if}\partial\Omega_f|_{\theta_f=0} = 0$. At moderate opening angles ($\gtrsim 5$ μrad) the DDCS decreases as the opening angle increases, which starting from Eq. (5.50) and $Q_\parallel \gg |\mathbf{Q}_\perp| = |\mathbf{q}_\perp|$ can be shown by $\mathbf{E}^0_{fi}\cdot\hat{\mathbf{y}} \propto Q_\parallel q_\parallel \mathbf{q}_\perp\cdot\hat{\mathbf{y}}/\left(\mathbf{q}_\perp^2 + q_\parallel^2 - \omega^2/c^2\right) = Q_\parallel q_\parallel |\mathbf{k}_f|\sin\theta_f/\left[|\mathbf{k}_f|^2\sin^2\theta_f + \omega^2(1/v_i^2 - 1/c^2)\right]$. For a 200 keV electron with loss energy $\hbar\epsilon_{if} = 2.5$ eV, $|\mathbf{k}_f|\sin\theta_f \gtrsim \omega/(\gamma_i v_i)$ at opening angles $> 5\,\mu$rad, leading to $\partial^2\sigma/\partial E_{if}d\Omega_f \propto 1/\sin^2\theta_f$. This effect exists independent of the target geometry and represents the decreasing probability of low loss events with moderate transverse recoil. Separately the lineouts in θ_f on the order of 5 μrad range are primarily dictated by the growing in of the transverse LSP mode, as at smaller angles $\mathbf{E}^0_{fi}\cdot\hat{\mathbf{y}} \propto \mathbf{q}\cdot\hat{\mathbf{y}} = |\mathbf{k}_f|\sin\theta_f$ and the lineout is taken at the $\hat{\mathbf{y}}$ oriented dipole mode energy. Unlike in the narrow beam limit, the DDCS observable has equal magnitude contributions from transverse and longitudinal recoils, which is a well known experimental and theoretical result of EEL DDCS on an anisotropic target [196, 204]. In addition to tracking the angular scattering behavior predicted by the point dipole model at small scattering angles ($\lesssim 25$ μrad), the lineout shown in green exhibits a progression of diffraction maxima/minima with increasing θ_f arising from the finite extent of the target. The single particle diffraction minima, indicated by vertical gray dashed lines, are located nearby angles θ_m corresponding to single slit diffraction minima predicted using $d_y\sin\theta_m = m\lambda_e$, where integers m index the diffraction minima, and λ_e is the de Broglie wavelength of the electron.

Figures 5.5(c) and 5.5(d) consider a nanorod dimer consisting of a pair of the silver rods from Figs. 5.5(a) and 5.5(b) displaced along $\hat{\mathbf{y}}$ such that there is an $s = 10$ nm gap between the rod tips. The dimer's DDCS is presented in Fig. 5.5(c), where the bonding (red) and antibonding (blue) hybridized long-axis dipole LSP modes are visible at energies slightly below and above 2.5 eV, respectively. Lineouts from Fig. 5.5(c) at loss energies corresponding to the bonding and antibonding dimer modes are shown in Fig. 5.5(d), again displaying multiple diffraction minima/maxima. In analogy to the double slit experiment, each nanorod is a source of single-particle diffraction in addition to matter-wave interference arising from the $d_\perp + s = 70$ nm center-to-

center displacement of the the nanorods. For example, each DDCS minimum observed at the bonding mode energy (2.30 eV) occurs at an angle corresponding to either one of the single-particle diffraction minima from Fig. 5.5(b) marked by vertical gray dashed lines, or at angles θ_n satisfying the double slit interference condition $n\lambda_\perp = d_y + s$, which are indicated by vertical gray solid lines. The condition for constructive interference at the antibonding resonance energy is $(n + 1/2)\lambda_\perp = d_y + s$.

An investigation of inelastic scattering involving superposition plane wave electron states interacting with a chiral nanophotonic target is presented in Fig. 5.6. Specifically, the target is the well-understood Born-Kuhn structure (BK) [110], composed of two gold nanorods arranged in an L-shape with a relative displacement ζ between the rods centered along $\hat{\mathbf{z}}$, as demonstrated in Fig. 5.6(a). Here, the long and short axes of each nanorod are 100 nm and 30 nm, respectively, $\zeta = 40$ nm, and tabulated gold dielectric data are taken from the literature [203]. Fig. 5.6(b) shows the optical extinction spectra of the BK target for incident wave vectors along $\hat{\mathbf{z}}$ and polarizations $\hat{\boldsymbol{\epsilon}} = \hat{\mathbf{L}}$ (red) and $\hat{\mathbf{R}}$ (blue). As is well-understood (see Appendix) [111, 112] both incident field helicities couple, albeit with unequal strengths, to the bonding and antibonding LSP modes near 2.0 eV involving the long-axis dipoles. The optical circular dichroism $\mathrm{CD}_{\mathrm{opt}} = 2(\sigma_{\mathrm{ext}}^{\hat{\mathbf{R}}} - \sigma_{\mathrm{ext}}^{\hat{\mathbf{L}}})/(\sigma_{\mathrm{ext}}^{\hat{\mathbf{R}}} + \sigma_{\mathrm{ext}}^{\hat{\mathbf{L}}})$ spectrum is shown in black, which exhibits the BK system's chiral response and serves as a point of comparison against the electron-based observables.

As depicted in Fig. 5.6(a), free electron plane wave superposition states $\psi^{\chi}_{k_x k_y}(x, y, z)$ are incident from the left, while an aperture situated in the diffraction plane post-selects the outgoing free electrons along the TEM axis with $\mathbf{k}^f_\perp = \mathbf{0}$, i.e, $\psi_{k'_\parallel}(x, y, z)$. It has been shown previously that the response of targets as measured by wide field EEL spectroscopy with pre- and post-selection of such states with $k_x = k_y$ and $\chi = \pm\pi/2$ in many ways mimic the optical response under circularly polarized optical excitation [4, 54, 118]. Indeed, Fig. 5.6(c) presents DDCS spectra of the BK target for $\psi^{\chi}_{k_x k_y}(x, y, z) \to \psi_{k'_\parallel}(x, y, z)$, producing the transition current density given by Eq. (5.19), for the scenarios of $\chi = \pm\pi/2$. The circular dichroism $\mathrm{CD}_{\mathrm{EEL}}$ (black) is again defined as twice the difference in the $\chi = \pm\pi/2$ DDCS spectra normalized by the sum, and strongly resembles the $\mathrm{CD}_{\mathrm{opt}}$ spectrum in Fig. 5.6(b). Panel (c) presents the $\mathrm{CD}_{\mathrm{EEL}}$ spectra as a function of convergence angle θ_i. Like the nanorod dimer presented in Fig. 5.5, the BK system exhibits both single slit diffraction and double slit interference effects (Fig. 5.6(d)), though the superposition state excitation and BK target geometry conspire to produce more complicated beating patterns than those observed in Fig. 5.5(c). The vertical dashed gray line in Fig. 5.6(d) indicates the convergence angle θ_i of the spectra presented in panel (c).

5.6 Conclusions

Development of capabilities to prepare, parse, and measure transversely phase-structured electron states in the electron microscope has opened the door to state- and energy-resolved inelastic scattering observables, adding to the rapidly evolving toolkit used to interrogate nanoscale systems in the low-loss regime. Here we

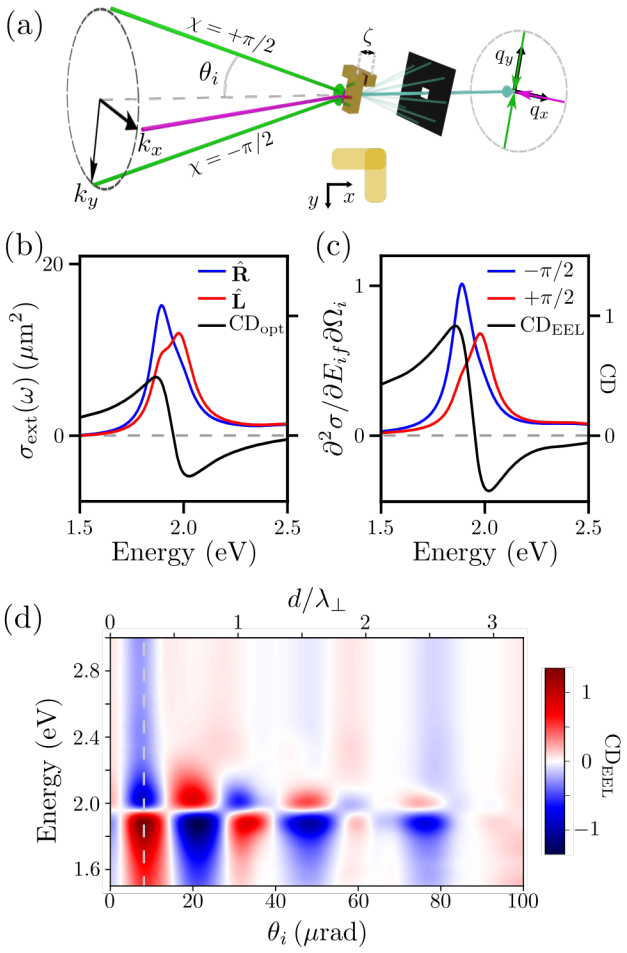

Figure 5.6: Numerical evaluation of the circular dichroic response of a chiral nanorod structure probed using wide field EEL spectroscopy within e-DDA. (a) Scheme showing the gold nanorod BK structure and probing geometries. Superposition plane wave electron states are incident from the left, while an aperture (black) post-selects the outgoing electron state along the TEM ($\hat{\mathbf{z}}$) axis. (b) Optical extinction spectra for incident plane wave wave vectors along $\hat{\mathbf{z}}$ with circular polarization states $\hat{\boldsymbol{\epsilon}} = \hat{\mathbf{R}}$ (blue) and $\hat{\mathbf{L}}$ (red). The optical circular dichroism $\mathrm{CD_{opt}}$ is shown in black and shares its secondary y-axis with panel (c). (c) DDCS spectra of the same BK structure for superposition plane wave electron states with $\chi = +\pi/2$ (red) and $\chi = -\pi/2$ (blue). The $\mathrm{CD_{EEL}}$ spectrum is shown in black. (d) Angle θ_i-resolved $\mathrm{CD_{EEL}}$ spectra. The dashed gray line in (d) indicates the fixed angle of the lineouts in (c). The incident electron kinetic energy in (c,d) is 200 keV.

present general expressions for transversely phase-shaped EEL and continuous-wave laser-stimulated EEG spectroscopies for transversely localized vortex and non-vortex electron states, and the DDCS for wide field electron plane waves under minimal assumptions regarding the magnitudes of electron velocity and energy exchange. By exploiting a quantum mechanical treatment that accounts explicitly for the transverse degrees of freedom of the probing electron wave functions, we have showcased the ability to retrieve information about the optical near-field and electromagnetic response of nanophotonic targets using inelastic scattering of phase-shaped free electrons following energy-momentum post-selection. A numerical procedure for evaluating derived observables is presented that allows for flexibility regarding particle number, size, geometry, and material composition. Example calculations for several prototypical plasmonic monomer and dimer systems are investigated to highlight the utility of our approach to analyze mode symmetries, local response field characteristics, chiral responses, and matter-wave diffraction phenomena. The general procedures outlined for constructing wide field plane wave and nondiffracting twisted and non-twisted electron beams with distinct transverse polarization and topological textures, in addition to the state- and energy-resolved observables, can be readily applied to many areas of atomic, molecular, and materials physics. In particular, we have drawn attention to an application of free electron qubits, whereby transitions between different OAM qubit states produce transition current densities with unique polarization and vector profiles, including analogs of optical polarization states and other more general forms of structured light. The theoretical framework presented can be extended to describe beam coherence in electron holography [205, 206] via a density matrix formalism [207], and utilized to explore the role of pure and mixed electron states in inelastic scattering and the concurrent transfer of quantum information in the form of quantized energy and OAM [182, 184, 185, 208]. Furthermore, the use of transversely phase-structured free electron states realizable in TEMs, STEMs, and ultrafast TEMs can lead to additional manifestations of unique electromagnetic fields [167, 168] and electron paraxial skyrmionic beams [169], all of which could play vital roles in the investigation of novel optically forbidden atomic, molecular, material, and topological excitations [142, 170, 209–211].

5.7 Acknowledgments

All work was supported by the U.S. Department of Energy (DOE), Office of Science, Office of Basic Energy Sciences (BES), Materials Sciences and Engineering Division under Award No. DOE BES DE-SC0022921.

5.8 Appendix

5.8.1 Vacuum Transition Vector Potentials and Electric Fields

The transition vector potentials and electric fields associated with each of the transition current densities in Sec. 5.3 are presented below. Specifically, the vacuum electric field

$$\begin{aligned}\mathbf{E}^0_{fi}(\mathbf{x},\omega) &= \frac{ic}{\omega}\left[\left(\frac{\omega}{c}\right)^2\overleftrightarrow{\mathbf{I}} + \nabla\nabla\right]\cdot\mathbf{A}^0_{fi}(\mathbf{x},\omega)\\ &= \frac{i}{\omega}\int d\mathbf{x}'\left[\left(\frac{\omega}{c}\right)^2\overleftrightarrow{\mathbf{I}} + \nabla\nabla\right]\frac{e^{i(\omega/c)|\mathbf{x}-\mathbf{x}'|}}{|\mathbf{x}-\mathbf{x}'|}\left(\frac{L}{v_i}\right)\mathbf{J}_{fi}(\mathbf{x}')\\ &= -4\pi i\omega\int d\mathbf{x}'\,\overleftrightarrow{\mathbf{G}}^0(\mathbf{x},\mathbf{x}',\omega)\cdot\left(\frac{L}{v_i}\right)\mathbf{J}_{fi}(\mathbf{x}')\end{aligned} \tag{5.47}$$

plays an important role in the observable EEL and EEG processes and depends upon the vector potential

$$\mathbf{A}^0_{fi}(\mathbf{x},\omega) = \frac{1}{c}\int d\mathbf{x}'\,\frac{e^{i(\omega/c)|\mathbf{x}-\mathbf{x}'|}}{|\mathbf{x}-\mathbf{x}'|}\left(\frac{L}{v_i}\right)\mathbf{J}_{fi}(\mathbf{x}') \tag{5.48}$$

presented here in the Lorenz gauge. Beginning with the transition current density in Eq. (5.18) associated with the transition between single plane wave states $\psi_{\mathbf{k}_i}(x,y,z)$ and $\psi_{\mathbf{k}_f}(x,y,z)$ where $\mathbf{k}_i$ and $\mathbf{k}_f$ are arbitrary wave vectors, the vacuum vector potential

$$\mathbf{A}^0_{\mathbf{k}_f\mathbf{k}_i}(\mathbf{x},\omega) = \frac{2\pi e\hbar}{mcv_iL^2}\frac{e^{i\mathbf{q}\cdot\mathbf{x}}}{(\omega/c)^2 - q^2}\mathbf{Q} \tag{5.49}$$

and electric field

$$\mathbf{E}^0_{\mathbf{k}_f\mathbf{k}_i}(\mathbf{x},\omega) = \frac{2\pi ie\gamma_i}{k_iL^2\omega}\frac{e^{i\mathbf{q}\cdot\mathbf{x}}}{(\omega/c)^2 - q^2}\left[\left(\frac{\omega}{c}\right)^2\overleftrightarrow{\mathbf{I}} - \mathbf{qq}\right]\cdot\mathbf{Q} \tag{5.50}$$

are readily obtained upon using the integral identity $\int d\mathbf{x}' e^{i(\omega/c)|\mathbf{x}-\mathbf{x}'|}e^{\mp i\mathbf{q}\cdot\mathbf{x}'}/|\mathbf{x}-\mathbf{x}'| = -4\pi e^{\mp i\mathbf{q}\cdot\mathbf{x}}/[(\omega/c)^2 - q^2]$.

The vacuum transition vector potential sourced by the superposition plane wave state transition current density in Eq. (5.19) takes the form

$$\begin{aligned}\mathbf{A}^{\chi 0}_{k'_\parallel,k_xk_y}(\mathbf{x},\omega) = \frac{2\pi e\hbar}{\sqrt{2}mcv_iL^2}e^{iq_\parallel z}\Bigg[&\frac{k_xe^{ik_xx}}{(\omega/c)^2 - k_x^2 - q_\parallel^2}\hat{\mathbf{x}} + \frac{k_ye^{i\chi}e^{ik_yy}}{(\omega/c)^2 - k_y^2 - q_\parallel^2}\hat{\mathbf{y}}\\ &+ Q_\parallel\left(\frac{e^{ik_xx}}{(\omega/c)^2 - k_x^2 - q_\parallel^2} + \frac{e^{i\chi}e^{ik_yy}}{(\omega/c)^2 - k_y^2 - q_\parallel^2}\right)\hat{\mathbf{z}}\Bigg]\end{aligned} \tag{5.51}$$

for the superposition state $\psi^\chi_{k_xk_y}(x,y,z) = (1/\sqrt{2L})\left[\Psi_{k_x}(x,y) + \Psi_{k_y}(x,y)e^{i\chi}\right]e^{ik_\parallel z}$ introduced in Sec. 5.2, transitioning to the final pin hole state $\psi_{k'_\parallel}(x,y,z) = L^{-3/2}e^{ik'_\parallel z}$ oriented along the TEM ($\hat{\mathbf{z}}$) axis. Associated

with this vector potential is the superposition plane wave state transition electric field

$$\mathbf{E}^{\chi 0}_{k'_\parallel,k_xk_y}(\mathbf{x},\omega)=\frac{-2\pi ie\hbar}{\sqrt{2}m\omega L^2v_i}\Big[\frac{k_x^2+Q_\parallel q_\parallel-(\frac{\omega}{c})^2}{k_x^2+q_\parallel^2-(\frac{\omega}{c})^2}k_xe^{ik_xx}\hat{\mathbf{x}}+\frac{k_y^2+Q_\parallel q_\parallel-(\frac{\omega}{c})^2}{k_y^2+q_\parallel^2-(\frac{\omega}{c})^2}k_ye^{ik_yy}e^{i\chi}\hat{\mathbf{y}}$$
$$+\Big(\frac{k_x^2q_\parallel+Q_\parallel q_\parallel^2-Q_\parallel(\frac{\omega}{c})^2}{k_x^2+q_\parallel^2-(\frac{\omega}{c})^2}e^{ik_xx}+\frac{k_y^2q_\parallel+Q_\parallel q_\parallel^2-Q_\parallel(\frac{\omega}{c})^2}{k_y^2+q_\parallel^2-(\frac{\omega}{c})^2}e^{ik_yy}e^{i\chi}\Big)\hat{\mathbf{z}}\Big]e^{iq_\parallel z}, \tag{5.52}$$

where $\mathbf{Q}=\mathbf{k}_i+\mathbf{k}_f$ and $\mathbf{q}=\mathbf{k}_i-\mathbf{k}_f$ are the same total and recoil wave vectors defined previously.

In the case of focused beams, more specifically in the small beam-width limit, we present only the vacuum transition fields involving one unit of OAM exchange between initial and final electron scattering states. The narrow beam limit, whereby the transverse electron wave function reduces to the transverse delta function [68], is adopted in all expressions. The transition vector potential and electric field associated with the HG transition current density in Eq. (5.23) describing the scattering from $\psi_{10}(x,y,z)$ to $\psi_{00}(x,y,z)$ is

$$\mathbf{A}^0_{00,10}(\mathbf{x},\omega)=-\frac{2ie\hbar}{mv_icw_0}\Big[\mathrm{K}_0\Big(\frac{q_\parallel\Delta R_0}{\gamma_i}\Big)\hat{\mathbf{x}}+i\frac{q_\parallel Q_\parallel w_0^2}{4\gamma_i}\frac{\Delta x}{\Delta R_0}\mathrm{K}_1\Big(\frac{q_\parallel\Delta R_0}{\gamma_i}\Big)\hat{\mathbf{z}}\Big]e^{iq_\parallel z}, \tag{5.53}$$

and

$$\mathbf{E}^0_{00,10}(\mathbf{x},\omega)=\frac{2\hbar e}{mw_0\omega v_i}\Big[\frac{\omega^2}{c^2}\overleftrightarrow{\mathbf{I}}+\nabla\nabla\Big]\cdot\Big[\mathrm{K}_0\Big(\frac{q_\parallel\Delta R_0}{\gamma_i}\Big)\hat{\mathbf{x}}+i\frac{q_\parallel Q_\parallel w_0^2}{4\gamma_i}\frac{\Delta x}{\Delta R_0}\mathrm{K}_1\Big(\frac{q_\parallel\Delta R_0}{\gamma_i}\Big)\hat{\mathbf{z}}\Big]e^{iq_\parallel z}$$
$$=\frac{\hbar e}{2mw_0\omega v_i}\Big\{\Big(\Big[\frac{4\omega^2}{c^2}+\frac{q_\parallel^2}{\gamma_i^2}(4+q_\parallel Q_\parallel w_0^2)\frac{\Delta x^2}{\Delta R_0^2}\Big]\mathrm{K}_0\Big(\frac{q_\parallel\Delta R_0}{\gamma_i}\Big)+\frac{q_\parallel}{\gamma_i}(4+q_\parallel Q_\parallel w_0^2)\frac{(\Delta x^2-\Delta y^2)}{\Delta R_0^3}\mathrm{K}_1\Big(\frac{q_\parallel\Delta R_0}{\gamma_i}\Big)\Big)\hat{\mathbf{x}}$$
$$+\frac{q_\parallel^2}{\gamma_i^2}(4+q_\parallel Q_\parallel w_0^2)\frac{\Delta x\Delta y}{\Delta R_0^2}\mathrm{K}_2\Big(\frac{q_\parallel\Delta R_0}{\gamma_i}\Big)\hat{\mathbf{y}}+\frac{i}{\gamma_i}\frac{\Delta x}{\Delta R_0}\Big[q_\parallel Q_\parallel w_0^2\frac{\omega^2}{c^2}-q_\parallel^2(1+q_\parallel Q_\parallel w_0^2)\Big]\mathrm{K}_1\Big(\frac{q_\parallel\Delta R_0}{\gamma_i}\Big)\hat{\mathbf{z}}\Big\}e^{iq_\parallel z}, \tag{5.54}$$

where $\Delta R_0=|\mathbf{R}-\mathbf{R}_0|$ and $\Delta x=|x-x_0|$ and $\Delta y=|y-y_0|$. By symmetry, scattering from HG $\psi_{01}(x,y,z)$ to $\psi_{00}(x,y,z)$ can be obtained from Eqs. (5.53) and by (5.54) interchanging $\hat{\mathbf{x}}$ with $\hat{\mathbf{y}}$, resulting in $\mathbf{A}^0_{00,01}(\mathbf{x},\omega)$ and $\mathbf{E}^0_{00,01}(\mathbf{x},\omega)$. If the transverse state does not change in the scattering process, as is the case in the conventional EEL signal, the vacuum vector potential and electric field associated with the current density in Eq. (5.24) where $n'=n=0$ and $m'=m=0$ become

$$\mathbf{A}^0_{00,00}(\mathbf{x},\omega)=\Big(\frac{\hbar e}{mv_ic}\Big)Q_\parallel\mathrm{K}_0\Big(\frac{q_\parallel\Delta R_0}{\gamma_i}\Big)\hat{\mathbf{z}}\,e^{iq_\parallel z} \tag{5.55}$$

and

$$\mathbf{E}^0_{00,00}(\mathbf{x},\omega)=\frac{\hbar e}{\omega mv_i}Q_\parallel\left[\frac{q_\parallel^2}{\gamma_i\Delta R_0}\mathrm{K}_1\Big(\frac{q_\parallel\Delta R_0}{\gamma}\Big)\Big(\Delta x\hat{\mathbf{x}}+\Delta y\hat{\mathbf{y}}\Big)+i\Big(\frac{\omega^2}{c^2}-q_\parallel^2\Big)\mathrm{K}_0\Big(\frac{q_\parallel\Delta R_0}{\gamma}\Big)\hat{\mathbf{z}}\right]e^{iq_\parallel z}. \tag{5.56}$$

The latter is the well known classical field of a uniformly moving point electron [68, 80] in the nonrecoil approximation where $q_\parallel=\omega/v_i$ and $Q_\parallel=2k_\parallel^i$.

Transitions between LG states $\psi_{\ell p}(\rho,\phi,z)$ and $\psi_{\ell' p'}(\rho,\phi,z)$ involving one unit of OAM can be derived

from the above HG transitions by linear combination. Specifically,

$$\mathbf{A}^0_{\ell'=0,p'=0,\ell=\pm1,p=0}(\rho,\phi,z,\omega)=\frac{1}{\sqrt{2}}\big[\mathbf{A}^0_{00,10}(\mathbf{x},\omega)\pm i\mathbf{A}^0_{00,01}(\mathbf{x},\omega)\big] \tag{5.57}$$

and

$$\mathbf{E}^0_{\ell'=0,p'=0,\ell=\pm1,p=0}(\rho,\phi,z,\omega)=\frac{1}{\sqrt{2}}\big[\mathbf{E}^0_{00,10}(\mathbf{x},\omega)\pm i\mathbf{E}^0_{00,01}(\mathbf{x},\omega)\big]. \tag{5.58}$$

All electric fields introduced in the Appendix are coded within the e-DDA and can be used to calculate the presented EEL observables in both wide field and focused beam limits.

5.8.2 Observables Under Interchange of Initial and Final States

The EEL rate w_{fi} is proportional to $\int d\mathbf{x}\,d\mathbf{x}'\mathbf{J}^*_{fi}(\mathbf{x})\cdot\overleftrightarrow{\mathbf{G}}(\mathbf{x},\mathbf{x}',\omega)\cdot\mathbf{J}_{fi}(\mathbf{x}')$. By interchanging the 3D coordinates $\mathbf{x}$ and $\mathbf{x}'$, and invoking reciprocity, i.e., $G_{\alpha\beta}(\mathbf{x},\mathbf{x}',\omega)=G_{\beta\alpha}(\mathbf{x}',\mathbf{x},\omega)$,

$$\begin{aligned}
\int d\mathbf{x}\,d\mathbf{x}'\big[\mathbf{J}_{fi}(\mathbf{R})e^{iq_\parallel z}\big]^*_\alpha G_{\alpha\beta}(\mathbf{x},\mathbf{x}',\omega)\big[\mathbf{J}_{fi}(\mathbf{R}')e^{iq_\parallel z'}\big]_\beta &= \int d\mathbf{x}\,d\mathbf{x}'\big[\mathbf{J}_{fi}(\mathbf{R})\big]^*_\alpha G_{\alpha\beta}(\mathbf{x},\mathbf{x}',\omega)\big[\mathbf{J}_{fi}(\mathbf{R}')\big]_\beta e^{-iq_\parallel(z-z')}\\
&= \int d\mathbf{x}\,d\mathbf{x}'\big[\mathbf{J}_{if}(\mathbf{R})\big]_\alpha G_{\alpha\beta}(\mathbf{x},\mathbf{x}',\omega)\big[\mathbf{J}_{if}(\mathbf{R}')\big]^*_\beta e^{-iq_\parallel(z-z')}\\
&= \int d\mathbf{x}\,d\mathbf{x}'\big[\mathbf{J}_{if}(\mathbf{R}')\big]^*_\beta G_{\beta\alpha}(\mathbf{x}',\mathbf{x},\omega)\big[\mathbf{J}_{if}(\mathbf{R})\big]_\alpha e^{-iq_\parallel(z-z')}\\
&= \int d\mathbf{x}\,d\mathbf{x}'\big[\mathbf{J}_{if}(\mathbf{R})\big]^*_\alpha G_{\alpha\beta}(\mathbf{x},\mathbf{x}',\omega)\big[\mathbf{J}_{if}(\mathbf{R}')\big]_\beta e^{-iq_\parallel(z'-z)}\\
&= \int d\mathbf{x}\,d\mathbf{x}'\big[\mathbf{J}_{if}(\mathbf{R})e^{i(-q_\parallel)z}\big]^*_\alpha G_{\alpha\beta}(\mathbf{x},\mathbf{x}',\omega)\big[\mathbf{J}_{if}(\mathbf{R}')e^{i(-q_\parallel)z'}\big]_\beta,
\end{aligned} \tag{5.59}$$

where $\alpha,\beta=x,y,z$ and Einstein summation notation has been used. Eq. (5.59) can be equivalently expressed as $w_{fi}(q_\parallel)=w_{if}(-q_\parallel)$ provided $G_{\alpha\beta}(\mathbf{x},\mathbf{x}',\omega)=G_{\beta\alpha}(\mathbf{x}',\mathbf{x},\omega)$. Said differently, interchanging the initial and final transverse states together with changing the sign of the recoil momentum wave vector $q_\parallel$ leaves the EEL observable invariant in a reciprocal medium. In the case of an isolated dipolar target at position $\mathbf{x}_d$ characterized by frequency-dependent polarizability $\overleftrightarrow{\boldsymbol{\alpha}}(\omega)$, $\overleftrightarrow{\mathbf{G}}(\mathbf{x},\mathbf{x}',\omega)$ satisfies the reciprocity condition when the polarizability tensor is complex symmetric, i.e., when $\overleftrightarrow{\boldsymbol{\alpha}}(\omega)=\overleftrightarrow{\boldsymbol{\alpha}}^T(\omega)$.

5.8.3 Laser-Stimulated Coherent States of the Target

Under the assumption that the stimulating laser field couples to a single target mode (labeled ℓ), which is driven into the coherent state $|\alpha_\ell\rangle$, the rate at which the probing electron gains energy as the target transitions to the sum of final Fock states $|n'_\ell\rangle$ is

$$\begin{aligned}
w^{\text{gain}}_{fi} &= \frac{2\pi}{\hbar c^2}\sum_{n'_\ell}\Big|\sum_\nu\int d\mathbf{x}\,\mathbf{J}_{fi}(\mathbf{x},t)\cdot\langle n'_\ell|\mathbf{A}^{(+)}_\nu(\mathbf{x})a_\nu e^{-i\omega_\nu t}|\alpha_\ell\rangle\Big|^2\delta(E_f-E_i)\\
&= \frac{2\pi}{\hbar c^2}\sum_{n'_\ell}\Big|\alpha_\ell\langle n'_\ell|\alpha_\ell\rangle\int d\mathbf{x}\,\mathbf{A}^{(+)}_\ell(\mathbf{x})\cdot\mathbf{J}_{fi}(\mathbf{x})\Big|^2\delta(E_f-E_i).
\end{aligned} \tag{5.60}$$

Coherent states can be written as $|\alpha\rangle = e^{-|\alpha|^2/2}\sum_{n=0}^{\infty}(\alpha^n/\sqrt{n!})|n\rangle$, where $|n\rangle = [(a^\dagger)^n/\sqrt{n!}]|0\rangle$. When expressed in terms of the electric field $\mathbf{E}_\ell^{(\pm)}(\mathbf{x}) = \pm(i\omega_\ell)/c\,\mathbf{A}_\ell^{(\pm)}(\mathbf{x})$ together with $\left|\langle n'_\ell|\alpha_\ell\rangle\right|^2 = (|\alpha_\ell|^{2n'_\ell}/n'_\ell!)e^{-|\alpha_\ell|^2}$, Eq. (5.60) can be cast as

$$\begin{aligned} w_{fi}^{\text{gain}} &= 2\pi\left(\frac{|\alpha_\ell|}{\hbar\omega_\ell}\right)^2\left(\sum_{n'_\ell}\frac{|\alpha_\ell|^{2n'_\ell}}{n'_\ell!}\right)e^{-|\alpha_\ell|^2}\left|\int d\mathbf{x}\,\mathbf{E}_\ell^{(+)}(\mathbf{x})\cdot\mathbf{J}_{fi}(\mathbf{x})\right|^2\delta([E_f-E_i]/\hbar) \\ &= 2\pi\left(\frac{|\alpha_\ell|}{\hbar\omega_\ell}\right)^2\left|\int d\mathbf{x}\,\mathbf{E}_\ell^{(+)}(\mathbf{x})\cdot\mathbf{J}_{fi}(\mathbf{x})\right|^2\delta([E_f-E_i]/\hbar). \end{aligned} \tag{5.61}$$

Bibliography

[1] Kevin C. Smith, Austin G. Nixon, and David J. Masiello. Strongly coupled photonic molecules as doubly-coupled oscillators, 2025.

[2] Marc R. Bourgeois, Feng Pan, C. Praise Anyanwu, Austin G. Nixon, Elliot K. Beutler, Jennifer A. Dionne, Randall H. Goldsmith, and David J. Masiello. Spectroscopy in nanoscopic cavities: Models and recent experiments. *Annu. Rev. Phys. Chem.*, 75:509–534, 2024.

[3] Austin G. Nixon, Matthieu Chalifour, Marc R. Bourgeois, Michael Sanchez, and David J. Masiello. Inelastic scattering of transversely structured free electrons from nanophotonic targets: Theory and computation. *Phys. Rev. A*, 109:043502, Apr 2024.

[4] Marc R. Bourgeois, Austin G. Nixon, Matthieu Chalifour, and David J. Masiello. Optical polarization analogs in inelastic free-electron scattering. *Sci. Adv.*, 9(51):eadj6038, 2023.

[5] Marc R. Bourgeois, Austin G. Nixon, Matthieu Chalifour, Elliot K. Beutler, and David J. Masiello. Polarization-resolved electron energy gain nanospectroscopy with phase-structured electron beams. *Nano Lett.*, 22(17):7158–7165, 2022.

[6] Feng Pan, Kristoffer Karlsson, Austin G. Nixon, Levi T. Hogan, Jonathan M. Ward, Kevin C. Smith, David J. Masiello, Síle Nic Chormaic, and Randall H. Goldsmith. Active control of Plasmonic–Photonic interactions in a microbubble cavity. *J. Phys. Chem. C*, 126(48):20470–20479, December 2022.

[7] Parivash Moradifar, Austin G. Nixon, Tiva Sharifi, Tim Brandt van Driel, Pulickel Ajayan, David J. Masiello, and Nasim Alem. Nanoscale mapping and Defect-Assisted manipulation of surface plasmon resonances in 2D Bi2Te3/Sb2Te3 In-Plane heterostructures. *Adv. Opt. Mater.*, 10(10):2101968, May 2022.

[8] Yueying Wu, Zhongwei Hu, Xiang-Tian Kong, Juan Carlos Idrobo, Austin G. Nixon, Philip D. Rack, David J. Masiello, and Jon P. Camden. Infrared plasmonics: Stem-eels characterization of fabry-pérot resonance damping in gold nanowires. *Phys. Rev. B*, 101:085409, Feb 2020.

[9] Grace Pakeltis, Zhongwei Hu, Austin G. Nixon, Eva Mutunga, C. Praise Anyanwu, Claire A. West, Juan Carlos Idrobo, Harald Plank, David J. Masiello, Jason D. Fowlkes, and Philip D. Rack. Focused

electron beam induced deposition synthesis of 3D photonic and magnetic nanoresonators. *ACS Appl. Nano Mater.*, 2(12):8075–8082, December 2019.

[10] Louis de Broglie. *Recherches sur la théorie des quanta (Research on the Theory of Quanta).* PhD thesis, University of Paris, 1921.

[11] C. Davisson and L. H. Germer. Diffraction of electrons by a crystal of nickel. *Phys. Rev.*, 30:705–740, Dec 1927.

[12] G. P. Thomson and A. Reid. Diffraction of cathode rays by a thin film. *Nature*, 119(3007):890–890, June 1927.

[13] Max Planck. Ueber das gesetz der energieverteilung im normalspectrum. *Ann. Phys.*, 309(3):553–563, January 1901.

[14] Albert Einstein. Über einen die erzeugung und verwandlung des lichtes betreffenden heuristischen gesichtspunkt. *Ann. Phys.*, 322(6):132–148, January 1905.

[15] Arthur H. Compton. A quantum theory of the scattering of x-rays by light elements. *Phys. Rev.*, 21:483–502, May 1923.

[16] Thomas Young. The bakerian lecture. on the theory of light and colours. *Philos. T. R. Soc. Lond.*, 92:12–48, January 1802.

[17] Erwin Schrödinger. Quantisierung als eigenwertproblem. *Ann. Phys.*, 384(4):361–376, January 1926.

[18] Paul A. M. Dirac. The quantum theory of the emission and absorption of radiation. *P. Roy. Soc. A-Math Phy.*, 114(767):243–265, 1927.

[19] Paul A. M. Dirac. The quantum theory of the electron. *P. Roy. Soc. A-Math Phy.*, 117(778):610–624, 1928.

[20] Hans Bethe. Zur theorie des durchgangs schneller korpuskularstrahlen durch materie. *Ann. Phys. (Leipzig)*, 397(3):325–400, January 1930.

[21] R. Colella, A. W. Overhauser, and S. A. Werner. Observation of gravitationally induced quantum interference. *Phys. Rev. Lett.*, 34:1472–1474, Jun 1975.

[22] Anton Zeilinger, Roland Gähler, C. G. Shull, Wolfgang Treimer, and Walter Mampe. Single- and double-slit diffraction of neutrons. *Rev. Mod. Phys.*, 60:1067–1073, Oct 1988.

[23] O. Carnal and J. Mlynek. Young's double-slit experiment with atoms: A simple atom interferometer. *Phys. Rev. Lett.*, 66:2689–2692, May 1991.

[24] Markus Arndt, Olaf Nairz, Julian Vos-Andreae, Claudia Keller, Gerbrand van der Zouw, and Anton Zeilinger. Wave–particle duality of C_{60} molecules. *Nature*, 401(6754):680–682, October 1999.

[25] James Clerk Maxwell. A dynamical theory of the electromagnetic field. *Philos. T. R. Soc. Lond.*, 155:459–512, January 1865.

[26] K. Y. Bliokh, I. P. Ivanov, G. Guzzinati, L. Clark, R. Van Boxem, A. Béché, R. Juchtmans, M. A. Alonso, P. Schattschneider, F. Nori, and J. Verbeeck. Theory and applications of free-electron vortex states. *Phys. Rep.*, 690:1–70, May 2017.

[27] Abbe Hon. The relation of aperture and power in the microscope (continued). *Journal of the Royal Microscopical Society*, 2(4):460–473, August 1882.

[28] Max Knoll and Ernst Ruska. Beitrag zur geometrischen elektronenoptik. I. *Ann. Phys.*, 404(5):607–640, January 1932.

[29] Max Knoll and Ernst Ruska. Beitrag zur geometrischen elektronenoptik. II. *Ann. Phys.*, 404(6):641–661, January 1932.

[30] Ernst Ruska. The development of the electron microscope and of electron microscopy. *Rev. Mod. Phys.*, 59:627–638, Jul 1987.

[31] Cecil E. Hall. Visualization of individual macromolecules with the electron microscope. *Proc. Natl. Acad. Sci. U.S.A.*, 42(11):801–806, November 1956.

[32] Thomas E. Weirich, Reiner Ramlau, Arndt Simon, Sven Hovmöller, and Xiaodong Zou. A crystal structure determined with 0.02 Å accuracy by electron microscopy. *Nature*, 382(6587):144–146, July 1996.

[33] Zhen Chen, Yi Jiang, Yu-Tsun Shao, Megan E. Holtz, Michal Odstrčil, Manuel Guizar-Sicairos, Isabelle Hanke, Steffen Ganschow, Darrell G. Schlom, and David A. Muller. Electron ptychography achieves atomic-resolution limits set by lattice vibrations. *Science*, 372(6544):826–831, May 2021.

[34] Kai Siegbahn. Electron spectroscopy for atoms, molecules, and condensed matter. *Rev. Mod. Phys.*, 54:709–728, Jul 1982.

[35] Kai Siegbahn and Kay Edvarson. β-Ray spectroscopy in the precision range of $1 : 10^5$. *Nucl. Phys.*, 1(8):137–159, January 1956.

[36] Hans Bethe. Bremsformel für elektronen relativistischer geschwindigkeit. *Z.Phys.*, 76(5):293–299, May 1932.

[37] David Bohm and David Pines. A collective description of electron interactions. I. magnetic interactions. *Phys. Rev.*, 82:625–634, Jun 1951.

[38] David Pines and David Bohm. A collective description of electron interactions: II. collective vs individual particle aspects of the interactions. *Phys. Rev.*, 85:338–353, Jan 1952.

[39] David Bohm and David Pines. A collective description of electron interactions: III. coulomb interactions in a degenerate electron gas. *Phys. Rev.*, 92:609–625, Nov 1953.

[40] Richard A. Beth. Mechanical detection and measurement of the angular momentum of light. *Phys. Rev.*, 50:115–125, Jul 1936.

[41] L. Allen, M. W. Beijersbergen, R. J. C. Spreeuw, and J. P. Woerdman. Orbital angular momentum of light and the transformation of Laguerre-Gaussian laser modes. *Phys. Rev. A*, 45:8185–8189, Jun 1992.

[42] N. B. Simpson, K. Dholakia, L. Allen, and M. J. Padgett. Mechanical equivalence of spin and orbital angular momentum of light: an optical spanner. *Opt. Lett.*, 22(1):52–54, January 1997.

[43] Konstantin Yu. Bliokh, Yury P. Bliokh, Sergey Savel'ev, and Franco Nori. Semiclassical dynamics of electron wave packet states with phase vortices. *Phys. Rev. Lett.*, 99:190404, Nov 2007.

[44] Johan Verbeeck, He Tian, and Peter Schattschneider. Production and application of electron vortex beams. *Nature*, 467(7313):301–304, 2010.

[45] Masaya Uchida and Akira Tonomura. Generation of electron beams carrying orbital angular momentum. *Nature*, 464(7289):737–739, 2010.

[46] Benjamin J. McMorran, Amit Agrawal, Ian M. Anderson, Andrew A. Herzing, Henri J. Lezec, Jabez J. McClelland, and John Unguris. Electron vortex beams with high quanta of orbital angular momentum. *Science*, 331(6014):192–195, 2011.

[47] Amir H. Tavabi, Paolo Rosi, Enzo Rotunno, Alberto Roncaglia, Luca Belsito, Stefano Frabboni, Giulio Pozzi, Gian Carlo Gazzadi, Peng-Han Lu, Robert Nijland, Moumita Ghosh, Peter Tiemeijer, Ebrahim Karimi, Rafal E. Dunin-Borkowski, and Vincenzo Grillo. Experimental demonstration of an electrostatic orbital angular momentum sorter for electron beams. *Phys. Rev. Lett.*, 126:094802, Mar 2021.

[48] Hugo Lourenço-Martins, Davy Gérard, and Mathieu Kociak. Optical polarization analogue in free electron beams. *Nat. Phys.*, 17(5):598–603, 2021.

[49] Giulio Guzzinati, Armand Béché, Hugo Lourenço-Martins, Jérôme Martin, Mathieu Kociak, and Jo Verbeeck. Probing the symmetry of the potential of localized surface plasmon resonances with phase-shaped electron beams. *Nat. Commun.*, 8(1):1–8, 2017.

[50] J.J. Sakurai and Jim Napolitano. *Modern Quantum Mechanics Second Edition.* Addison-Wesley., 2011.

[51] J.J. Sakurai. *Advanced Quantum Mechanics.* Pearson Education, Inc, 1967.

[52] John David Jackson. *Classical Electrodynamics*. Wiley, 1999.

[53] Claude Cohen-Tannoudji, Jacques Dupont-Roc, and Gilbert Grynberg. *Photons and Atoms: Introduction to Quantum Electrodynamics*. Wiley, Weinheim, Germany, 1997.

[54] P. Schattschneider, S. Rubino, C. Hébert, J. Rusz, J. Kuneš, P. Novák, E. Carlino, M. Fabrizioli, G. Panaccione, and G. Rossi. Detection of magnetic circular dichroism using a transmission electron microscope. *Nature*, 441(7092):486–488, May 2006.

[55] M. Wagner. *Unitary Transformations in Solid State Physics*. North-Holland Physics Publishing, Amsterdam, The Netherlands, 1986.

[56] S. M. Lloyd, M. Babiker, G. Thirunavukkarasu, and J. Yuan. Electron vortices: Beams with orbital angular momentum. *Rev. Mod. Phys.*, 89:035004, Aug 2017.

[57] Tomáš Neuman, Pablo Alonso-González, Aitzol Garcia-Etxarri, Martin Schnell, Rainer Hillenbrand, and Javier Aizpurua. Mapping the near fields of plasmonic nanoantennas by scattering-type scanning near-field optical microscopy. *Laser Photonics Rev.*, 9(6):637–649, 2015.

[58] Thiago L. Vasconcelos, Bráulio S. Archanjo, Benjamin Fragneaud, Bruno S. Oliveira, Juha Riikonen, Changfeng Li, Douglas S. Ribeiro, Cassiano Rabelo, Wagner N. Rodrigues, Ado Jorio, Carlos A. Achete, and Luiz Gustavo Cançado. Tuning localized surface plasmon resonance in scanning Near-Field optical microscopy probes. *ACS Nano*, 9(6):6297–6304, June 2015.

[59] Florian Schertz, Marcus Schmelzeisen, Maximilian Kreiter, Hans-Joachim Elmers, and Gerd Schönhense. Field emission of electrons generated by the near field of strongly coupled plasmons. *Phys. Rev. Lett.*, 108(23):237602, 2012.

[60] Andrej Grubisic, Emilie Ringe, Claire M. Cobley, Younan Xia, Laurence D. Marks, Richard P. Van Duyne, and David J. Nesbitt. Plasmonic near-electric field enhancement effects in ultrafast photoelectron emission: correlated spatial and laser polarization microscopy studies of individual ag nanocubes. *Nano Lett.*, 12(9):4823–4829, 2012.

[61] Andrej Grubisic, Volker Schweikhard, Thomas A. Baker, and David J. Nesbitt. Coherent multiphoton photoelectron emission from single au nanorods: the critical role of plasmonic electric near-field enhancement. *ACS Nano*, 7(1):87–99, 2013.

[62] Maciej Dąbrowski, Yanan Dai, and Hrvoje Petek. Ultrafast microscopy: Imaging light with photoelectrons on the nano–femto scale. *J. Phys. Chem. Lett.*, 8(18):4446–4455, 2017.

[63] Yanan Dai, Zhikang Zhou, Atreyie Ghosh, Roger S.K. Mong, Atsushi Kubo, Chen-Bin Huang, and Hrvoje Petek. Plasmonic topological quasiparticle on the nanometre and femtosecond scales. *Nature*, 588(7839):616–619, 2020.

[64] Xinzhong Chen, Debo Hu, Ryan Mescall, Guanjun You, D. N. Basov, Qing Dai, and Mengkun Liu. Modern Scattering-Type scanning Near-Field optical microscopy for advanced material research. *Adv. Mater.*, 31(24):1804774, June 2019.

[65] Maciej Dąbrowski, Yanan Dai, and Hrvoje Petek. Ultrafast photoemission electron microscopy: Imaging plasmons in space and time. *Chem. Rev.*, 120(13):6247–6287, July 2020.

[66] P. E. Batson. Surface plasmon coupling in clusters of small spheres. *Phys. Rev. Lett.*, 49(13):936, 1982.

[67] P. E. Batson. Inelastic scattering of fast electrons in clusters of small spheres. *Surf. Sci.*, 156:720–734, 1985.

[68] F. J. García de Abajo. Optical excitations in electron microscopy. *Rev. Mod. Phys.*, 82(1):209, 2010.

[69] Yueying Wu, Guoliang Li, and Jon P. Camden. Probing nanoparticle plasmons with electron energy loss spectroscopy. *Chem. Rev.*, 118(6):2994–3031, 2018.

[70] Jaysen Nelayah, Mathieu Kociak, Odile Stéphan, F. J. García de Abajo, Marcel Tencé, Luc Henrard, Dario Taverna, Isabel Pastoriza-Santos, Luis M. Liz-Marzán, and Christian Colliex. Mapping surface plasmons on a single metallic nanoparticle. *Nat. Phys.*, 3(5):348–353, 2007.

[71] Charles Cherqui, Niket Thakkar, Guoliang Li, Jon P. Camden, and David J. Masiello. Characterizing localized surface plasmons using electron energy-loss spectroscopy. *Annu. Rev. Phys. Chem.*, 67:331–357, 2016.

[72] Christian Colliex, Mathieu Kociak, and Odile Stéphan. Electron energy loss spectroscopy imaging of surface plasmons at the nanometer scale. *Ultramicroscopy*, 162:A1–A24, 2016.

[73] Andrea Konečná, Tomáš Neuman, Javier Aizpurua, and Rainer Hillenbrand. Surface-enhanced molecular electron energy loss spectroscopy. *ACS Nano*, 12(5):4775–4786, 2018.

[74] Andrew B. Yankovich, Battulga Munkhbat, Denis G. Baranov, Jorge Cuadra, Erik Olsén, Hugo Lourenço-Martins, Luiz H.G. Tizei, Mathieu Kociak, Eva Olsson, and Timur Shegai. Visualizing spatial variations of plasmon-exciton polaritons at the nanoscale using electron microscopy. *Nano Lett.*, 19(11):8171–8181, 2019.

[75] Marc R. Bourgeois, Elliot K. Beutler, Siamak Khorasani, Nicole Panek, and David J. Masiello. Nanometer-scale spatial and spectral mapping of exciton polaritons in structured plasmonic cavities. *Phys. Rev. Lett.*, 128(19):197401, 2022.

[76] H. Kohl and H. Rose. Theory of image formation by inelastically scattered electrons in the electron microscope. In Peter W Hawkes, editor, *Advances in Electronics and Electron Physics*, volume 65, pages 173–227. Academic Press, January 1985.

[77] Adam P. Hitchcock. Near edge electron energy loss spectroscopy: Comparison to X-ray absorption. *Jpn. J. Appl. Phys.*, 32(S2):176, January 1993.

[78] P. E. Batson. Symmetry-selected electron-energy-loss scattering in diamond. *Phys. Rev. Lett.*, 70:1822–1825, Mar 1993.

[79] J. Yuan and N. K. Menon. Magnetic linear dichroism in electron energy loss spectroscopy. *J. Appl. Phys.*, 81(8):5087–5089, April 1997.

[80] F. J. García de Abajo and M. Kociak. Probing the photonic local density of states with electron energy loss spectroscopy. *Phys. Rev. Lett.*, 100(10):106804, 2008.

[81] Ulrich Hohenester, Harald Ditlbacher, and Joachim R. Krenn. Electron-energy-loss spectra of plasmonic nanoparticles. *Phys. Rev. Lett.*, 103(10):106801, 2009.

[82] Anton Hörl, Andreas Trügler, and Ulrich Hohenester. Tomography of particle plasmon fields from electron energy loss spectroscopy. *Phys. Rev. Lett.*, 111(7):076801, 2013.

[83] Olivia Nicoletti, Francisco de La Peña, Rowan K. Leary, Daniel J. Holland, Caterina Ducati, and Paul A. Midgley. Three-dimensional imaging of localized surface plasmon resonances of metal nanoparticles. *Nature*, 502(7469):80–84, 2013.

[84] Anton Hörl, Andreas Trügler, and Ulrich Hohenester. Full three-dimensonal reconstruction of the dyadic green tensor from electron energy loss spectroscopy of plasmonic nanoparticles. *ACS Photonics*, 2(10):1429–1435, 2015.

[85] Anton Hörl, Georg Haberfehlner, Andreas Trügler, Franz-Philipp Schmidt, Ulrich Hohenester, and Gerald Kothleitner. Tomographic imaging of the photonic environment of plasmonic nanoparticles. *Nat. Commun.*, 8(1):1–7, 2017.

[86] Xiaoyan Li, Georg Haberfehlner, Ulrich Hohenester, Odile Stéphan, Gerald Kothleitner, and Mathieu Kociak. Three-dimensional vectorial imaging of surface phonon polaritons. *Science*, 371(6536):1364–1367, 2021.

[87] A. Asenjo-Garcia and F. J. García de Abajo. Dichroism in the interaction between vortex electron beams, plasmons, and molecules. *Phys. Rev. Lett.*, 113:066102, Aug 2014.

[88] Wei Cai, Ori Reinhardt, Ido Kaminer, and F. J. García de Abajo. Efficient orbital angular momentum transfer between plasmons and free electrons. *Phys. Rev. B*, 98(4):045424, 2018.

[89] Matteo Zanfrognini, Enzo Rotunno, Stefano Frabboni, Alicia Sit, Ebrahim Karimi, Ulrich Hohenester, and Vincenzo Grillo. Orbital angular momentum and energy loss characterization of plasmonic excitations in metallic nanostructures in TEM. *ACS Photonics*, 6(3):620–627, 2019.

[90] F. J. García de Abajo and M. Kociak. Electron energy-gain spectroscopy. *New J. Phys.*, 10(7):073035, 2008.

[91] Ana Asenjo-Garcia and F. J. García de Abajo. Plasmon electron energy-gain spectroscopy. *New J. Phys.*, 15(10):103021, 2013.

[92] Chenze Liu, Yueying Wu, Zhongwei Hu, Jacob A. Busche, Elliot K. Beutler, Nicholas P. Montoni, Thomas M. Moore, Gregory A. Magel, Jon P. Camden, David J. Masiello, Gerd Duscher, and Philip D. Rack. Continuous wave resonant photon stimulated electron energy-gain and electron energy-loss spectroscopy of individual plasmonic nanoparticles. *ACS Photonics*, 6(10):2499–2508, October 2019.

[93] Matthias Liebtrau, Murat Sivis, Armin Feist, Hugo Lourenço-Martins, Nicolas Pazos-Pérez, Ramon A. Alvarez-Puebla, F. J. García de Abajo, Albert Polman, and Claus Ropers. Spontaneous and stimulated electron–photon interactions in nanoscale plasmonic near fields. *Light-Sci. Appl.*, 10(1):1–14, 2021.

[94] P. Das, J. D. Blazit, M. Tencé, L. F. Zagonel, Y. Auad, Y. H. Lee, X. Y. Ling, A. Losquin, C. Colliex, O. Stéphan, F. J. García de Abajo, and M. Kociak. Stimulated electron energy loss and gain in an electron microscope without a pulsed electron gun. *Ultramicroscopy*, 203:44–51, August 2019.

[95] Robyn Collette, David A. Garfinkel, and Philip D. Rack. Nearfield excited state imaging of bonding and antibonding plasmon modes in nanorod dimers via stimulated electron energy gain spectroscopy. *J. Chem. Phys.*, 153(4):044711, 2020.

[96] Brett Barwick, David J. Flannigan, and Ahmed H. Zewail. Photon-induced near-field electron microscopy. *Nature*, 462(7275):902–906, 2009.

[97] F. J. García de Abajo, Ana Asenjo-Garcia, and Mathieu Kociak. Multiphoton absorption and emission by interaction of swift electrons with evanescent light fields. *Nano Lett.*, 10(5):1859–1863, 2010.

[98] Sang Tae Park, Milo Lin, and Ahmed H. Zewail. Photon-induced near-field electron microscopy (PINEM): theoretical and experimental. *New J. Phys.*, 12(12):123028, December 2010.

[99] Brett Barwick and Ahmed H. Zewail. Photonics and plasmonics in 4d ultrafast electron microscopy. *ACS Photonics*, 2(10):1391–1402, 2015.

[100] Kangpeng Wang, Raphael Dahan, Michael Shentcis, Yaron Kauffmann, Adi Ben Hayun, Ori Reinhardt, Shai Tsesses, and Ido Kaminer. Coherent interaction between free electrons and a photonic cavity. *Nature*, 582(7810):50–54, 2020.

[101] F. J. García de Abajo and Valerio Di Giulio. Optical excitations with electron beams: Challenges and opportunities. *ACS Photonics*, 8(4):945–974, April 2021.

[102] Vincenzo Grillo, Amir H. Tavabi, Federico Venturi, Hugo Larocque, Roberto Balboni, Gian Carlo Gazzadi, Stefano Frabboni, Peng-Han Lu, Erfan Mafakheri, Frédéric Bouchard, Rafal E. Dunin-Borkowski, Robert W. Boyd, Martin P. J. Lavery, Miles J. Padgett, and Ebrahim Karimi. Measuring the orbital angular momentum spectrum of an electron beam. *Nat. Commun.*, 8(1):15536, May 2017.

[103] Dolev Roitman, Roy Shiloh, Peng-Han Lu, Rafal E. Dunin-Borkowski, and Ady Arie. Shaping of electron beams using sculpted thin films. *ACS Photonics*, 8(12):3394–3405, 2021.

[104] Jo Verbeeck, Armand Béché, Knut Müller-Caspary, Giulio Guzzinati, Minh Anh Luong, and Martien Den Hertog. Demonstration of a 2×2 programmable phase plate for electrons. *Ultramicroscopy*, 190:58–65, 2018.

[105] Ran Li, Danqing Wang, Jun Guan, Weijia Wang, Xianyu Ao, George C. Schatz, Richard Schaller, and Teri W. Odom. Plasmon nanolasing with aluminum nanoparticle arrays. *J. Opt. Soc. Am. B*, 36(7):E104–E111, July 2019.

[106] Tyler R. Harvey, Jan-Wilke Henke, Ofer Kfir, Hugo Lourenco-Martins, Armin Feist, F. J. García de Abajo, and Claus Ropers. Probing chirality with inelastic electron-light scattering. *Nano Lett.*, 20(6):4377–4383, 2020.

[107] Bruce T. Draine and Piotr J. Flatau. Discrete-dipole approximation for scattering calculations. *J. Opt. Soc. Am. A*, 11(4):1491–1499, 1994.

[108] Agust Olafsson, Siamak Khorasani, Jacob A. Busche, Jose J. Araujo, Juan Carlos Idrobo, Daniel R. Gamelin, David J. Masiello, and Jon P. Camden. Imaging infrared plasmon hybridization in doped semiconductor nanocrystal dimers. *J. Phys. Chem. Lett.*, 12(42):10270–10276, 2021. PMID: 34652912.

[109] Steven C. Quillin, Charles Cherqui, Nicholas P. Montoni, Guoliang Li, Jon P. Camden, and David J. Masiello. Imaging plasmon hybridization in metal nanoparticle aggregates with electron energy-loss spectroscopy. *J. Phys. Chem. C*, 120(37):20852–20859, 2016.

[110] Xinghui Yin, Martin Schäferling, Bernd Metzger, and Harald Giessen. Interpreting chiral nanophotonic spectra: the plasmonic Born–Kuhn model. *Nano Lett.*, 13(12):6238–6243, 2013.

[111] Tong Fu, Tiankun Wang, Yuyan Chen, Yongkai Wang, Yu Qu, and Zhongyue Zhang. Chiral near-fields around chiral dolmen nanostructure. *J. Phys. D: Appl. Phys.*, 50(47):474004, 2017.

[112] Lauren A. Warning, Ali Rafiei Miandashti, Lauren A. McCarthy, Qingfeng Zhang, Christy F. Landes, and Stephan Link. Nanophotonic approaches for chirality sensing. *ACS Nano*, 15(10):15538–15566, 2021.

[113] Hui Zhang and A.O. Govorov. Giant circular dichroism of a molecule in a region of strong plasmon resonances between two neighboring gold nanocrystals. *Phys. Rev. B*, 87(7):075410, 2013.

[114] H. Boersch, J. Geiger, and W. Stickel. Interaction of 25-kev electrons with lattice vibrations in lif. experimental evidence for surface modes of lattice vibration. *Phys. Rev. Lett.*, 17(7):379–381, 1966.

[115] Maureen J. Lagos and Philip E. Batson. Thermometry with subnanometer resolution in the electron microscope using the principle of detailed balancing. *Nano Lett.*, 18(7):4556–4563, 2018.

[116] Juan Carlos Idrobo, Andrew R. Lupini, Tianli Feng, Raymond R. Unocic, Franklin S. Walden, Daniel S. Gardiner, Tracy C. Lovejoy, Niklas Dellby, Sokrates T. Pantelides, and Ondrej L. Krivanek. Temperature measurement by a nanoscale electron probe using energy gain and loss spectroscopy. *Phys. Rev. Lett.*, 120(9):095901, 2018.

[117] Knut Müller, Florian F. Krause, Armand Béché, Marco Schowalter, Vincent Galioit, Stefan Löffler, Johan Verbeeck, Josef Zweck, Peter Schattschneider, and Andreas Rosenauer. Atomic electric fields revealed by a quantum mechanical approach to electron picodiffraction. *Nat. Commun.*, 5(1):1–8, 2014.

[118] C. Hébert and P. Schattschneider. A proposal for dichroic experiments in the electron microscope. *Ultramicroscopy*, 96(3):463–468, September 2003.

[119] J.A. Bradley, G.T. Seidler, G. Cooper, Maarten Vos, Adam Percival Hitchcock, A.P. Sorini, C. Schlimmer, and K.P. Nagle. Comparative study of the valence electronic excitations of N_2 by inelastic X-ray and electron scattering. *Phys. Rev. Lett.*, 105(5):053202, 2010.

[120] Ján Rusz, Juan-Carlos Idrobo, and Somnath Bhowmick. Achieving atomic resolution magnetic dichroism by controlling the phase symmetry of an electron probe. *Phys. Rev. Lett.*, 113(14):145501, 2014.

[121] Kevin C. Smith, Agust Olafsson, Xuan Hu, Steven C. Quillin, Juan Carlos Idrobo, Robyn Collette, Philip D. Rack, Jon P. Camden, and David J. Masiello. Direct observation of infrared plasmonic fano antiresonances by a nanoscale electron probe. *Phys. Rev. Lett.*, 123(17):177401, 2019.

[122] Albert Polman, Mathieu Kociak, and F. J. García de Abajo. Electron-beam spectroscopy for nanophotonics. *Nat. Mater.*, 18(11):1158–1171, 2019.

[123] Yves Auad, Cyrille Hamon, Marcel Tencé, Hugo Lourenço-Martins, Vahagn Mkhitaryan, Odile Stéphan, F. J. Garcia de Abajo, Luiz H.G. Tizei, and Mathieu Kociak. Unveiling the coupling of single metallic nanoparticles to whispering-gallery microcavities. *Nano Lett.*, 22(1):319–327, 2021.

[124] Maureen J. Lagos, Andreas Trügler, Ulrich Hohenester, and Philip E Batson. Mapping vibrational surface and bulk modes in a single nanocube. *Nature*, 543(7646):529–532, March 2017.

[125] Sophia Lloyd, Mohamed Babiker, and Jun Yuan. Quantized orbital angular momentum transfer and magnetic dichroism in the interaction of electron vortices with matter. *Phys. Rev. Lett.*, 108(7):074802, 2012.

[126] Ruben Van Boxem, Bart Partoens, and Jo Verbeeck. Inelastic electron-vortex-beam scattering. *Phys. Rev. A*, 91(3):032703, 2015.

[127] Daniel Ugarte and Caterina Ducati. Controlling multipolar surface plasmon excitation through the azimuthal phase structure of electron vortex beams. *Phys. Rev. B*, 93(20):205418, 2016.

[128] Roy J. Glauber and M. Lewenstein. Quantum optics of dielectric media. *Phys. Rev. A*, 43(1):467, 1991.

[129] Julio C. Gutiérrez-Vega, M.D. Iturbe-Castillo, and S. Chávez-Cerda. Alternative formulation for invariant optical fields: Mathieu beams. *Opt. Lett.*, 25(20):1493–1495, 2000.

[130] Andrew Forbes, Michael de Oliveira, and Mark R. Dennis. Structured light. *Nat. Photonics*, 15(4):253–262, 2021.

[131] Jonas Krehl, Giulio Guzzinati, Johannes Schultz, Pavel Potapov, Darius Pohl, Jérôme Martin, Johan Verbeeck, Andreas Fery, Bernd Büchner, and Axel Lubk. Spectral field mapping in plasmonic nanostructures with nanometer resolution. *Nat. Commun.*, 9(1):06572, 2018.

[132] Armin Feist, Sergey V. Yalunin, Sascha Schäfer, and Claus Ropers. High-purity free-electron momentum states prepared by three-dimensional optical phase modulation. *Phys. Rev. Res.*, 2:043227, Nov 2020.

[133] Ivan Madan, Veronica Leccese, Adam Mazur, Francesco Barantani, Thomas LaGrange, Alexey Sapozhnik, Phoebe M. Tengdin, Simone Gargiulo, Enzo Rotunno, Jean-Christophe Olaya, Ido Kaminer, Vincenzo Grillo, F. J. García de Abajo, Fabrizio Carbone, and Giovanni Maria Vanacore. Ultrafast transverse modulation of free electrons by interaction with shaped optical fields. *ACS Photonics*, 9(10):3215–3224, October 2022.

[134] Shai Tsesses, Raphael Dahan, Kangpeng Wang, Tomer Bucher, Kobi Cohen, Ori Reinhardt, Guy Bartal, and Ido Kaminer. Tunable photon-induced spatial modulation of free electrons. *Nat. Mater.*, 22(3):345–352, March 2023.

[135] Nicholas W. Bigelow, Alex Vaschillo, Vighter Iberi, Jon P. Camden, and David J. Masiello. Characterization of the electron- and Photon-Driven plasmonic excitations of metal nanorods. *ACS Nano*, 6(8):7497–7504, August 2012.

[136] Nicholas W. Bigelow, Alex Vaschillo, Jon P. Camden, and David J. Masiello. Signatures of Fano interferences in the electron energy loss spectroscopy and cathodoluminescence of symmetry-broken nanorod dimers. *ACS Nano*, 7(5):4511–4519, 2013.

[137] J. Aleksi Soininen, A.L. Ankudinov, and J.J. Rehr. Inelastic scattering from core electrons: A multiple scattering approach. *Phys. Rev. B*, 72(4):045136, 2005.

[138] Prashant Shekhar, Marek Malac, Vaibhav Gaind, Neda Dalili, Al Meldrum, and Zubin Jacob. Momentum-resolved electron energy loss spectroscopy for mapping the photonic density of states. *ACS Photonics*, 4(4):1009–1014, 2017.

[139] Hikaru Saito, Hugo Lourenço-Martins, Noémie Bonnet, Xiaoyan Li, Tracy C. Lovejoy, Niklas Dellby, Odile Stéphan, Mathieu Kociak, and Luiz Henrique Galvão Tizei. Emergence of point defect states in a plasmonic crystal. *Phys. Rev. B*, 100(24):245402, 2019.

[140] Bruce T. Draine and Piotr J. Flatau. Discrete-dipole approximation for periodic targets: theory and tests. *J. Opt. Soc. Am. A*, 25(11):2693–2703, 2008.

[141] Ron Ruimy, Alexey Gorlach, Chen Mechel, Nicholas Rivera, and Ido Kaminer. Toward atomic-resolution quantum measurements with coherently shaped free electrons. *Phys. Rev. Lett.*, 126:233403, Jun 2021.

[142] Atreyie Ghosh, Sena Yang, Yanan Dai, and Hrvoje Petek. The spin texture topology of polygonal plasmon fields. *ACS Photonics*, 10(1):13–23, January 2023.

[143] Edwin N. Lassettre. Collision cross-section studies on molecular gases and the dissociation of oxygen and water. *Radiat. Res. Suppl.*, 1:530–546, 1959.

[144] E. N. Lassettre, M. E. Krasnow, and S. Silverman. Inelastic scattering of electrons by helium. *J. Chem. Phys.*, 40(5):1242–1248, March 1964.

[145] J. A. Bradley, G. T. Seidler, G. Cooper, M. Vos, A. P. Hitchcock, A. P. Sorini, C. Schlimmer, and K. P. Nagle. Comparative study of the valence electronic excitations of N_2 by inelastic X-ray and electron scattering. *Phys. Rev. Lett.*, 105:053202, Jul 2010.

[146] Marc Adrian, Jacques Dubochet, Jean Lepault, and Alasdair W. McDowall. Cryo-electron microscopy of viruses. *Nature*, 308(5954):32–36, March 1984.

[147] Peter Rez, Toshihiro Aoki, Katia March, Dvir Gur, Ondrej L. Krivanek, Niklas Dellby, Tracy C. Lovejoy, Sharon G. Wolf, and Hagai Cohen. Damage-free vibrational spectroscopy of biological materials in the electron microscope. *Nat. Commun.*, 7(1):1–8, 2016.

[148] Rafael Fernandez-Leiro and Sjors H. W. Scheres. Unravelling biological macromolecules with cryo-electron microscopy. *Nature*, 537(7620):339–346, September 2016.

[149] Jordan A. Hachtel, Jingsong Huang, Ilja Popovs, Santa Jansone-Popova, Jong K. Keum, Jacek Jakowski, Tracy C. Lovejoy, Niklas Dellby, Ondrej L. Krivanek, and Juan Carlos Idrobo. Identification of site-specific isotopic labels by vibrational spectroscopy in the electron microscope. *Science*, 363(6426):525–528, February 2019.

[150] Jiade Li, Jiangxu Li, Jilin Tang, Zhiyu Tao, Siwei Xue, Jiaxi Liu, Hailin Peng, Xing-Qiu Chen, Jiandong Guo, and Xuetao Zhu. Direct observation of topological phonons in graphene. *Phys. Rev. Lett.*, 131:116602, Sep 2023.

[151] C. Dwyer, T. Aoki, P. Rez, S. L. Y. Chang, T. C. Lovejoy, and O. L. Krivanek. Electron-beam mapping of vibrational modes with nanometer spatial resolution. *Phys. Rev. Lett.*, 117:256101, Dec 2016.

[152] Ryosuke Senga, Kazu Suenaga, Paolo Barone, Shigeyuki Morishita, Francesco Mauri, and Thomas Pichler. Position and momentum mapping of vibrations in graphene nanostructures. *Nature*, 573(7773):247–250, September 2019.

[153] Albert Polman, Mathieu Kociak, and F. J. García de Abajo. Electron-beam spectroscopy for nanophotonics. *Nat. Mater.*, 18(11):1158–1171, Nov 2019.

[154] Yves Auad, Eduardo J. C. Dias, Marcel Tencé, Jean-Denis Blazit, Xiaoyan Li, Luiz Fernando Zagonel, Odile Stéphan, Luiz H. G. Tizei, F. Javier García de Abajo, and Mathieu Kociak. μeV electron spectromicroscopy using free-space light. *Nat. Commun.*, 14(1):4442, Jul 2023.

[155] F. Araoka, T. Verbiest, K. Clays, and A. Persoons. Interactions of twisted light with chiral molecules: An experimental investigation. *Phys. Rev. A*, 71:055401, May 2005.

[156] Gabriel Molina-Terriza, Juan P. Torres, and Lluis Torner. Twisted photons. *Nat. Phys.*, 3(5):305–310, May 2007.

[157] Jérémie Harris, Vincenzo Grillo, Erfan Mafakheri, Gian Carlo Gazzadi, Stefano Frabboni, Robert W. Boyd, and Ebrahim Karimi. Structured quantum waves. *Nat. Phys.*, 11(8):629–634, August 2015.

[158] Alison M. Yao and Miles J. Padgett. Orbital angular momentum: origins, behavior and applications. *Adv. Opt. Photon.*, 3(2):161–204, June 2011.

[159] Haoqi Zhao, Yichen Ma, Zihe Gao, Na Liu, Tianwei Wu, Shuang Wu, Xilin Feng, James Hone, Stefan Strauf, and Liang Feng. High-purity generation and switching of twisted single photons. *Phys. Rev. Lett.*, 131:183801, Oct 2023.

[160] Gregorius C.G. Berkhout, Martin P.J. Lavery, Johannes Courtial, Marco W. Beijersbergen, and Miles J. Padgett. Efficient sorting of orbital angular momentum states of light. *Phys. Rev. Lett.*, 105(15):153601, 2010.

[161] H. Di Lorenzo Pires, H. C. B. Florijn, and M. P. van Exter. Measurement of the spiral spectrum of entangled two-photon states. *Phys. Rev. Lett.*, 104:020505, Jan 2010.

[162] Ebrahim Karimi, Daniel Giovannini, Eliot Bolduc, Nicolas Bent, Filippo M. Miatto, Miles J. Padgett, and Robert W. Boyd. Exploring the quantum nature of the radial degree of freedom of a photon via Hong-Ou-Mandel interference. *Phys. Rev. A*, 89:013829, Jan 2014.

[163] Yiyu Zhou, Mohammad Mirhosseini, Dongzhi Fu, Jiapeng Zhao, Seyed Mohammad Hashemi Rafsanjani, Alan E. Willner, and Robert W. Boyd. Sorting photons by radial quantum number. *Phys. Rev. Lett.*, 119:263602, Dec 2017.

[164] Danilo Zia, Nazanin Dehghan, Alessio D'Errico, Fabio Sciarrino, and Ebrahim Karimi. Interferometric imaging of amplitude and phase of spatial biphoton states. *Nat. Photonics*, August 2023.

[165] Suman Karan, Radhika Prasad, and Anand K. Jha. Postselection-free controlled generation of a high-dimensional orbital-angular-momentum entangled state. *Phys. Rev. Appl.*, 20:054027, Nov 2023.

[166] Şerban Suciu, George Andrei Bulzan, Tudor Alexandru Isdrailă, Alexandra Maria Pălici, Stefan Ataman, Cristian Kusko, and Radu Ionicioiu. Quantum communication networks with optical vortices. *Phys. Rev. A*, 108:052612, Nov 2023.

[167] G. F. Quinteiro, D. E. Reiter, and T. Kuhn. Formulation of the twisted-light–matter interaction at the phase singularity: The twisted-light gauge. *Phys. Rev. A*, 91:033808, Mar 2015.

[168] G. F. Quinteiro, D. E. Reiter, and T. Kuhn. Formulation of the twisted-light–matter interaction at the phase singularity: Beams with strong magnetic fields. *Phys. Rev. A*, 95:012106, Jan 2017.

[169] Sijia Gao, Fiona C. Speirits, Francesco Castellucci, Sonja Franke-Arnold, Stephen M. Barnett, and Jörg B. Götte. Paraxial skyrmionic beams. *Phys. Rev. A*, 102:053513, Nov 2020.

[170] T. Zanon-Willette, F. Impens, E. Arimondo, D. Wilkowski, A. V. Taichenachev, and V. I. Yudin. Engineering quantum control with optical transitions induced by twisted light fields. *Phys. Rev. A*, 108:043513, Oct 2023.

[171] Zhi-Wei Lu, Liang Guo, Zheng-Zheng Li, Mamutjan Ababekri, Fang-Qi Chen, Changbo Fu, Chong Lv, Ruirui Xu, Xiangjin Kong, Yi-Fei Niu, and Jian-Xing Li. Manipulation of giant multipole resonances via vortex γ photons. *Phys. Rev. Lett.*, 131:202502, Nov 2023.

[172] D. A. Muller and J. Silcox. Delocalization in inelastic scattering. *Ultramicroscopy*, 59(1):195–213, July 1995.

[173] P. Schattschneider and W. S. M. Werner. Coherence in electron energy loss spectrometry. *J. Electron Spectrosc.*, 143(2):81–95, May 2005.

[174] P. Schattschneider, B. Schaffer, I. Ennen, and J. Verbeeck. Mapping spin-polarized transitions with atomic resolution. *Phys. Rev. B*, 85:134422, Apr 2012.

[175] Shunsuke Muto, Ján Rusz, Kazuyoshi Tatsumi, Roman Adam, Shigeo Arai, Vancho Kocevski, Peter M. Oppeneer, Daniel E. Bürgler, and Claus M. Schneider. Quantitative characterization of nanoscale polycrystalline magnets with electron magnetic circular dichroism. *Nat. Commun.*, 5(1):3138, January 2014.

[176] Ján Rusz, Juan-Carlos Idrobo, and Somnath Bhowmick. Achieving atomic resolution magnetic dichroism by controlling the phase symmetry of an electron probe. *Phys. Rev. Lett.*, 113:145501, Sep 2014.

[177] Mingquan Xu, Aowen Li, Stephen J. Pennycook, Shang-Peng Gao, and Wu Zhou. Probing a defect-site-specific electronic orbital in graphene with single-atom sensitivity. *Phys. Rev. Lett.*, 131:186202, Oct 2023.

[178] Marius Constantin Chirita Mihaila, Philipp Weber, Matthias Schneller, Lucas Grandits, Stefan Nimmrichter, and Thomas Juffmann. Transverse electron-beam shaping with light. *Phys. Rev. X*, 12:031043, Sep 2022.

[179] Vincenzo Grillo, Gian Carlo Gazzadi, Erfan Mafakheri, Stefano Frabboni, Ebrahim Karimi, and Robert W. Boyd. Holographic generation of highly twisted electron beams. *Phys. Rev. Lett.*, 114:034801, Jan 2015.

[180] G. M. Vanacore, G. Berruto, I. Madan, E. Pomarico, P. Biagioni, R. J. Lamb, D. McGrouther, O. Reinhardt, I. Kaminer, B. Barwick, H. Larocque, V. Grillo, E. Karimi, F. J. García de Abajo, and F. Carbone. Ultrafast generation and control of an electron vortex beam via chiral plasmonic near fields. *Nat. Mater.*, 18(6):573–579, June 2019.

[181] M. V. Tsarev, A. Ryabov, and P. Baum. Free-electron qubits and maximum-contrast attosecond pulses via temporal talbot revivals. *Phys. Rev. Res.*, 3:043033, Oct 2021.

[182] Raphael Dahan, Gefen Baranes, Alexey Gorlach, Ron Ruimy, Nicholas Rivera, and Ido Kaminer. Creation of optical Cat and GKP states using shaped free electrons. *Phys. Rev. X*, 13:031001, Jul 2023.

[183] T. Schachinger, P. Hartel, P.-H. Lu, S. Löffler, M. Obermair, M. Dries, D. Gerthsen, R. E. Dunin-Borkowski, and P. Schattschneider. Experimental realization of a $\pi/2$ vortex mode converter for electrons using a spherical aberration corrector. *Ultramicroscopy*, 229:113340, October 2021.

[184] Stefan Löffler. Unitary two-state quantum operators realized by quadrupole fields in the electron microscope. *Ultramicroscopy*, 234:113456, April 2022.

[185] Stefan Löffler, Thomas Schachinger, Peter Hartel, Peng-Han Lu, Rafal E. Dunin-Borkowski, Martin Obermair, Manuel Dries, Dagmar Gerthsen, and Peter Schattschneider. A quantum logic gate for free electrons. *Quantum*, 7:1050, jul 2023.

[186] Nicholas Rivera, Liang Jie Wong, Marin Soljačić, and Ido Kaminer. Ultrafast multiharmonic plasmon generation by optically dressed electrons. *Phys. Rev. Lett.*, 122:053901, Feb 2019.

[187] Franck Aguilar, Hugo Lourenço-Martins, Damián Montero, Xiaoyan Li, Mathieu Kociak, and Alfredo Campos. Selective probing of longitudinal and transverse plasmon modes with electron Phase-Matching. *J. Phys. Chem. C*, 127(45):22252–22264, November 2023.

[188] Philip Trøst Kristensen, Rong-Chun Ge, and Stephen Hughes. Normalization of quasinormal modes in leaky optical cavities and plasmonic resonators. *Phys. Rev. A*, 92:053810, Nov 2015.

[189] Rong-Chun Ge and Stephen Hughes. Quasinormal mode theory and modelling of electron energy loss spectroscopy for plasmonic nanostructures. *Journal of Optics*, 18(5):054002, March 2016.

[190] Sebastian Franke, Stephen Hughes, Mohsen Kamandar Dezfouli, Philip Trøst Kristensen, Kurt Busch, Andreas Knorr, and Marten Richter. Quantization of quasinormal modes for open cavities and plasmonic cavity quantum electrodynamics. *Phys. Rev. Lett.*, 122:213901, May 2019.

[191] Konstantin Y. Bliokh, Peter Schattschneider, Jo Verbeeck, and Franco Nori. Electron vortex beams in a magnetic field: A new twist on Landau levels and Aharonov-Bohm states. *Phys. Rev. X*, 2:041011, Nov 2012.

[192] Ruben Van Boxem, Bart Partoens, and Johan Verbeeck. Rutherford scattering of electron vortices. *Phys. Rev. A*, 89:032715, Mar 2014.

[193] Vincenzo Grillo, Ebrahim Karimi, Gian Carlo Gazzadi, Stefano Frabboni, Mark R. Dennis, and Robert W. Boyd. Generation of nondiffracting electron Bessel beams. *Phys. Rev. X*, 4:011013, Jan 2014.

[194] P. Schattschneider, M. Stöger-Pollach, and J. Verbeeck. Novel vortex generator and mode converter for electron beams. *Phys. Rev. Lett.*, 109:084801, Aug 2012.

[195] R. H. Ritchie. Plasma losses by fast electrons in thin films. *Phys. Rev.*, 106:874–881, Jun 1957.

[196] P. Schattschneider, C. Hébert, H. Franco, and B. Jouffrey. Anisotropic relativistic cross sections for inelastic electron scattering, and the magic angle. *Phys. Rev. B*, 72:045142, Jul 2005.

[197] Nahid Talebi, Wilfried Sigle, Ralf Vogelgesang, and Peter van Aken. Numerical simulations of interference effects in photon-assisted electron energy-loss spectroscopy. *New J. Phys.*, 15(5):053013, 2013.

[198] Yang Cao, Alejandro Manjavacas, Nicolas Large, and Peter Nordlander. Electron energy-loss spectroscopy calculation in finite-difference time-domain package. *ACS Photonics*, 2(3):369–375, 2015.

[199] Ulrich Hohenester and Andreas Trügler. MNPBEM–a Matlab toolbox for the simulation of plasmonic nanoparticles. *Comput. Phys. Commun.*, 183(2):370–381, 2012.

[200] Huigao Duan, Antonio I. Fernández-Domínguez, Michel Bosman, Stefan A. Maier, and Joel K. W. Yang. Nanoplasmonics: Classical down to the nanometer scale. *Nano Lett.*, 12(3):1683–1689, 2012.

[201] Jan Pomplun, Sven Burger, Lin Zschiedrich, and Frank Schmidt. Adaptive finite element method for simulation of optical nano structures. *Phys. Status Solidi (b)*, 244(10):3419–3434, 2007.

[202] E. M. Purcell and C. R. Pennypacker. Scattering and absorption of light by nonspherical dielectric grains. *Astrophys. J.*, 186:705–714, 1973.

[203] P. B. Johnson and R. W. Christy. Optical constants of the noble metals. *Phys. Rev. B*, 6:4370–4379, Dec 1972.

[204] Cécile Hébert, Peter Schattschneider, H. Franco, and Bernard Jouffrey. ELNES at magic angle conditions. *Ultramicroscopy*, 106(11-12):1139–1143, 2006.

[205] Tyler R. Harvey, Jordan S. Pierce, Amit K. Agrawal, Peter Ercius, Martin Linck, and Benjamin J. McMorran. Efficient diffractive phase optics for electrons. *New J. Phys.*, 16(9):093039, September 2014.

[206] Fehmi S. Yasin, Tyler R. Harvey, Jordan J. Chess, Jordan S. Pierce, Colin Ophus, Peter Ercius, and Benjamin J. McMorran. Probing light atoms at subnanometer resolution: Realization of scanning transmission electron microscope holography. *Nano Lett.*, 18(11):7118–7123, November 2018.

[207] Hugo Lourenço-Martins, Axel Lubk, and Mathieu Kociak. Bridging nano-optics and condensed matter formalisms in a unified description of inelastic scattering of relativistic electron beams. *SciPost Phys.*, 10:031, 2021.

[208] A. Ben Hayun, O. Reinhardt, J. Nemirovsky, A. Karnieli, N. Rivera, and I. Kaminer. Shaping quantum photonic states using free electrons. *Sci. Adv.*, 7(11):eabe4270, 2021.

[209] Timothy J. Davis, David Janoschka, Pascal Dreher, Bettina Frank, Frank J. Meyer zu Heringdorf, and Harald Giessen. Ultrafast vector imaging of plasmonic skyrmion dynamics with deep subwavelength resolution. *Science*, 368(6489):eaba6415, April 2020.

[210] Yijie Shen, Eduardo Casas Martínez, and Carmelo Rosales-Guzmán. Generation of optical skyrmions with tunable topological textures. *ACS Photonics*, 9(1):296–303, January 2022.

[211] Lingyuan Gao, Sergei Prokhorenko, Yousra Nahas, and Laurent Bellaiche. Dynamical multiferroicity and magnetic topological structures induced by the orbital angular momentum of light in a nonmagnetic material. *Phys. Rev. Lett.*, 131:196801, Nov 2023.